

**FLOW-TOPOGRAPHY INTERACTIONS, PARTICLE TRANSPORT AND
PLANKTON DYNAMICS AT THE FLOWER GARDEN BANKS:
A MODELING STUDY**

A Dissertation

by

SIMONE FRANCIS

Submitted to the Office of Graduate Studies of
Texas A&M University
in partial fulfillment of the requirements for the degree of
DOCTOR OF PHILOSOPHY

December 2005

Major Subject: Oceanography

**FLOW-TOPOGRAPHY INTERACTIONS, PARTICLE TRANSPORT AND
PLANKTON DYNAMICS AT THE FLOWER GARDEN BANKS:**

A MODELING STUDY

A Dissertation

by

SIMONE FRANCIS

Submitted to the Office of Graduate Studies of
Texas A&M University
in partial fulfillment of the requirements for the degree of

DOCTOR OF PHILOSOPHY

Approved by:

Chair of Committee,	George A. Jackson
Committee Members,	Robert D. Hetland
	James L. Pinckney
	William H. Neill
Head of Department,	Wilford D. Gardner

December 2005

Major Subject: Oceanography

ABSTRACT

Flow-Topography Interactions, Particle Transport and
Plankton Dynamics at the Flower Garden Banks:
a Modeling Study. (December 2005)

Simone Francis, B.E., City College of New York;
M.S., California Institute of Technology

Chair of Advisory Committee: Dr. George A. Jackson

Flow disruption resulting from interactions between currents and abrupt topography can have important consequences for biological processes in the ocean. A high-resolution three-dimensional hydrodynamic model is used to study topographically influenced flow at the Flower Garden Banks, two small but thriving coral reef ecosystems in the northwest Gulf of Mexico. Flow past the modeled banks is characterized by vortex shedding, turbulent wake formation and strong return velocities in the near-wake regions. The speed of the oncoming current, strength of water-column stratification, and level of topographic detail used in the model each serve to modulate these basic flow characteristics.

Larval retention and dispersal processes at the Flower Garden Banks, and specifically the dependence of these processes on the nature of flow disruption, are explored by coupling a Lagrangian particle-tracking algorithm to the hydrodynamic model. Passive particles released from the tops of the modeled banks as mimics of coral larvae can remain trapped in the wake regions very close to the banks on time scales of hours to days, depending primarily on the speed of the free-stream current. Most particles are swept quickly downstream, however, where their trajectories are most strongly influenced by the topography of the continental shelf. Modeled dispersal patterns suggest that there is an ample supply of larvae from the Flower Garden Banks to nearby oil and gas platforms, which can provide suitable benthic habitat for corals.

The flow disturbances generated by the modeled banks result in the mixing of nutrients from deeper water into shallower, nutrient-depleted layers in the wakes of the banks. The ability of the planktonic system to respond to such an injection of nutrients is tested by embedding a simple nutrient-phytoplankton-zooplankton ecosystem model into the hydrodynamic model. Plankton biomass in the flow-disturbed wakes is shown to increase in response to the additional nutrients.

This study shows how flow-topography interactions at the Flower Garden Banks can exert critical control over local larval transport processes and plankton dynamics. More generally, it demonstrates the usefulness and feasibility of using numerical models as tools to uncover important mechanisms of physical-biological interaction in the ocean.

ACKNOWLEDGMENTS

All that I am, or hope to be, I owe to my angel mother.

– Abraham Lincoln

This dissertation, the culmination of almost six years of effort, would not have come to fruition without a great deal of help from a great number of people. To my advisor, George Jackson, I owe the deepest debt of gratitude. He has been the most inspiring, supportive, patient and generous mentor I could ever have hoped for. He is one of the most dynamic and most effective teachers I've ever known, and has always amazed me with his incredible versatility and insight as a researcher. George, I am so thankful to have had the opportunity to learn from you. I am still more thankful to have you as a friend.

I thank the members of my advisory committee—Rob Hetland, for teaching me how to work with ROMS; Jay Pinckney, for asking the tough biology questions; Bill Neill, for challenging me to think big and for being my greatest cheerleader. Each of them has made valuable contributions, not only to this dissertation, but also to my development as a scientist.

Past and present members of the Ecosystem Modeling Group (aka the Jackson Lab), have consistently provided thoughtful advice and moral support, not to mention plenty of bad puns, birthday cakes and Chinese yo-yo targets. For all of it, I give many thanks to Greg Breed, Cheryl Brown, Adrian Burd, Damien Eveillard, Debby Ianson, Tammi Richardson, Tim Sellers and Lars Stemmann.

Thanks also go to Mark McCann and Steve Baum, who have been the indispensable computer gurus every girl needs two of. They were always happy to come to my rescue when I had hardware and software problems.

I am grateful to all of the friends and fellow students who have helped make my years at Texas A&M fun and rewarding. Although I cannot list them all, I would particularly like to thank Amy Bratcher, Jim Kaldy, Sharath Ravula, Patrick Ressler, Hank Seidel and Ellen Toby.

My family has always provided the solid foundation I've needed to lean on and to grow from, and for that I am so thankful. It is from my angel mother, Susan, my indefatigable father, David, and my two brilliant, beautiful sisters, Bridget and Nicole, that I draw my own strength. I cannot imagine getting through graduate school, let alone life, without them.

And finally, to Garrett, whose ardent devotion to me has no apparent limit, I say a humble, heartfelt thank you—for always believing in me; for sharing your intelligence, strength and playfulness with me; for getting me a bug balloon and escaping with me to the ballpark when I really needed it; and for making my little life a great big adventure.

TABLE OF CONTENTS

	Page
ABSTRACT	iii
ACKNOWLEDGMENTS.....	v
TABLE OF CONTENTS	vii
LIST OF FIGURES.....	ix
LIST OF TABLES	xi
CHAPTER	
I INTRODUCTION.....	1
II FLOW-TOPOGRAPHY INTERACTIONS AND IMPLICATIONS FOR BIOLOGICAL PROCESSES	3
2.1 Overview.....	3
2.2 Introduction.....	4
2.3 The Flower Garden Banks	6
2.4 The Numerical Model.....	8
2.5 Strategy	12
2.6 Results.....	12
2.7 Discussion.....	37
2.8 Conclusions.....	42
III PARTICLE TRANSPORT AND IMPLICATIONS FOR LARVAL DYNAMICS.....	43
3.1 Overview.....	43
3.2 Introduction.....	44
3.3 The Flower Garden Banks	46
3.4 Model Description and Configuration	49
3.5 Strategy	53
3.6 Results.....	53
3.7 Discussion.....	73
3.8 Conclusions.....	80
IV PLANKTON DYNAMICS	82
4.1 Overview.....	82
4.2 Introduction.....	83
4.3 The Flower Garden Banks	84
4.4 The Hydrodynamic Model.....	85
4.5 Flow Disruption and Nutrient Upwelling.....	87

CHAPTER	Page
4.6 The Ecosystem Model	89
4.7 Discussion.....	94
4.8 Conclusions.....	97
V CONCLUSIONS	99
REFERENCES.....	101
VITA	109

LIST OF FIGURES

FIGURE	Page
2.1 Map of study area.....	7
2.2 Model bathymetries.....	9
2.3 Initial vertical profiles of temperature and buoyancy frequency	10
2.4 Cross-shelf sections of velocity for simulation A	13
2.5 Streamlines and velocity anomaly vectors at three depths.....	14
2.6 Cross-shelf sections of velocity for simulation B	16
2.7 Alongshelf sections of velocity for simulation B.....	17
2.8 Streamlines and velocity anomaly vectors for simulation C.....	18
2.9 Strouhal number, wake volume and wake velocity extrema as a function of Rossby number	20
2.10 Isopycnal displacements and relative vorticity for simulation C.....	24
2.11 Normalized relative vorticity as a function of Rossby number.....	25
2.12 Density structure and vertical velocity contours	26
2.13 Maximum vertical eddy diffusivity as a function of Rossby number.....	27
2.14 Streamlines and velocity anomaly vectors for simulation H.....	30
2.15 Density anomaly and relative vorticity for simulation H.....	32
2.16 Alongshelf sections of velocity for simulation I	33
2.17 Comparison of idealized and more realistic bathymetries	34
2.18 Streamlines and velocity anomaly vectors for simulation J.....	35
3.1 Map of Flower Garden Banks	47
3.2 Model bathymetries and platform locations.....	50
3.3 Comparison of flow patterns	54
3.4 Comparison of wake structures	55
3.5 Loss of particles over time	57
3.6 Patterns in particle loss.....	58

FIGURE		Page
3.7	Patterns in particle dispersal.....	60
3.8	Variances in particle positions and effective mixing coefficients.....	63
3.9	Dispersal of near-surface released particles	64
3.10	Interbank particle transport for simulations A, B and C	65
3.11	Interbank particle transport for simulations B, D and G	66
3.12	Particle-platform contacts, simulations A, B and C	68
3.13	Particle-platform contacts, simulations B and G.....	69
3.14	Particle-platform contacts as a function of platform location	70
3.15	Platform locations for reversed inflow simulation	72
4.1	Model bathymetry	85
4.2	Initial vertical profiles of temperature and nutrient-like tracer	86
4.3	Upwelling of a nutrient	88
4.4	Diagram of the ecosystem model	89
4.5	Results of the one-dimensional model	93
4.6	Results of the three-dimensional coupled model	95

LIST OF TABLES

TABLE		Page
2.1	Parameters of the flow-topography simulations.....	12
3.1	Parameters of the particle-transport simulations.....	53
3.2	Particle-platform contact data	71
4.1	Symbols used in the ecosystem model.....	91

CHAPTER I

INTRODUCTION

The East and West Flower Garden Banks, two small, submerged topographic features in the northwest Gulf of Mexico, are home to surprisingly abundant and diverse assemblages of marine life. Reef-building corals form the foundation of the ecosystem at each bank; the corals share their habitat with a wide variety of reef-associated invertebrates and small tropical fish, as well as with larger creatures such as barracuda, hammerhead sharks, sea turtles and manta rays.

The Banks are fascinating from a biological viewpoint, not least because they are the northernmost tropical coral reef systems in the Gulf of Mexico and are far away from their nearest reef neighbors in Veracruz, Mexico, on the Yucatan Peninsula and in the Florida Keys. The magnitudes and mechanisms of biological connectivity among the coral reefs of the Gulf of Mexico and the Caribbean Sea remain open questions. The Flower Garden Banks are certainly sources of coral larvae—spawning activities are well-documented. The extent to which they act as sinks to larvae originating elsewhere is unknown.

The Flower Garden Banks are also remarkable from the standpoint of ocean physics, since, having grown atop naturally occurring salt domes, they rise abruptly from seafloor depths of 100–150 m near the continental shelf break to within 20 m of the sea surface over horizontal distances of 5–10 km. Interactions between shelf currents and multiple prominent bathymetric features have not been well-studied; there are many new things to be discovered about how the Flower Garden Banks exert influence on the flow field surrounding them.

The goal of the present research is to explore flow-topography interactions at the Flower Garden Banks with a focus on the influences these interactions have on the

This dissertation follows the style and format of the Journal of Marine Systems.

important biological processes of larval transport and plankton dynamics. The use of a numerical modeling approach for this exploration serves to reduce the complexity of the problem, and allows the effects of various interacting factors to be analyzed separately.

The purely physical aspects of the flow-topography problem are presented and discussed in chapter II of the dissertation. A high-resolution three-dimensional hydrodynamic model is configured to represent conditions at the Flower Garden Banks, and simulations are conducted in which inflow forcing velocity, strength of water-column stratification and degree of bathymetric realism are varied. Changes in the flow field resulting from these variations are discussed in terms of potential impacts on particle transport and plankton dynamics.

In chapter III, some of the predictions made with respect to particle transport are actually tested by releasing passive particles from the modeled banks into the flow fields, tracking them through time, and quantifying rates of retention, far-field dispersal and interbank exchange. The results are interpreted in terms of what they might mean for larval transport processes.

Chapter IV describes a very simple ecosystem model that is coupled to the hydrodynamic model in an effort to test the link between flow disturbance, nutrient upwelling and planktonic food-web response at the Flower Garden Banks.

CHAPTER II

FLOW-TOPOGRAPHY INTERACTIONS AND IMPLICATIONS FOR BIOLOGICAL PROCESSES

2.1 Overview

Multiple topographic features on a continental shelf can interact to provide more complicated flows than a single feature and are more representative of real bathymetry. I used a three-dimensional primitive-equation hydrodynamic model to study flow over two abrupt topographic features on a continental shelf. A highly idealized geometry, which modeled the topographic features as Gaussian peaks, was used to study the effects of varying inflow velocity and stratification. Use of a more realistic bathymetry, based on the Flower Garden Banks in the northwest Gulf of Mexico, allowed the effects of topographic detail to be studied. Flow over the Gaussian peaks is characterized by vortex shedding, with faster inflow speeds leading to more vigorous shedding activity, stronger wake velocities, larger wake regions, and larger vertical eddy diffusivities (i.e. larger turbulent mixing rates) over the tops of the peaks and in their wakes. Unsteady velocity forcing leads to flow disturbances with broader cross-shelf signatures and larger variabilities in all flow descriptors. Strong stratification results in a two-layer system, with flow disturbances confined to depths below the tops of the banks, whereas weaker stratification leads to single-layer flow with strong surface signatures generated by the subsurface features. Use of more realistic bathymetry disrupts the basic vortex-shedding nature of the flow and changes the shapes and sizes of the wakes, but does not significantly alter the maximum wake velocities or the degree of turbulence enhancement. The complex flow patterns generated in the model are expected to have significant implications for biological processes such as larval retention and dispersal and plankton dynamics, all of which are important to ecosystem function at the Flower Garden Banks and elsewhere.

2.2 Introduction

The interaction of currents and abrupt bottom topography creates complex circulation patterns in the rotating, density-stratified oceanic system. Much of the research done on this topic has focused on flow around seamounts in the deep ocean and has included theoretical studies, scaled-down laboratory experiments, field observations and numerical modeling efforts. Understanding the basic flow patterns generated by such topographic interactions has value in itself, but of more practical importance is the influence these fundamental flow patterns have on the various chemical and biological processes that occur in the ocean, from nutrient pumping and its impact on plankton dynamics to vortex shedding and its impact on larval dispersal.

Examples of some of the important physical flow patterns and phenomena that have been described for flow-topography interactions include formation of Taylor caps, generation and shedding of trailing vortices, vertical displacement of isopycnals, and enhancement of turbulent mixing. In the case of an isolated seamount, fluid often goes around rather than over the seamount, resulting in a region of water trapped directly above the feature—a Taylor cap. Taylor cap formation is a direct consequence of the vertical rigidity of rapidly rotating flows, which constrains flow to be along isobaths. Many theoretical, observational and modeling studies of Taylor cap formation over abrupt topographies (e.g. Hogg, 1973; Huppert and Bryan, 1976; Owens and Hogg, 1980; Smith, 1992; Chapman and Haidvogel, 1992; Beckmann and Haidvogel, 1997) have shown that the critical parameter determining the character of the flow is the Rossby number, $Ro = U/fL$, where U is the freestream velocity, f the Coriolis parameter and L the horizontal length scale of the topographic feature. Taylor caps tend to form when the Rossby number is small, generally less than $O(10^{-1})$, and depend on the relative height of the topography. The shape and vertical extent of the Taylor cap is further controlled by the strength of density stratification, which is commonly described using another dimensionless parameter, the Burger number, $Bu = (NH/fL)^2$. Here, $N = (\Delta\rho g/\rho_0 H)^{1/2}$ is the buoyancy frequency, $\Delta\rho$ the change in fluid density through the water column, g the gravitational acceleration, ρ_0 a reference density, H the total depth of the

fluid, and f and L are as defined above. The existence of Taylor caps and their influence on water column properties have been implicated in particle capture (Goldner and Chapman, 1997), fish egg and larva aggregation and retention (Kloppmann et al., 2001), and enhanced phytoplankton production (Dower et al., 1992; Comeau et al., 1995) above and near submerged topographic features.

More relevant to this study are cases where the Rossby number is $O(10^{-1})$ or greater, leading to the formation and shedding of vortices downstream of a topographic feature. This phenomenon has been most carefully studied by Boyer and colleagues via tow-tank laboratory experiments (Boyer and Kmetz, 1983; Boyer et al., 1987; Boyer and Zhang, 1990), and more recently by Schär and Durran (1996) and Castro et al. (2001), who worked in the atmospheric rather than oceanic realm. A combined numerical and observational study by Coutis and Middleton (2002) showed vortex shedding in the lee of an isolated deep-ocean island. Observations by Royer (1978) of small-scale eddies in the Pacific Ocean correlated well with the presence of upstream seamounts, the inference being that they were generated by flow interactions with the seamounts and transported downstream from there. Vortex shedding frequencies are often described using the nondimensional Strouhal number, $St = \omega_e L / U$, where ω_e is the shedding frequency and L and U are as defined above. St appears to be relatively insensitive to variations in the Rossby and Burger numbers, at least for values of these parameters characteristic of seamount-generated flows (Boyer et al., 1987).

Lee-side vortex generation and shedding is also associated with a number of phenomena that have been modeled and observed in the wake regions behind submerged obstacles as well as behind surface-piercing islands. These include enhanced relative vorticity (Hasegawa et al., 2004), strong and persistent return flows (Boyer and Zhang, 1990), and isopycnal displacements (Rissik et al., 1997; Coutis and Middleton, 2002). It is easy to envision each of these wake-region properties having significant implications for biologically relevant processes such as particle and plankton dynamics.

Turbulent mixing rates near seamounts and other abrupt topographic features, measured using microstructure probes, have been found to be one to five orders of

magnitude greater than background rates (Toole et al., 1997; Lueck and Mudge, 1997; Moum and Nash, 2000; Lavelle et al., 2004). Such topography-induced enhancement of mixing is important in terms of its potentially very large contribution to overall turbulent dissipation in the ocean. Turbulent mixing is also known to influence marine ecosystem dynamics via its impact on nutrient fluxes (e.g. Crawford and Dewey, 1989), phytoplankton cell sizes and food-web structure (e.g. Kiørboe, 1993), and zooplankton production rates (e.g. Visser and Stips, 2002).

The inspiration for this study comes from an interest in how flow-topography interactions affect biological processes at the Flower Garden Banks, a coral reef ecosystem in the northwestern Gulf of Mexico. It is a very complex system, both in its topography and in the variety of physical forcing mechanisms affecting it, and any modeling effort must necessarily simplify it considerably. My interest is in developing an understanding of the flow structures and other phenomena that could occur at the Banks by starting with very simple geometry and forcing, systematically adding more realistic detail. In this chapter, I examine how variations in inflow velocity, strength of stratification and bathymetric detail influence the response of the system, with an emphasis on properties important for biological processes.

The results extend much of the work that has been done on deep-ocean seamount systems to conditions more typical of continental-shelf regions, where Rossby and Burger numbers are generally larger and spatial scales are much smaller. This study forms the basis for the physical-biological models described in chapters III and IV which use Lagrangian particle tracking and embedded ecosystem modeling to explore larval transport and plankton dynamics at the Flower Garden Banks.

2.3 The Flower Garden Banks

The East and West Flower Garden Banks are two topographic features that rise abruptly from seafloor depths of 100–150 m to approximately 20 m. They are located on the continental shelf of the northwestern Gulf of Mexico, approximately 200 km south of the Texas-Louisiana border, near the shelf break (Fig. 2.1). Local water temperature and light penetration are sufficient to sustain small but thriving coral reef ecosystems atop

both of the banks.

Average surface-layer currents in the region are directed alongshore toward the east at 8 cm s^{-1} , but variability in both speed and direction is large (DiMarco et al., 1997). Near-surface flow at the banks is strongly wind-driven, as it is over most of the continental shelf (Cochrane and Kelly, 1986; Cho et al., 1998). Tidal ellipses are oriented with their major axes across bathymetric contours (i.e. in the cross-shelf direction) and tidal currents range from $\sim 3\text{-}6 \text{ cm s}^{-1}$ (DiMarco and Reid, 1998). The

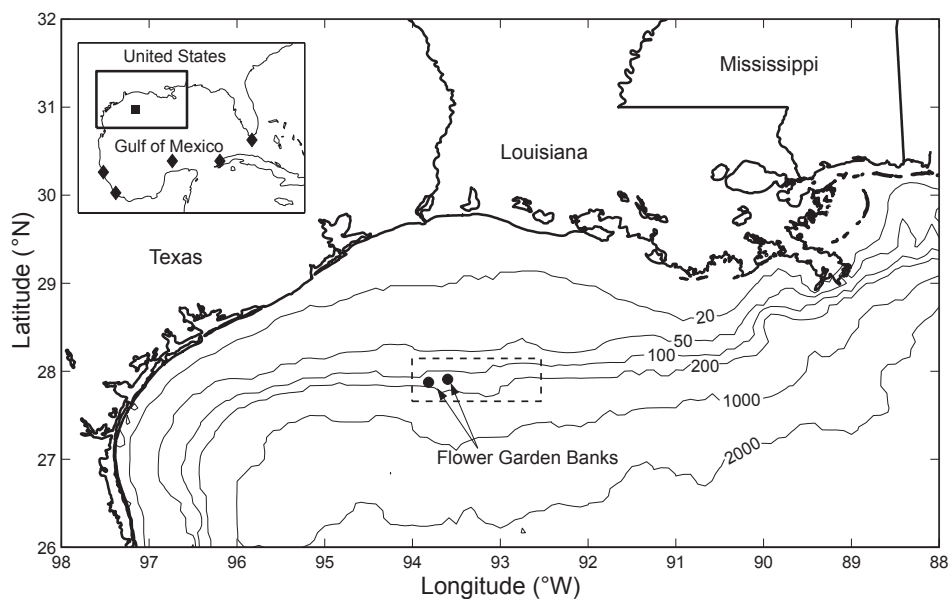


Fig. 2.1. Map of study area. Dashed box shows region modeled. Filled square in inset box shows location of Flower Garden Banks. Diamonds in inset box show locations of nearest coral reefs. Depth contours in meters.

position of the banks near the shelf break makes them subject to the influences of deep-water processes as well, most importantly the large anticyclonic eddies that separate from the Loop Current in the eastern Gulf of Mexico. These eddies travel westward through the Gulf, eventually impacting the slope where they are partly responsible for the eastward flow near the shelf-break and can cause significant cross-shelf transport (Brooks, 1984; Oey, 1995; Sahl et al., 1997).

The banks are separated from each other by about 20 km; they are more than 600 km

from their nearest neighboring coral reefs in the Florida Keys, near the Yucatan Peninsula, and off Veracruz, Mexico (Fig. 2.1). Thus, questions about long-distance larval transport versus localized self-seeding, and the details of larval dispersal and recruitment dynamics are particularly relevant in the region.

2.4 The Numerical Model

2.4.1 Model description

I used the Regional Ocean Modeling System (ROMS), described in detail by Haidvogel et al. (2000), Marchesiello et al. (2003) and Shchepetkin and McWilliams (2005), to model the flow field. ROMS is a free-surface hydrostatic model that solves the primitive equations of motion using finite-difference approximations on orthogonal coordinates in the horizontal and a stretched, bottom-following coordinate in the vertical.

2.4.2 Model configuration

The geographic region extended from ~ 92.5 to 94° W longitude and from ~ 27.7 to 28.1° N latitude, forming a domain ~ 140 km in the alongshelf (zonal) direction and ~ 50 km in the cross-shelf (meridional) direction. The horizontal grid consisted of 205 cells in the alongshelf direction and 125 cells in the cross-shelf direction. In both the alongshelf and cross-shelf directions, horizontal grid resolution varied smoothly and gradually from 200 m over a region centered on the banks to 2000 m near each boundary of the domain. The maximum relative change in grid cell length between any two adjacent cells was less than 5%. There were forty vertical levels, with resulting vertical grid resolutions of ~ 0.5 m above the banks, where the minimum depth was ~ 20 m, and ~ 3 to 11 m in regions of maximum depth. The Coriolis parameter was set to a constant value of $6.8 \times 10^{-5} \text{ s}^{-1}$, which corresponds to 27.9° N latitude; beta-plane effects were neglected.

I tested both highly idealized and somewhat more realistic bathymetries in the model. The idealized topography consisted of two Gaussian peaks, representing the East and West Flower Garden Banks, on a smooth shelf-slope region (Fig. 2.2a). The more realistic bathymetry was created by combining two data sets: that of Gardner et al. (1998), with a horizontal resolution less than 10 m, for the banks themselves, and that of Herring (Dynalysis of Princeton, unpublished data), with a ~ 1 -km resolution, for the

surrounding shelf and slope regions (Fig. 2.2b). Depth values at grid points were calculated by bilinear interpolation of the combined data sets. The topographically complex slope region was greatly simplified by imposing a maximum depth of 300 m offshore. The resulting bathymetry was then smoothed using a selective Shapiro filter such that the maximum relative variation in topography computed on the discrete grid was less than 0.15, a constraint that is thought to minimize potential pressure-gradient errors (Beckman and Haidvogel, 1993).

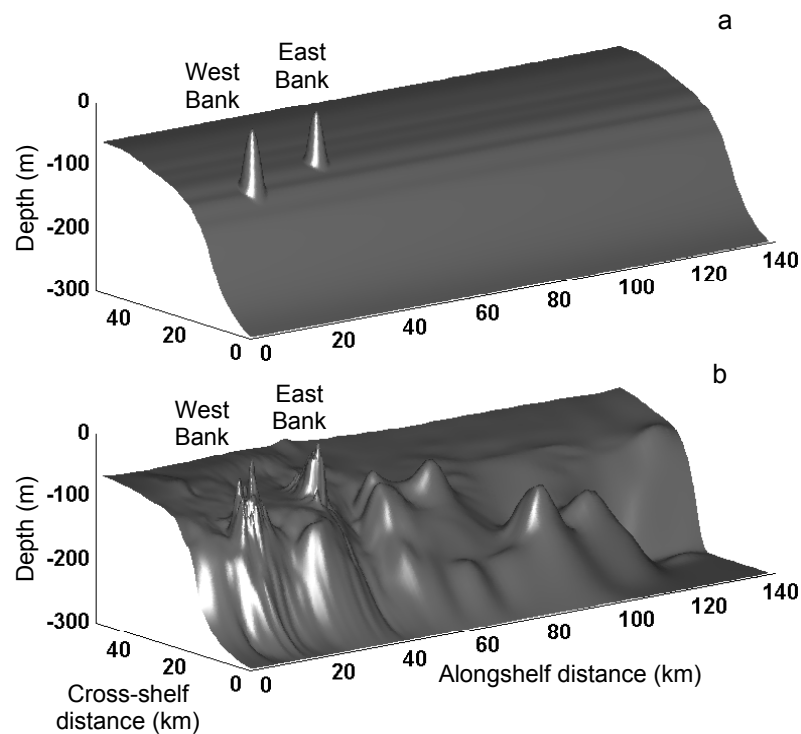


Fig. 2.2. Model bathymetries. (a) Ideal case. (b) Realistic case.

The density-Jacobian scheme of Shchepetkin and McWilliams (2003) was used to compute the pressure gradient terms. Diagnostic simulations were conducted without forcing and with closed-wall boundary conditions; the resulting spurious velocities generated by pressure gradient errors were negligibly small.

2.4.3 Initialization

Initial water column stratification was set by choosing a typical potential temperature vertical profile from data gathered near the Flower Garden Banks during the LATEX program (Jochens et al., 1998). One of two profiles was used to initialize the entire domain. Most of the simulations used a temperature profile derived from a summer 1992 cruise when surface temperature was 29°C and there was a strong thermocline centered at 35 m. A temperature profile more typical of winter conditions, based on data from a February 1994 cruise, was used for comparison in one simulation. The winter profile had a surface temperature of about 21°C and a relatively weak thermocline at 100 m (Fig. 2.3). The buoyancy frequency associated with the winter profile is relatively constant at $\sim 0.01\text{ s}^{-1}$; buoyancy frequency for the summer profile peaks at $\sim 0.03\text{ s}^{-1}$ in the thermocline and is $\sim 0.01\text{ s}^{-1}$ below 100 m. For both cases, the Burger number is $O(10)$, indicating that stratification effects should be important for the flow.

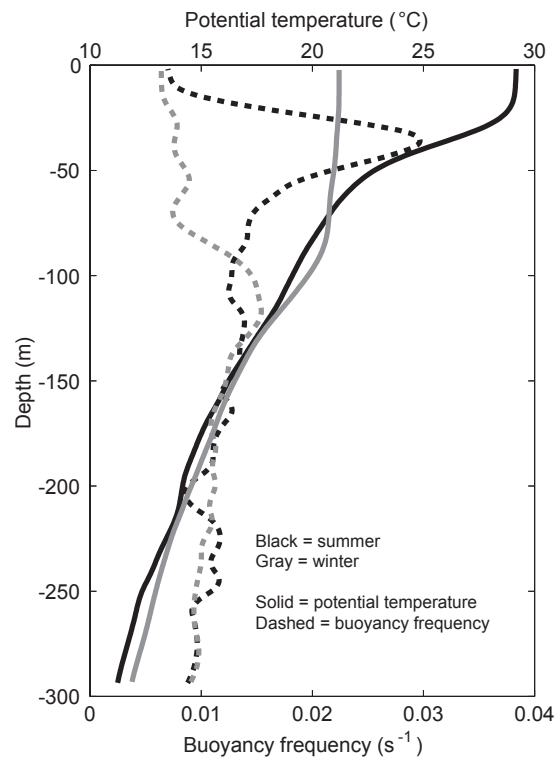


Fig. 2.3. Initial vertical profiles of temperature and buoyancy frequency. Summer and winter stratification cases are shown. There was no initial horizontal variation in potential temperature.

Salinity varies moderately with depth near the Flower Garden Banks on a seasonal basis. Most of the variability is in the upper 10-20 m. Annual surface salinity near the Flower Garden Banks averages 35.5 (30.4-37.4) psu, while near-bottom salinity averages 36.3 (35.6-36.8) psu (Jochens et al., 1998). For simplicity, its value was fixed at a uniform 36 psu in the model. Seawater density was computed in the model using the UNESCO equation of state.

2.4.4 Sub-gridscale parameterizations

I used the 2.5 level model of Mellor and Yamada (1982) for the turbulent closure scheme. The third-order, upstream-biased advection scheme of ROMS obviates the need for explicit horizontal mixing of momentum and tracers in many cases; I used non-zero horizontal viscosity and diffusivity coefficients only in the sponge layers described below. Additional dissipation was introduced via quadratic bottom friction using a constant drag coefficient of 10^{-3} .

2.4.5 Forcing

Each simulation started with the water at rest throughout the domain; currents were induced by specifying a uniform barotropic velocity at the upcurrent boundary. The velocity was increased from zero to the target value over a period of three days using a hyperbolic tangent multiplier. Variations in the imposed forcing form an integral part of the overall strategy employed and will be discussed in section 2.5.

2.4.6 Boundary conditions

The onshore and offshore boundaries of the domain were closed, while the upcurrent and downcurrent boundaries were open and subject to radiation of mass and momentum. I implemented the oblique radiation and adaptive nudging technique described by Marchesiello et al. (2001) at the open boundaries. Where information fluxes were directed into the domain, I nudged boundary temperatures to their specified initial values and barotropic velocities to the imposed forcing value, both on a time scale of four hours (strong nudging). Where fluxes were directed out of the domain, I allowed barotropic velocity and temperature to relax to the desired background values on a time scale of 14 days (weak nudging). A sponge layer provided damping over 5 grid points (about 10

km) on the downcurrent end of the domain; Laplacian horizontal mixing coefficients for momentum and tracers increased quadratically in this region from zero in the interior to $100 \text{ m}^2 \text{ s}^{-1}$ at the boundary.

2.5 Strategy

The reference simulation consisted of an 8 cm s^{-1} eastward flow over the idealized topography grid with summertime stratification. I constructed this baseline case in steps, starting with a shelf-slope only (i.e. no banks) simulation followed by a single-bank case and then a two-bank case. Additional simulations were conducted using steady eastward velocities of 4, 12 and 16 cm s^{-1} ; using the winter stratification; reversing the flow direction; and using the more realistic bathymetry. Two final simulations incorporated diurnal sinusoidal velocity forcing on the ideal and realistic topographies. Table 2.1 summarizes the conditions for each of the simulations conducted.

Table 2.1. Parameters of the flow-topography simulations. Details of geometries and stratifications are as described in the text. Inflow speed is positive eastward, negative westward. ω is equal to the forcing frequency, $2\pi/D \text{ d}^{-1}$ where D is 1 day and t is measured in days. Simulation C is the reference simulation.

Simulation	Geometry	Inflow speed (cm s^{-1})	Stratification
A	Ideal – no banks	8	Summer
B	Ideal – one bank	8	Summer
C	Ideal	8	Summer
D	Ideal	4	Summer
E	Ideal	12	Summer
F	Ideal	16	Summer
G	Ideal	-8	Summer
H	Ideal	$8 + 4\sin(\omega t)$	Summer
I	Ideal	8	Winter
J	Realistic	8	Summer
K	Realistic	$8 + 4\sin(\omega t)$	Summer

2.6 Results

2.6.1 The no-bank case: flow adjustment to imposed forcing

Flow over the shelf-slope region without the presence of the topographic banks (simulation A) develops over a period of about ten days. Due to the gradually imposed

forcing at the upstream boundary, the total amount of kinetic energy in the domain also slowly increases, reaching an essentially constant value by day 10. This state of constant kinetic energy can be used as a criterion for defining well-developed flow within the domain. The sea-surface height anomaly adjusts geostrophically to $\sim +1.5$ cm along the offshore boundary and to ~ -1.5 cm along the onshore boundary during the 10-day period. All results presented in the rest of this chapter are for day 14 and later.

The flow must also adjust spatially, as the purely alongshelf and uniform inflow imposed at the upstream boundary responds to bottom friction, the Coriolis effect and the sloping bathymetry within the domain. A cross-shelf gradient in the depth-averaged alongshelf velocity is set up within 10 km of the upstream boundary and persists downstream of there. The cross-shelf variation is less than 10% of the specified 8 cm s^{-1} forcing velocity.

A cross-shelf section of normalized alongshelf velocity at the midpoint of the domain shows this variation, with more rapid flow offshore and slower flow inshore (Fig. 2.4a). There is evidence of a sub-surface jet at the shelf-break depth (125 m), with a

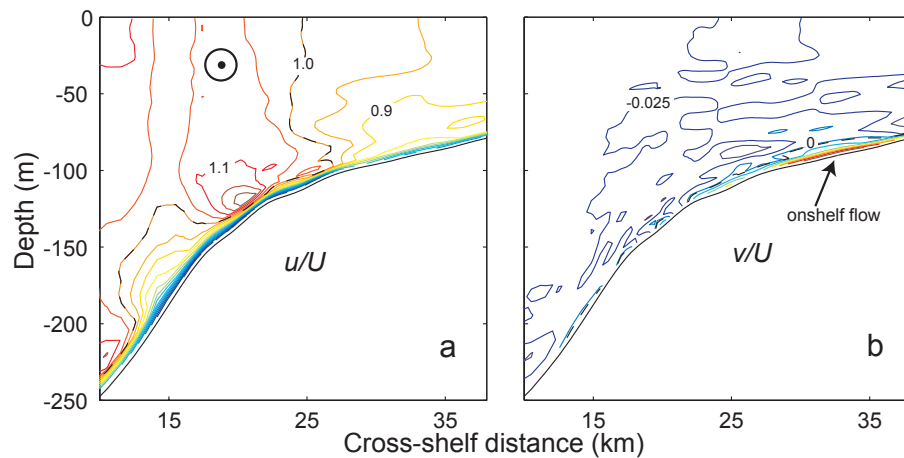


Fig. 2.4. Cross-shelf sections of velocity for simulation A. No-bank case, sections at the alongshelf midpoint of the domain, day 16. (a) Normalized alongshelf velocity (u/U). Dotted line shows $u/U = 1$, contour interval is 0.05. (b) Normalized cross-shelf velocity (v/U). Dotted line shows $v/U = 0$, contour interval is 0.025. Mean flow is out of the paper. Only part of the model domain is shown.

maximum alongshelf speed of about 9.5 cm s^{-1} . A secondary flow develops in the cross-shelf velocity component, with a weak ($\sim 0.2 \text{ cm s}^{-1}$) offshore flow through most of the domain and relatively strong onshore flow (up to $\sim 1.25 \text{ cm s}^{-1}$) confined to the bottom few meters on the shelf in the Ekman layer (Fig. 2.4b). Boyer et al. (1987) found a similar secondary flow pattern in laboratory studies. Their flow tank had a flat bottom, however, so that the near-bottom cross-channel flow extended the width of the channel.

The density structure of the flow changes very little in time and space except in the bottom-most few meters, where adjustment is made to the no-flux condition and where some transport is caused by the near-bottom cross-shelf flow described above. This boundary layer flow does not significantly impact the bulk of the fluid in the domain.

2.6.2 Flow disruption and wake interactions: one bank vs. two

The addition of a single Gaussian topographic feature (simulation B) disrupts the flow over the shelf, resulting in streamlines that diverge from those of the no-bank case

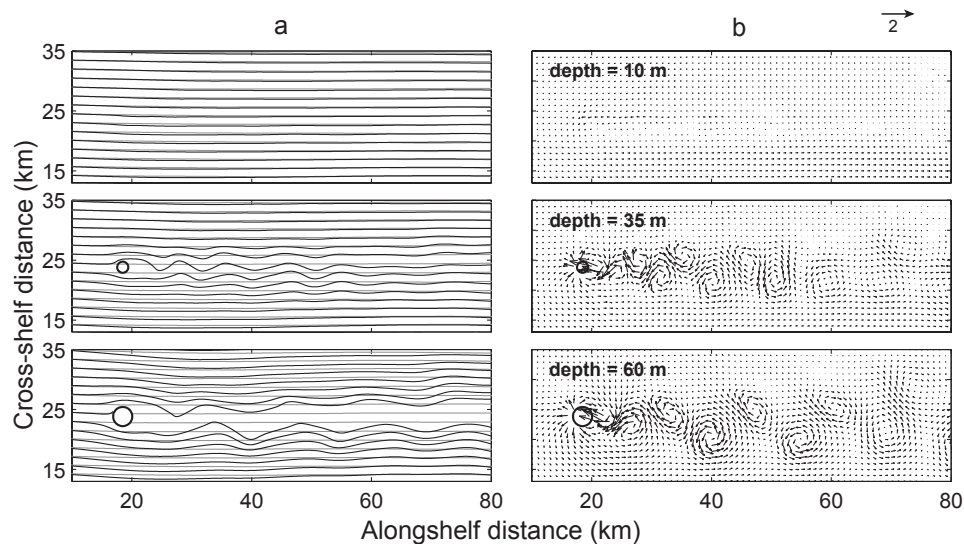


Fig. 2.5. Streamlines and velocity anomaly vectors at three depths. Day 16. (a) Instantaneous streamlines for the no-bank case (simulation A, gray lines) and the one-bank case (simulation B, black lines), (b) Instantaneous normalized velocity anomaly vectors for the one-bank case (simulation B). Normalized velocity anomaly is computed by subtracting the alongshelf forcing velocity from the model velocity and dividing by the forcing velocity (see text). Only part of the model domain is shown in each panel.

(Fig. 2.5a). Flow disruption is primarily a subsurface effect, as streamlines at 10 m depth (above the top of the bank) show only minimal deflection. Undulation of the streamlines downstream of the topographic feature reflect the formation of vortices in the immediate wake and their transport downstream with the mean flow. The characteristic sizes of the shed vortices are related to the local cross-sectional area of the feature, which increases with depth. This vortex size variation can be seen in Fig. 2.5b, which shows normalized velocity anomaly vector plots at three depths. The normalized velocity anomaly is computed by subtracting the forcing velocity (U) from the alongshelf velocity component (u), and then normalizing both the alongshelf and cross-shelf velocity (v) components by the forcing velocity (i.e. $u^* = (u - U)/U$ and $v^* = v/U$).

Cross-shelf sections of normalized velocities at the midpoint of the Gaussian bank show the structure of flow acceleration around the bank. Enhancement of the alongshelf flow is greatest at depth, where the topographic feature presents a greater cross-sectional area that the fluid must go around, i.e. where there is more blockage of the flow (Fig. 2.6a). The cross-shelf velocity is greatest near the top of the feature in this mid-point cross-section (Fig. 2.6b), although this is a consequence of bank geometry. Sections through the bank at locations other than the midpoint show cross-shelf velocity maxima at varying depths.

There is no reversed alongshelf flow above the bank which would indicate Taylor cap formation. This is expected from the relatively large Rossby number ($Ro \sim 0.37$). For instance, Chapman and Haidvogel (1992) showed that the critical Rossby number dividing stratified flows ($Bu \sim O(1)$) over Gaussian peaks into those with and without Taylor caps was $Ro_c \sim 0.14$ for a geometrical aspect ratio equal to that used in this study. Most other studies of Taylor cap formation consider Rossby numbers much smaller than 0.1.

Similar cross-shelf sections of velocity taken on a plane 3 km downstream of the bank midpoint show some of the complexity of the near-wake region. There is an area of reversed alongshelf velocity (Fig. 2.6c) that is persistent in time, but whose size and shape are very dynamic. The maximum value of the reversed flow in the snapshot shown

is approximately 80% of the forcing velocity (i.e. $\sim 6.5 \text{ cm s}^{-1}$, directed westward). The direction of the cross-shelf flow in the wake varies with depth (Fig. 2.6d), which reflects the vortex shedding process and the complex three-dimensional geometry of the vortices themselves. Cross-shelf speeds in the section shown reach nearly 7.5 cm s^{-1} ($0.94U$).

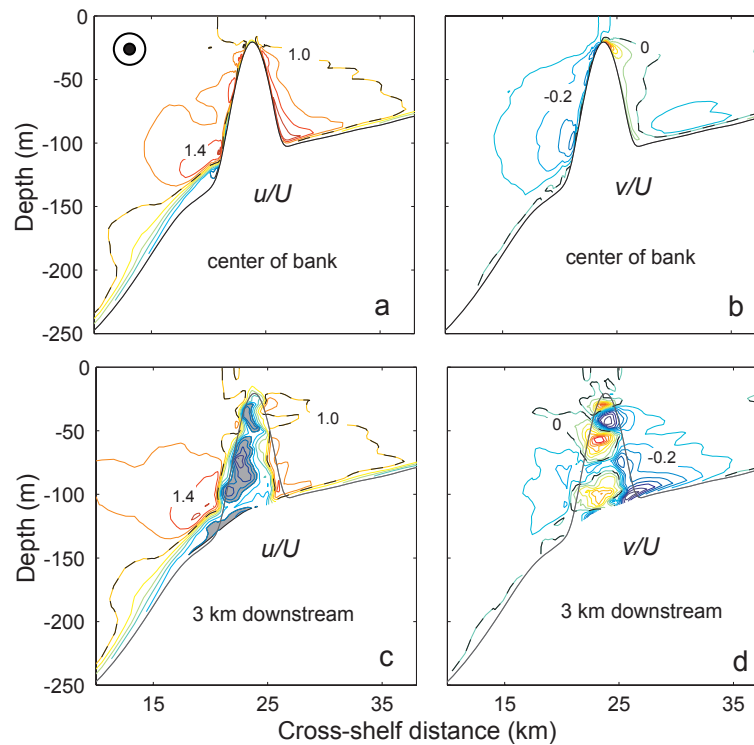


Fig. 2.6. Cross-shelf sections of velocity for simulation B. One-bank case, day 16. (a) Normalized alongshelf velocity (u/U) on a section through the center of the bank. Dotted line shows $u/U = 1$, contour interval is 0.2. (b) Normalized cross-shelf velocity (v/U) on a section through the center of the bank. Dotted line shows $v/U = 0$, contour interval is 0.1. (c) Normalized alongshelf velocity (u/U) on a section 3 km downstream of the bank. Shaded region shows $u/U < 0$, dotted line shows $u/U = 1$, contour interval is 0.2. (d) Normalized cross-shelf velocity (v/U) on a section 3 km downstream of the bank. Dotted line shows $v/U = 0$, contour interval is 0.1. Mean flow is out of the paper. Bank profile in c and d is shown for reference only and does not reflect the local bathymetry at this section. Only part of the model domain is shown.

An alongshelf section of velocity through the midpoint of the bank shows how the alongshelf flow is slowed as it approaches the bank and reverses in an irregular (and

dynamic) region in the immediate lee (Fig. 2.7a). Cross-shelf velocity contours reflect the distortion of the shed vortices, where the axis of each vortex is angled in the direction of flow, with the greatest degree of downstream bending between 20 and 50 m (Fig. 2.7b). The vortex axes become more vertical as the vortices are advected downstream. Similar vortex distortion has been observed in laboratory studies by Boyer et al. (1987) and Boyer and Zhang (1990) and in the laboratory and numerical work of Castro et al. (2001). The Boyer studies attributed the distortion to depth-dependent differences in vortex shedding frequency caused by variations in streamwise obstacle diameter, and to differences in vortex advection speeds. The Castro study refuted this explanation and instead pointed to a depth-dependent phase shift in the shedding cycle. Here, I do observe a higher shedding frequency higher in the water column ($\sim 0.7 \text{ d}^{-1}$ at 35 m vs. $\sim 0.5 \text{ d}^{-1}$ at 60 m), but find that it is stratification, rather than geometry, that

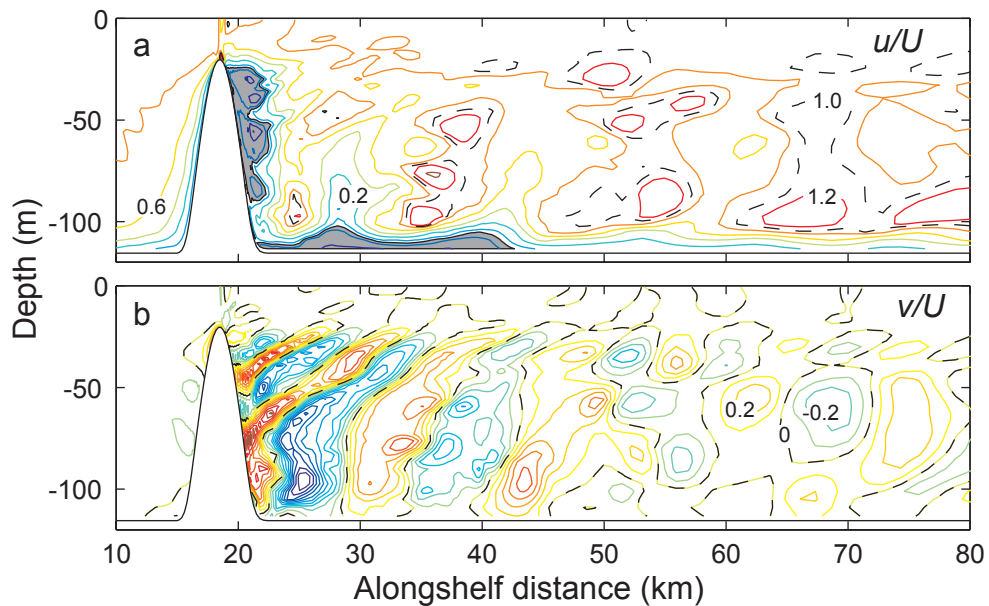


Fig. 2.7. Alongshelf sections of velocity for simulation B. One-bank case, sections through the center of the bank, day 16. (a) Normalized alongshelf velocity (u/U). Shaded area shows $u/U < 0$, dotted line shows $u/U = 1$, contour interval is 0.2. (b) Normalized cross-shelf velocity (v/U). Dotted line shows $v/U = 0$, contour interval is 0.1. Mean flow is from left to right. Only part of the model domain is shown.

appears to be the most influential factor (see below). Cross-shelf velocities in the section shown in Fig. 2.7b peak at nearly 9.5 cm s^{-1} ($1.2U$) near the bank and remain as high as 2.4 cm s^{-1} ($0.3U$) up to 50 km downstream.

In simulation C (Table 1), there is a second Gaussian peak downstream and shoreward of the first, forming a geometrical configuration that represents the geography of the Flower Garden Banks in a highly idealized sense. The seafloor and bank topographies are greatly simplified in both shape and smoothness, but the locations of the banks on the continental shelf and relative to one another are close to reality.

Streamline and velocity anomaly arrow plots at three depths show that vortices are shed from each of the banks and interact as they are advected downstream of the second bank (Fig. 2.8). Vortex interaction appears to increase with depth, where the larger shed

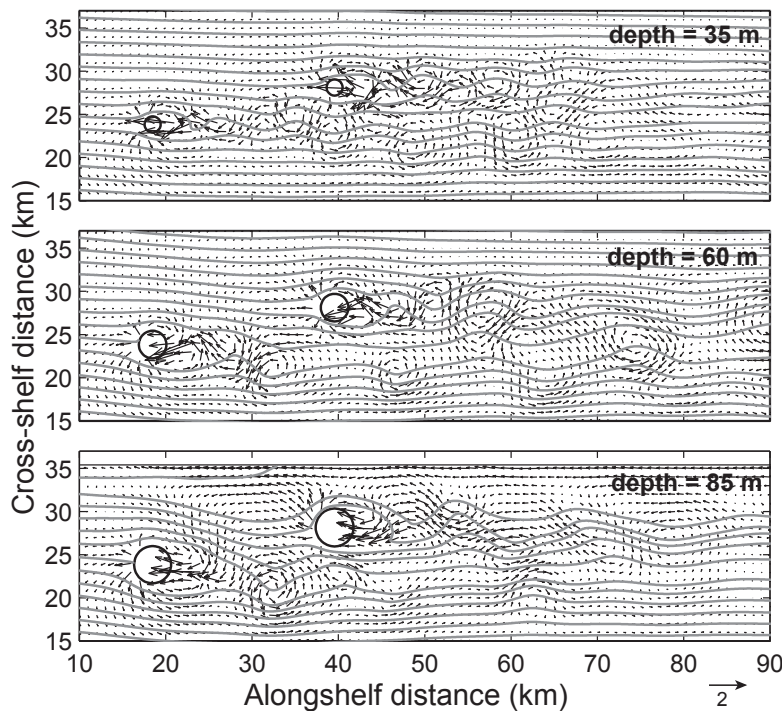


Fig. 2.8. Streamlines and velocity anomaly vectors for simulation C. Reference case, day 16. Normalized velocity anomaly is computed by subtracting the alongshelf forcing velocity from the model velocity and dividing by the forcing velocity (see text). Only part of the model domain is shown.

vortices tend to coalesce more readily than the smaller vortices that are shed nearer the tops of the banks. A dominant effect of adding a second bank is, thus, to influence the flow field downstream of both banks. Vortex coalescence results in larger characteristic vortex sizes in the far-field such that the wake there resembles one generated by flow over a single obstacle of larger cross-section rather than one generated by flow over two obstacles, each of smaller cross-section. A similar effect was documented by Zhang and Boyer (1991), who measured larger streamline undulation wavelengths downstream of two in-line interfering obstacles as compared to a single obstacle.

Velocity contour plots (not shown) for simulation C in the equivalent alongshelf and cross-shelf sections as were shown in Figs. 2.6 and 2.7 confirm that the structure of the flow field very near to each of the banks is similar to that of the single-bank case. For the upstream bank, the differences are remarkably small; for the downstream bank, the differences are more pronounced and vary in time, reflecting the influence of the vortices shed by the upstream bank. Quantitative measures of the near-wake properties and vortex shedding process for each of the banks will be presented in the next section.

2.6.3 *Ideal bathymetry: variation of inflow velocity*

In simulations C through H, I used the two-bank Gaussian bathymetry with summer density stratification and varied only the velocity forcing at the upstream boundary. Four constant eastward forcing velocities were considered as well as one westward forcing velocity and one time-varying eastward velocity.

2.6.3.1 *Steady eastward inflow: wake properties and vortex shedding*

Vortex shedding frequencies were estimated using twelve-hour snapshots of the normalized velocity anomaly fields over a period of four days. I used velocity maps taken at 60 m, near the mid-height of the Gaussian peaks. Shedding frequency, ω_e , was estimated as $\omega_e = [(x_{i+1} - x_i)/\Delta t]/X$, where $x_{i+1} - x_i$ is the distance a vortex center travels in the time interval Δt and X is the mean spacing between vortices (Boyer et al., 1987). The Strouhal number is relatively insensitive to variations in Ro for vortices shed from the upstream bank (Fig. 2.9a). $St \approx 0.2$ in each case, which agrees with computed Strouhal numbers ranging from 0.19 to 0.3 for flow past isolated cylinders and cones

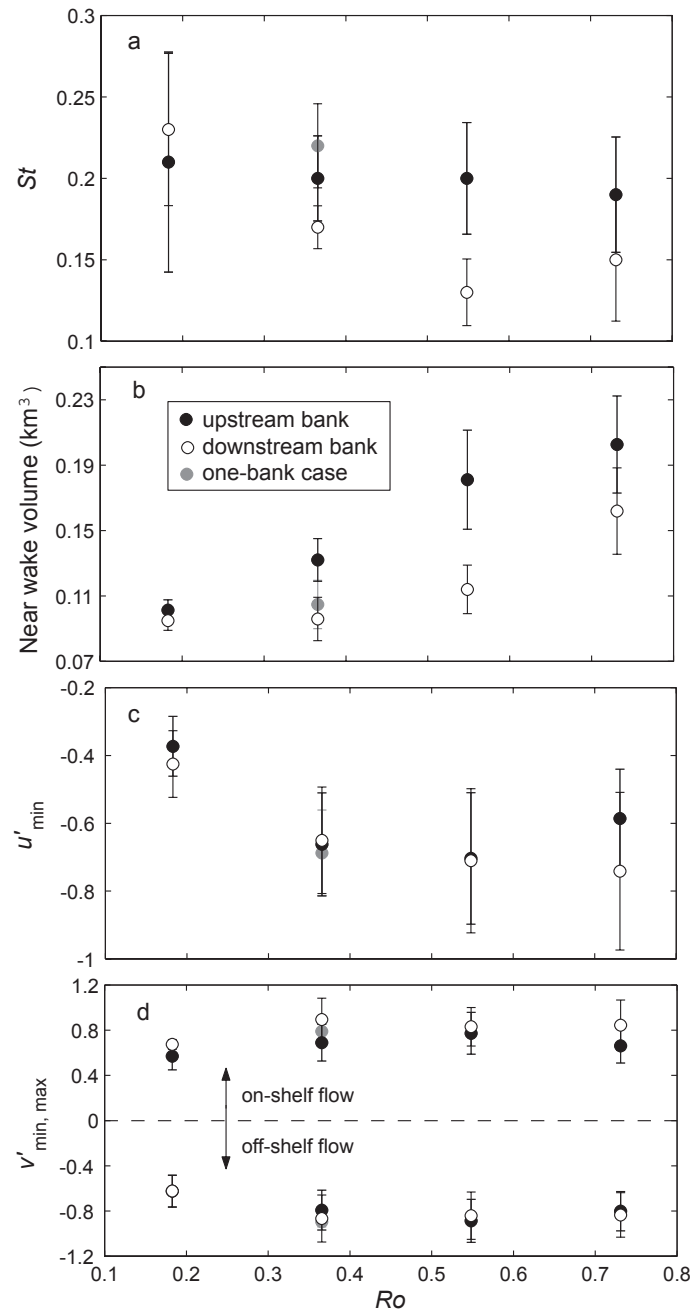


Fig. 2.9. Strouhal number, wake volume and wake velocity extrema as a function of Rossby number. Data from simulations B through F. (a) Strouhal number ($St = nL/U$) at a depth of 60 m. (b) Volume of return-flow region ($u < 0$) in the near wake. (c) Maximum speed of alongshelf return flow, normalized by forcing velocity, U . (d) Maximum cross-shelf speeds normalized by forcing velocity, U . Values shown are time averages ± 1 standard deviation (std), computed using four-hour data over four days.

(Boyer and Kmetz, 1983; Boyer et al., 1987). The Boyer et al. study found no dependence of St on Ro , but did find a slight negative dependence of St on the strength of stratification. Their strongest stratification case corresponded to a Burger number of approximately 6. Because the Burger number here is $O(10)$, I would expect the Strouhal number results to be closer to their maximum stratification case, $St \approx 0.2$.

Strouhal numbers tended to be smaller for the downstream bank, implying that the presence of the upstream bank influences the shedding process at the other bank (Fig. 2.9a). This influence is more pronounced for larger Rossby number flows, for which the downstream $St = 0.13 - 0.17$. The smallest Ro case has a downstream St that is essentially the same as that for the upstream bank. The uncertainty in St for this case is relatively large, in part because the number of vortices included in the calculations is small compared to the other cases. Bokaian and Geoola (1984) studied the vortex shedding process for two interfering cylinders at various separation distances, measuring $St \approx 0.17 - 0.2$ for separation distances similar to those used here, and also finding the shedding frequency (and hence St) of the upstream cylinder to be consistently higher than that of the downstream cylinder. They attributed this difference in St to both the change in mean flow direction as fluid is diverted around the upstream cylinder and to the upstream cylinder's shed vortices interfering with vortex generation at the downstream cylinder.

The size of the region of strong return flow observed in the immediate wakes of the topographic features (e.g. Figs. 2.6c,d; 2.7) was estimated by computing the average volume of the wake within which the alongshelf component of velocity was less than zero (i.e. opposite in direction to the forcing flow). I included only the depth band from 20 m (the tops of the peaks) down to 60 m, since the ultimate interest is in impacts on biological processes in the upper water column. Also, the barotropic nature of the inflow forcing means that flows deeper in the water column are faster in the model than they are in the field. The near-wake reversed flow volume increases with increasing Ro (Fig. 2.9b). The wake region behind the downstream bank is generally smaller than that behind the upstream bank. The influence of the upstream bank on the downstream bank

again tends to be stronger for the larger Ro (i.e. faster inflow velocity) simulations. Zhang and Boyer (1991) observed a similar strengthening of the bank-bank interaction with increasing Ro for flows past two Gaussian peaks oriented similarly to those in my simulations. They did not measure return-flow volumes, but noticed that the shape of the near wake was wider in the cross-flow direction behind the downstream peak than behind the upstream peak. I observed a similar trend in my simulations (not shown), with the wakes behind the downstream bank being generally wider, but also shorter, than those behind the upstream bank, such that the total volume was smaller for the downstream bank. This difference in near-wake shapes and volumes can again be explained in terms of flow deflection in the gap between the two banks and the influence of vortices shed from the upstream bank on flow past the downstream bank, both of which are expected to be greater for larger Ro flows.

The minimum alongshelf velocity (i.e. maximum return velocity) and the minimum and maximum cross-shelf velocities in larger wake regions behind each bank, all normalized by inflow velocity, show little variation between the upstream and downstream banks (Fig. 2.9c,d). For this figure, the wake regions considered extended approximately 14 km downstream of each bank and covered approximately 6 km in the cross-shelf direction, with a depth range of 20 to 60 m. Both the strength and variability of the maximum normalized return flow increase with Ro , with values tending to flatten out as they approach 0.8 (i.e. return flow speed approaching 80% of forcing speed) (Fig. 2.9c). In absolute terms, the return velocities do not tend to taper off but continue increasing with faster inflow.

Maximum normalized on-shelf and off-shelf flows in the wake regions vary little for $Ro > 0.3$ (Fig. 2.9d). Off-shelf velocities are $\sim 10\%$ larger than on-shelf velocities for the upstream bank, but this small difference disappears for the downstream bank. The absolute magnitudes of the cross-shelf velocities are larger when inflow speed is faster, which might imply a larger region of influence of the wake in the cross-shelf direction for faster inflows. I was unable, however, to measure a difference in the widths of the wakes for the different Rossby number cases. Faster alongshelf inflows generate

stronger cross-shelf flows, but may also serve to limit their cross-shelf extent.

2.6.3.2 Steady eastward inflow: cross-shelf transport

I investigated the potential for interbank exchange of water, and by extension any chemical constituents or particles it contains, by computing average cross-shelf volume transport through a vertically oriented plane between the two banks. Since the banks are offset in the cross-shelf direction, cross-shelf transport is necessary for interbank exchange. The plane considered was midway between the banks in the cross-shelf direction and oriented in the alongshelf direction, extending from 4 km downstream of the upstream bank to 4 km upstream of the downstream bank over the depth range 20 to 60 m. Positive transport through the plane (i.e. transport in the on-shelf direction) would favor exchange from the upstream to the downstream bank. Positive transport through the plane does occur intermittently in both time and space, but the average transport in all cases is negative, indicating overall off-shelf flow between the banks. The magnitude of off-shelf transport is larger for larger Rossby number inflows, ranging from $\sim 2000 \text{ m}^3 \text{ s}^{-1}$ for $Ro = 0.18$ to $\sim 10,000 \text{ m}^3 \text{ s}^{-1}$ for $Ro = 0.74$. The Coriolis effect and the deflection of flow in the gap between the banks produce consistent off-shelf flow that is not counteracted, at least in a time-averaged sense, by the spatially and temporally sporadic on-shelf flows associated with shed vortices. I expect interbank exchange to decrease with increasing inflow velocity.

2.6.3.3 Steady eastward inflow: vorticity and isopycnal displacements

The vortices shed from the Gaussian peaks are associated with enhanced relative vorticity and density perturbations in the flow field. Near-surface density surfaces undergo an abrupt deflection as flow passes just over the tops of the banks, while the isopycnals show broad, wave-like patterns in the wake regions (Fig. 2.10a). The abrupt density perturbations near the bank tops are associated with a hydraulic jump flow pattern and are similar in structure to those modeled by Chapman and Haidvogel (1993) for seamounts and measured by Nash and Moum (2001) over a small bank on the continental shelf. The phenomenon will be explored further in the next section. The wave-like undulations of isopycnals in the wakes of the banks reflect the same

downstream bending as do the shed vortices and persist for more than 50 km downstream of each bank. The amplitude of the undulations extending $\sim 10\text{-}15$ km downstream of the banks increases with faster inflow velocities, ranging from ~ 0.5 m for $U = 4 \text{ cm s}^{-1}$ to ~ 2.3 m for $U = 16 \text{ cm s}^{-1}$.

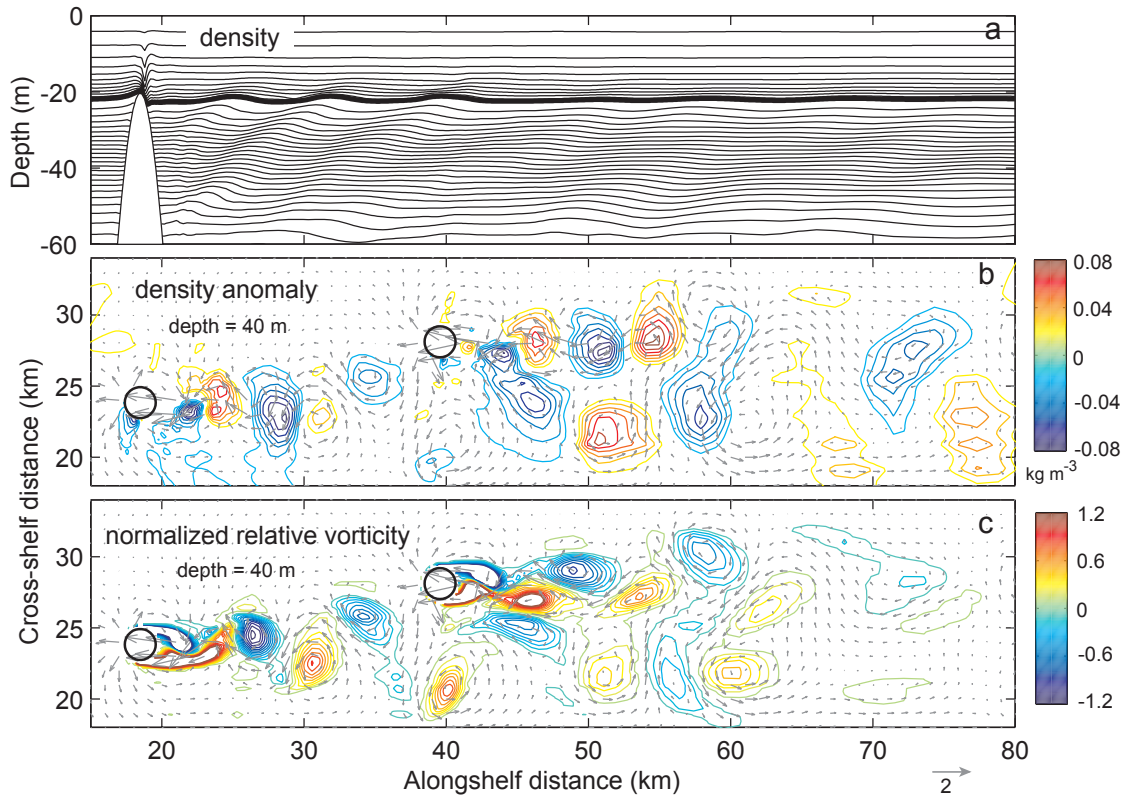


Fig. 2.10. Isopycnal displacements and relative vorticity for simulation C. Reference case, day 16. (a) Potential density contours on an alongshelf section through the middle of the upstream bank. Thick line corresponds to 23 kg m^{-3} . Above this, the contour interval is 0.02 kg m^{-3} ; below, the contour interval is 0.1 kg m^{-3} . (b) Potential density anomaly and normalized velocity anomaly vectors at 40 m depth. Density anomaly contour interval is 0.01 kg m^{-3} , with the zero contour suppressed. (c) Relative vorticity normalized by the Coriolis parameter and normalized velocity anomaly vectors at 40 m depth. Normalized relative vorticity contour interval is 0.1, with the zero contour suppressed. Normalized velocity anomaly is computed by subtracting the alongshelf forcing velocity from the model velocity and dividing by the forcing velocity (see text). Only part of the model domain is shown in each panel.

The density anomalies at 40 m tend not to align with vortex centers but to occur around the edges and in regions between two counter-rotating vortices (Fig. 2.10b). Temperature variations associated with the density perturbations in the wake are on the order of ~ 0.15 to 0.65 °C at 40 m and depend on Ro . This variability is too small to have a significant impact on temperature-dependent biological processes such as phytoplankton growth rate.

Contours of relative vorticity ($\zeta = \partial v/\partial x - \partial u/\partial y$) normalized by the Coriolis parameter help to delineate the locations and boundaries of the shed vortices and demonstrate the diminishment of their strength with distance downstream (Fig. 2.10c). Relative vorticity exceeds planetary vorticity (i.e. $\zeta/f > 1$) only in the vortex formation regions immediately downstream of each bank and, occasionally, at the centers of shed vortices that are within ~ 10 km of a bank. The maximum magnitude of normalized relative vorticity in the wakes increases with the Rossby number (Fig. 2.11). For the faster inflow cases, the maximum relative vorticity is $O(10f)$, which is in agreement with measurements of enhanced vorticity in the wake of an isolated deep-ocean island made by Hasegawa et al. (2004).

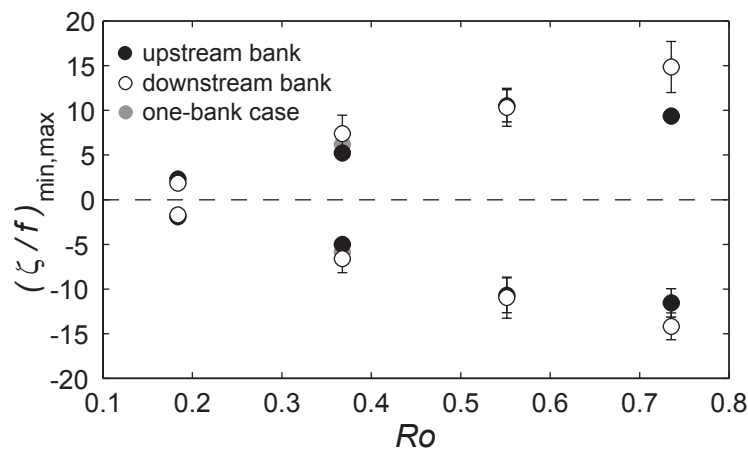


Fig. 2.11. Normalized relative vorticity as a function of Rossby number. Maximum and minimum values, normalized by Coriolis parameter. Data from simulations B through F, showing time averages ± 1 std, computed using four-hour data over four days. Depths were limited to shallower than 60 m.

2.6.3.4 Steady eastward inflow: turbulent mixing

The pattern of abrupt isopycnal displacements associated with accelerating flow over the bank tops produced by the model (Fig. 2.12a) closely resembles measurements made by Nash and Moum (2001) over a small bank on the continental shelf. The flows they measured were described in terms of internal hydraulic jump dynamics and were associated with enhanced drag coefficients and turbulent mixing over the top of the bank. The modeled turbulent mixing rates, as represented by the vertical eddy diffusivity, K_v , were similarly enhanced in the vicinity of the topographic peaks.

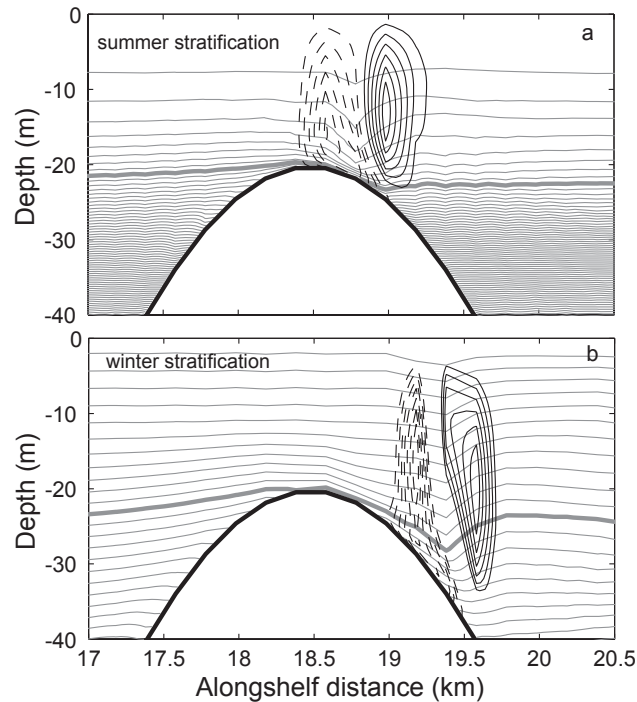


Fig. 2.12. Density structure and vertical velocity contours. Alongshelf sections through the center of the upstream bank, day 16. (a) Simulation C (reference case). Thick gray line corresponds to 23 kg m^{-3} . Density contour interval is 0.025 kg m^{-3} . Vertical velocity contours range from -0.12 to 0.12 by 0.02 cm s^{-1} , with dashed lines denoting negative velocities and the zero contour suppressed. (b) Simulation I (winter stratification case). Thick gray line corresponds to 25.32 kg m^{-3} . Density contour interval is 0.01 kg m^{-3} . Vertical velocity contours range from -0.22 to -0.10 by 0.02 cm s^{-1} and from 0.10 to 0.22 by 0.02 cm s^{-1} , with dashed lines denoting negative velocities. Mean flow is from left to right.

Maximum values of K_v near the bank tops increased with Rossby number, ranging from $\sim 4 \times 10^{-5} \text{ m}^2 \text{ s}^{-1}$ for the smallest Ro case to $\sim 1 \times 10^{-2} \text{ m}^2 \text{ s}^{-1}$ for the largest Ro case (Fig. 2.13). The background value of K_v used in the model was $1 \times 10^{-5} \text{ m}^2 \text{ s}^{-1}$, which is typical of continental shelf regions (Moum and Nash, 2000). Maximum enhancement of turbulent mixing over the bank tops is thus ~ 4 –1000 times the background rate. This result is supported by several studies which have measured and modeled topographically generated turbulence enhancement of 100–10,000 times background rates (Lueck and Mudge, 1997; Nash and Moum, 2001; Lavelle et al., 2004). Maximum vertical eddy diffusivities in the wake regions behind the banks were smaller than those found near the bank tops, but were still ~ 10 –100 times the background for all but the lowest Rossby number case (Fig. 2.13).

The maximum vertical speeds associated with the hydraulic jump flow pattern (Fig. 2.12a) also increase in magnitude with increasing Ro , from $\sim 0.04 \text{ cm s}^{-1}$ for the 4 cm s^{-1} inflow case to $\sim 0.64 \text{ cm s}^{-1}$ for the 16 cm s^{-1} inflow case.

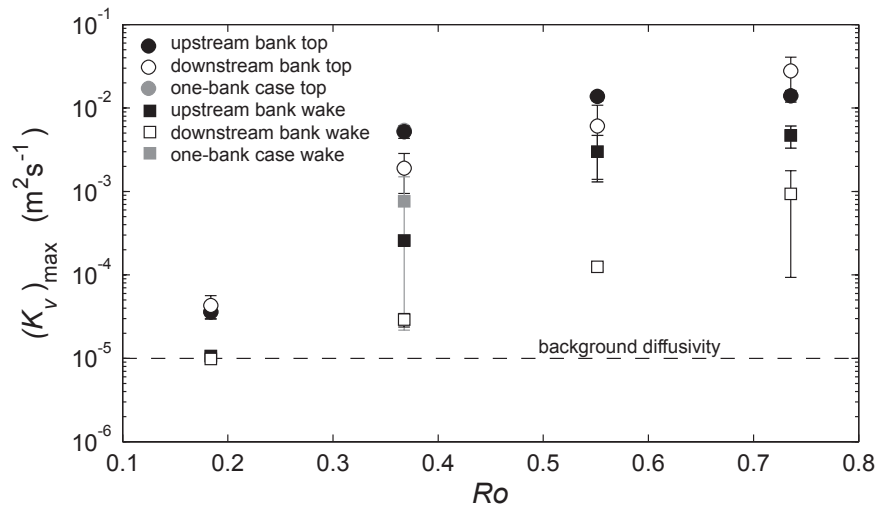


Fig. 2.13. Maximum vertical eddy diffusivity as a function of Rossby number. Data from simulations B through F. Values shown are time averages ± 1 std, computed using four-hour data over one day. Background vertical eddy diffusivity specified in the model is $10^{-5} \text{ m}^2 \text{ s}^{-1}$, shown by dashed line.

2.6.3.5 *Steady westward inflow*

In simulation G, the inflow velocity was reversed to be from east to west rather than west to east but its speed remained 8 cm s^{-1} . Because the relative positions of the two peaks were unchanged, the upstream bank was now shoreward of the downstream bank. The flow patterns and associated phenomena observed are very similar to those of the reference case, with nearly identical results for maximum wake return velocities; minimum and maximum cross-shelf wake velocities; isopycnal displacements and maximum vertical velocities near the bank tops; and enhancement of relative vorticity and vertical eddy diffusivity in the wake regions. The Strouhal number results were also similar, with the upstream bank having $St \approx 0.2$. The downstream bank had a lower St indicative of slightly less frequent vortex shedding. For the reference case, the reduction in shedding frequency at the downstream bank was $\sim 15\%$, whereas the reduction was $\sim 30\%$ for simulation G ($St \approx 0.17$ vs. $St \approx 0.14$). This difference suggests that the influence of the upstream bank on flow patterns around the downstream bank may be somewhat larger for the reversed flow case.

The results for cross-shore volume transport between the two banks support the ideal of an enhanced downstream effect of reversed flow. For the reference case, there was a net off-shelf transport which would tend to inhibit interbank exchange. For the reversed flow case, the same mechanisms of flow deflection in the gap between the banks and the Coriolis effect promote on-shelf flow, which would again work against interbank exchange. The net volume transport computed in this case is in fact positive, and thus directed onshore, but its magnitude is less than half that of the reference case ($1.38 \times 10^3 \text{ m}^3 \text{ s}^{-1}$ vs. $3.23 \times 10^3 \text{ m}^3 \text{ s}^{-1}$).

A final significant difference between the eastward and westward flow cases involves the near-wake volumes, where alongshelf velocity is directed back toward each bank (cf. Fig. 2.9b). These regions of return flow tend to be larger when inflow is from the east ($\sim 0.15 \text{ km}^3$ vs. $\sim 0.11 \text{ km}^3$). Boyer and Davies (1982) observed a similar difference in near-wake size when they compared experimental results for eastward vs. westward flow past a cylinder on a β -plane. For eastward inflows, the β -effect tended to

delay the separation of flow around the cylinder, resulting in a small wake area. For westward inflows, β -plane effects promoted early flow separation and resulted in relatively larger wakes. (Recall that northward deflection of flow on a β -plane induces negative relative vorticity—clockwise rotation, while southward deflection induces positive relative vorticity—counter-clockwise rotation. When considering deflection of flow around a cylinder, these effects lead to early separation for westward flows and delayed separation for eastward flows). In the f -plane model, the sloping topography of the shelf may be similarly influencing flow-separation points and thus leading to different wake volumes (the relative vorticity arguments are essentially the same).

2.6.3.6 *Unsteady eastward inflow*

In simulation H, the forcing at the upstream boundary was imposed as a sinusoidal wave with an average value of 8 cm s^{-1} , an amplitude of 4 cm s^{-1} and a period of 1 day, i.e. $U = 8 + 4\sin(2\pi t/D)$, where D is the period and t is measured in days. Streamlines and normalized velocity anomalies develop over the course of a single forcing cycle (Fig. 2.14). Starting (arbitrarily) at a time of minimum inflow forcing (Fig. 2.14a, $t = 0 \text{ d}$, $U = 4 \text{ cm s}^{-1}$), the acceleration phase of the forcing cycle results in the ‘straightening out’ of streamlines and a concomitant reduction in cross-shelf excursions of the flow (Fig. 2.14b, $t = 0.25 \text{ d}$, $U = 8 \text{ cm s}^{-1}$; and 2.14c, $t = 0.5 \text{ d}$, $U = 12 \text{ cm s}^{-1}$). During the deceleration phase of the forcing cycle, the cross-shelf meanderings of the streamlines reappear (Fig. 2.14d, $t = 0.75 \text{ d}$, $U = 8 \text{ cm s}^{-1}$) and the flow returns to a pattern characteristic of minimum inflow forcing, from which the cycle begins again (Fig. 2.14e, $t = 1 \text{ d}$, $U = 4 \text{ cm s}^{-1}$). Note the dramatically different flow at $t = 0.25 \text{ d}$ and $t = 0.75 \text{ d}$, which correspond to times in the forcing cycle when $U = 8 \text{ cm s}^{-1}$ (Fig. 2.14b,d). Flow patterns are strongly dependent on whether the flow is accelerating or decelerating, consistent with previous studies by Boyer and Zhang (1990) and Zhang and Boyer (1991).

The normalized velocity anomaly arrows demonstrate that vortex shedding occurs during all phases of the flow cycle (Fig. 2.14). Strouhal numbers computed using the mean forcing velocity of 8 cm s^{-1} are within the range computed for steady flows of

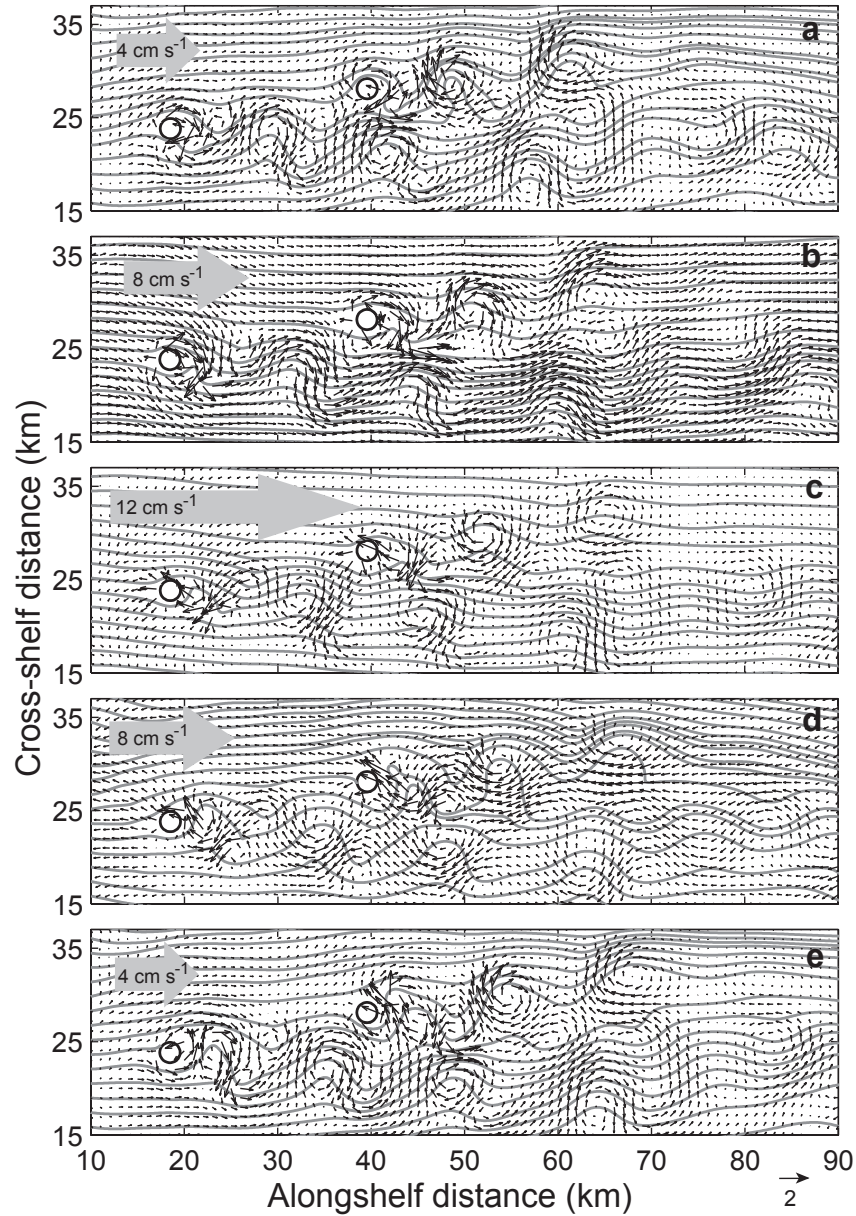


Fig. 2.14. Streamlines and velocity anomaly vectors for simulation H. Snapshots at five times during the sinusoidal forcing period, beginning on day 16. Depth is 40 m. (a) Minimum inflow phase, $t = 0$ hr, $U = 4 \text{ cm s}^{-1}$. (b) Acceleration phase, $t = 6$ hr, $U = 8 \text{ cm s}^{-1}$. (c) Maximum inflow phase, $t = 12$ hr, $U = 16 \text{ cm s}^{-1}$. (d) Deceleration phase, $t = 18$ hr, $U = 8 \text{ cm s}^{-1}$. (e) Minimum inflow phase, $t = 24$ hr, $U = 4 \text{ cm s}^{-1}$. Normalized velocity anomaly is computed by subtracting the (time-dependent) alongshelf forcing velocity from the model velocity and dividing by the forcing velocity (see text). Only part of the model domain is shown in each panel.

4 to 12 cm s⁻¹ and reflect the same influence of the upstream bank on the downstream bank as was seen for the steady flows ($St = 0.23$ for the upstream bank, $St = 0.20$ for the downstream bank). Values for many of the other metrics used to characterize the flow for the steady inflow cases, including the near-wake volumes, maximum vertical and return velocities, cross-shelf transport, maximum relative vorticities and maximum vertical eddy diffusivities, generally fell between the results for the 8 and 12 cm s⁻¹ steady-inflow cases. The time-varying forcing led to standard deviations on these quantities that were 2 to 10 times larger than for the steady-inflow cases. The near-wake volumes were an especially interesting case, because although they were on average about the same size as for the 8 cm s⁻¹ steady inflow case, their characteristics over the course of a cycle were quite different. The wakes were largest when the inflow was at its minimum value. They were swept out of existence during the accelerating phase of the inflow, only to form again as the flow decelerated. This highly transient nature of the return-flow wake volumes implies that any biological effects associated with the wakes—accumulation of biomass, for instance—will be similarly intermittent.

The maximum cross-shelf velocities in the wake regions behind the banks are significantly larger for the unsteady-inflow case than for any of the steady-inflow cases. Broader cross-shelf distributions of potential density anomaly and relative vorticity signatures (Fig. 2.15) may be related to this strong cross-shelf flow. The cross-shelf extent of the wake region is wider for the unsteady-forcing case as compared to the steady-forcing case (cf. Fig. 2.10), and implications for cross-shelf dispersal of chemical tracers and particles are expected to be significant.

2.6.4 *Ideal bathymetry: summer vs. winter stratification*

The influence of stratification was explored in simulation I (Table 1) by initializing the model with the winter temperature profile (Fig. 2.3), but maintaining all other model conditions as in the reference case (simulation C). Strouhal numbers, computed at 60 m, are indistinguishable from those computed for the reference case ($St \approx 0.2$), and correspond to a vortex shedding frequency of ~ 0.43 d⁻¹. At 35 m, the shedding frequency for the winter stratification case was unchanged, at 0.43 d⁻¹, whereas

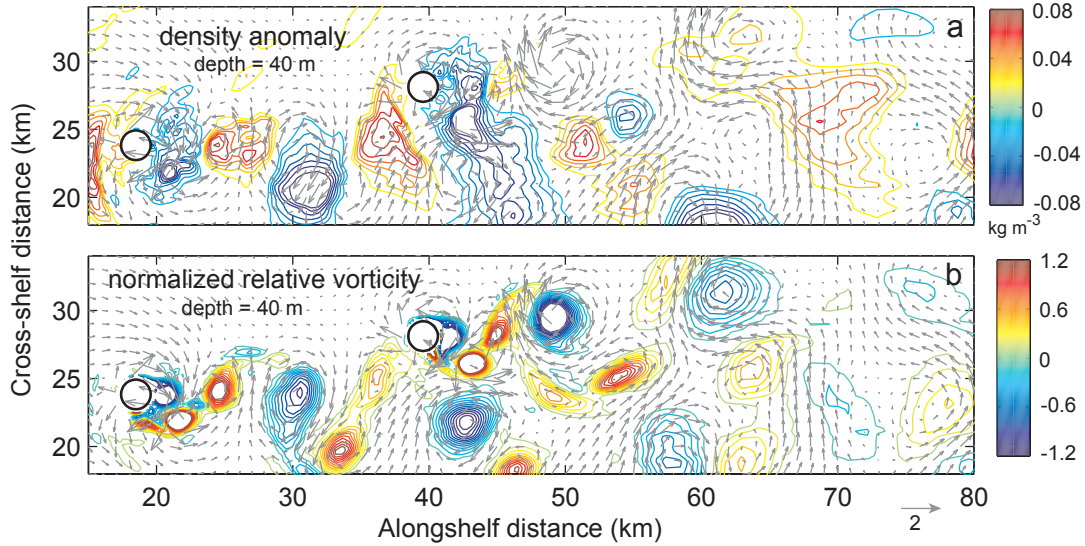


Fig. 2.15. Density anomaly and relative vorticity for simulation H. Periodic forcing case, snapshots during the acceleration phase. (a) Potential density anomaly and normalized velocity anomaly vectors. Density anomaly contour interval is 0.01 kg m^{-3} , with the zero contour suppressed. (b) Relative vorticity normalized by the Coriolis parameter and normalized velocity anomaly vectors. Normalized relative vorticity contour interval is 0.1, with the zero contour suppressed. Normalized velocity anomaly is computed by subtracting the alongshelf forcing velocity from the model velocity and dividing by the forcing velocity (see text). Only part of the model domain is shown.

for the summer stratification case it increased to $\sim 0.7 \text{ d}^{-1}$. This implies that water column stratification has a strong influence on the dynamics of vortex shedding. Alongshelf sections of velocity for the winter stratification case (Fig. 2.16) show how the flow disturbances extend throughout the water column, rather than being confined to depths below the tops of the banks (cf. Fig. 2.7). The downstream bending of vortices apparent in the summer stratification case also is absent. The strong pycnocline at 35 m in the summer case allows for the flow in the surface layer to be effectively disconnected from that in lower layers. In addition, the maximum in buoyancy frequency at 35 m in the summer (Fig. 2.3) leads to more frequent vortex shedding at this depth than deeper in the water column, where the local strength of stratification is smaller. This effect was not seen for the winter case, where stratification strength is nearly constant in the upper 100

m (Fig. 2.3). Increased stratification has been shown to enhance flow instabilities in obstacle wakes (Boyer et al., 1987; Castro et al., 2001), which may help to explain the variation in vortex shedding frequency with depth for the summer stratification case.

Vertical motions in the flow were less restricted for the winter case than for the summer case, which is an expected consequence of the reduced strength of stratification in winter. Density and vertical velocity contours near the top of the upstream bank in winter (Fig. 2.12b) show greater deflection of density surfaces and stronger vertical motions than for the summer reference case (Fig. 2.12a). Maximum vertical speeds for the winter simulation were approximately twice those for the summer simulation (~ 0.32 vs. ~ 0.16 cm s^{-1}). Associated with the enhanced vertical motions were enhanced vertical eddy diffusivities, which were four to five times larger for the winter stratification case as compared to summer.

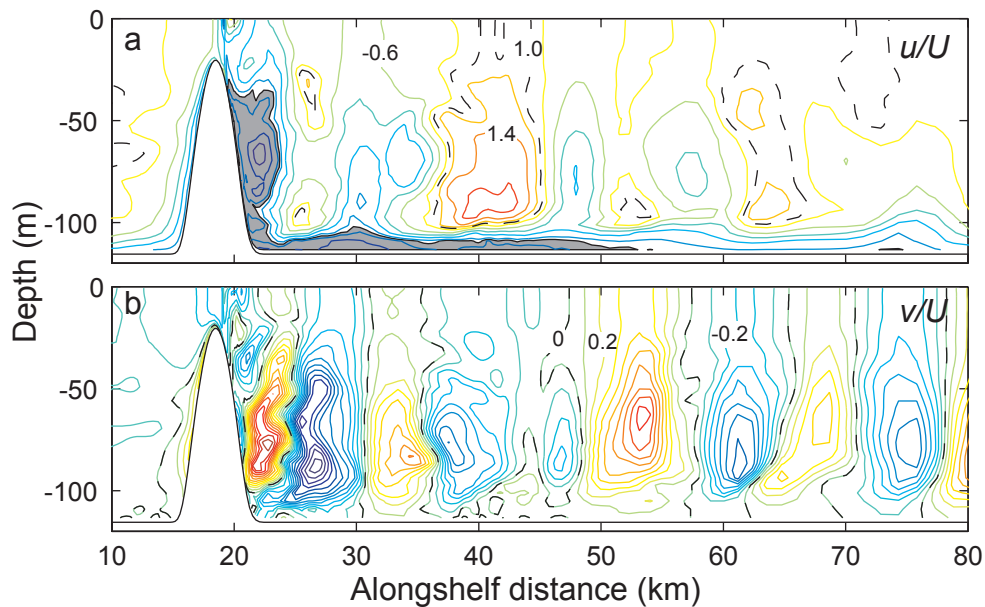


Fig. 2.16. Alongshelf sections of velocity for simulation I. Winter stratification case, sections through the center of the upstream bank, day 16. (a) Normalized alongshelf velocity (u/U). Shaded area shows $u/U < 0$, dotted line shows $u/U = 1$, contour interval is 0.2. (b) Normalized cross-shelf velocity (v/U). Dotted line shows $v/U = 0$, contour interval is 0.1. Only part of the model domain is shown.

2.6.5 Realistic bathymetry: steady and unsteady inflows

In simulations J and K (Table 1), the more realistic bathymetry (Fig. 2.2b) was used in place of the idealized shelf/slope and Gaussian peaks. Simulation J incorporated steady eastward forcing at 8 cm s^{-1} while simulation K used the same periodic forcing as was used for simulation H (section 5.3.5).

Comparison of the bathymetric profiles through the centers of the banks in the alongshelf and cross-shelf directions (Fig. 2.17a-c) reveals that the more realistic banks are generally wider near their bases and narrower near the tops than the Gaussian shapes. The west bank has neighboring features to the west and north that rise to 50-75 m, while the east bank is more clearly an isolated peak. Cross-sectional area comparisons at three

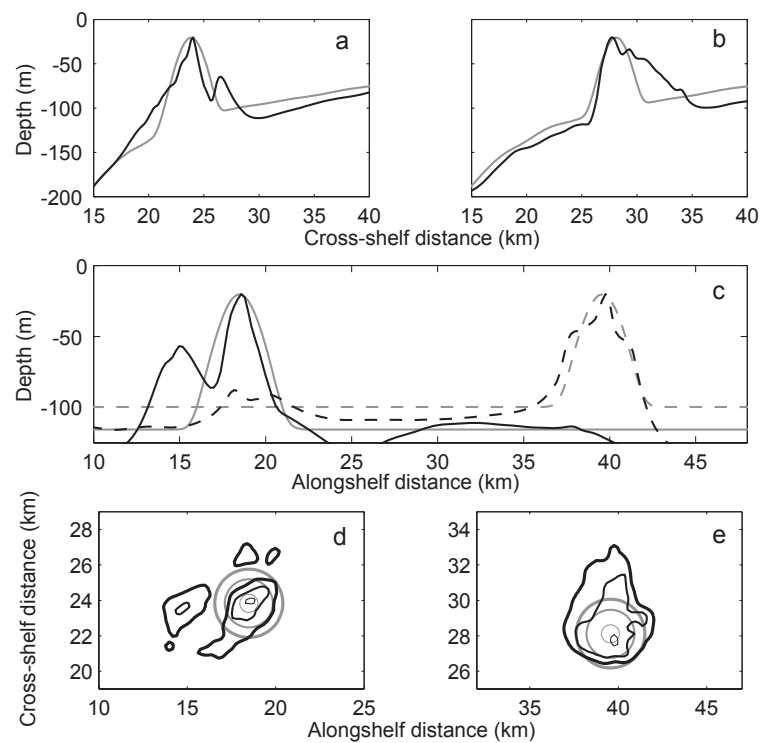


Fig. 2.17. Comparison of idealized and more realistic bathymetries. Gray lines – idealized bathymetry; black lines – more realistic bathymetry. (a), (b) Cross-shelf sections through middle of west bank (a) and east bank (b). (c) Superimposed alongshelf sections through middle of west bank (solid lines) and middle of east bank (dashed lines). (d), (e) Cross-sectional areas of west bank (d) and east bank (e) at 25 m (thin lines), 50 m (medium lines) and 75 m (thick lines).

depths show that the west bank (Fig. 2.17d) has a narrow, elliptical cross-section down to about 50 m, then broadens into an area of several peaks by about 75 m. The east bank (Fig. 2.17e) also has a very narrow pinnacle at its peak but it broadens as a single feature, beginning at about 40 m, into a shape that is less streamlined in the alongshelf direction than the Gaussian circles (i.e. it presents more of a bluff-body shape to alongshelf flow).

Streamlines at 60 m for the steady inflow case (Fig. 2.18) are deflected around each of the banks and tend to follow the shelf/slope bathymetric contours downstream of the two. Vortices were shed only sporadically from the west bank, and only cyclonic vortices persisted downstream to any distance (there is one centered at about 42 km in Fig. 2.18). Occasional anticyclonic vortices were shed from the east bank, but the wake there was primarily characterized by a wide region of strong return flow. Vortex shedding was not regular enough in either case to estimate a Strouhal number; the irregular bank shapes were sufficient to disrupt consistent vortex generation behind each of the banks.

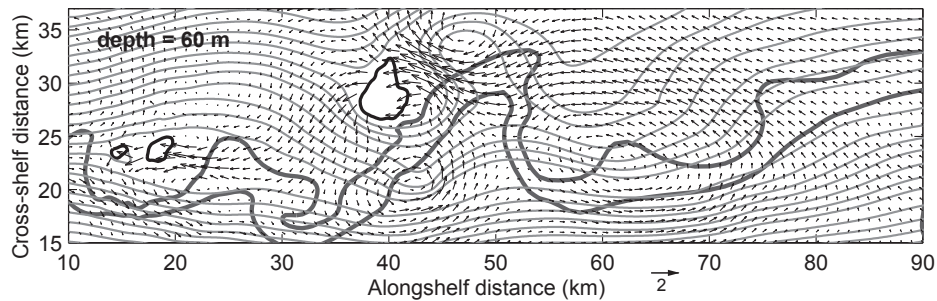


Fig. 2.18. Streamlines and velocity anomaly for simulation J. Realistic bathymetry, steady forcing case. Thick black line is the 60 m depth contour. Thick gray lines show contours at 125 m and 150 m. Thin gray lines are streamlines. Normalized velocity anomaly is computed by subtracting the alongshelf forcing velocity from the model velocity and dividing by the forcing velocity (see text). Only part of the model domain is shown.

The average return-flow wake volume behind the more realistic west bank was about equal to that behind its Gaussian counterpart ($0.169 \pm 0.060 \text{ km}^3$ real vs. 0.132 ± 0.013

km³ Gaussian). For the east bank, the bluff shape of the more realistic bathymetry led to a large increase in the average volume of return flow, from 0.096 ± 0.013 km³ to 0.507 ± 0.240 km³. The maximum return velocities within these wake volumes were not significantly different for the Gaussian vs. realistic cases for either bank. Minimum and maximum cross-shelf velocities in the wake regions were also comparable for the two different bathymetries, suggesting that the strength of the inflow was more important than the details of the bathymetry in determining cross-shelf and return flow speeds in the wake.

Flow deflection around the banks and the non-uniform shape of the shelf in the area between the banks led to an average off-shelf volume transport there that was nearly twice that estimated for the Gaussian case. Thus, conditions were even less conducive to interbank exchange of material when realistic bathymetry was used in place of the Gaussian simplification.

The steepness of the banks near their summits led to maximum vertical velocities and eddy diffusivities that were 2 to 2.5 times larger than those for the equivalent Gaussian bank simulation. The relative enhancement of turbulent diffusivity over the background value remained at the same order of magnitude, however, so that use of a much simplified topography may be justified for model studies focused primarily on topographically generated increases in turbulent mixing rates.

In simulation K, the realistic bathymetry domain was subject to periodic rather than steady forcing. Many of the differences noted in section 5.3.5 between the unsteady and steady forcing on the Gaussian bathymetry were also apparent for the more realistic bathymetry case. In particular, maximum cross-shelf velocities in the wakes and maximum vertical velocities and eddy diffusivities near the bank tops were about twice as large for unsteady forcing as for steady forcing, with the variabilities in these quantities 2 to 10 times higher. The wake volume effect seen in the unsteady Gaussian case was also observed here, with formation of large reversed-flow wake regions coinciding with the deceleration and minimum-inflow phases, and destruction of these return-flow regions coinciding with the acceleration and maximum-inflow phases.

2.7 Discussion

The topography, hydrography and forcing parameters of the model system are based on conditions at the Flower Garden Banks, on the continental shelf of the Gulf of Mexico. Model results, using both steady and unsteady forcing over Gaussian representations of the two banks, indicate that the flow can be characterized by vigorous vortex shedding and its associated effects on density-surface perturbations and turbulent mixing rates. The Rossby numbers associated with the flows considered vary from ~ 0.2 to ~ 0.8 , which is in the range both predicted and observed to be characteristic of the vortex-shedding flow regime (Boyer and Zhang, 1990; Zhang and Boyer, 1991; Chapman and Haidvogel, 1991; Coutis and Middleton, 2002). The large Rossby numbers preclude the formation of Taylor caps over the banks, in contrast to what is often observed for more typical, well-studied seamounts, which have larger horizontal length scales and are subject to deep-ocean currents which are generally much slower than the near-surface currents considered here. The water-parcel trapping and isopycnal doming effects associated with Taylor caps are thus not significant in this system.

For the steady inflow cases (simulations C through G), faster inflows generally result in more vigorous activity over the tops and in the wakes of the banks. Vortex shedding frequencies increased, although Strouhal numbers, which normalize shedding frequency by inflow velocity, remained nearly constant. Because vortex formation times are greatest for slowest inflows, retention of particles or accumulation of biomass in these formation regions, very near to each bank, should be greatest for the slowest inflow. Working against this expectation, however, are the sizes of the near-wake regions and the magnitudes of the return flows within them, both of which increase with increasing Rossby number (inflow). Cross-shelf velocities in the wake regions also increase with faster inflow, which implies a greater potential for cross-shelf transport at larger Rossby numbers. The net effect of these various interacting and sometimes counteracting wake properties on particle and plankton dynamics is not obvious. Coutis and Middleton (2002) found that the particle retention potential of an island wake was extremely sensitive to variations in incident current speed and also to the precise timing of particle

release. As a result, they found it very difficult to make generalizations regarding particle capture or retention.

My efforts to gauge interbank exchange potential using estimates of cross-shelf volume transport through a plane situated between the banks led me to expect less exchange from the upstream bank to the downstream bank for faster inflows. This averaged volume transport, however, does not necessarily reflect the actual mass transport of a dissolved chemical constituent or the transport of individual particles such as larvae. In the case of a dissolved chemical, the advective rate of transport is given by the product of the advective velocity and the chemical concentration at each point in the flow field. Additional transport occurs via turbulent diffusion and depends on velocity fluctuations. Variability in the velocity field and horizontal gradients of chemical concentration can thus be very important to the transport calculation. In the case of individual particles, a Lagrangian approach must be taken in order to accurately estimate transport.

The amplitudes of the wave-like undulations of isopycnals in the wakes of the banks increases when the forcing inflow is increased, but are small in all cases (~ 0.5 to 2.5 m). The temperature changes associated with these vertical displacements are also small and, hence, biologically irrelevant. The biological impact of the isopycnal deflections might be stronger in terms of the relative change in concentration of a biologically important nutrient such as nitrate. Nitrate tends to be depleted in surface waters of the ocean. Near the Flower Garden Banks in the Gulf of Mexico in the summer, nitrate concentration is near zero from the surface down to about 50 m, where it begins to increase rapidly with depth (Jochens et al., 1998). A 1-2 m vertical uplift of isopycnals at this depth could result in a ~ 10 - 20% increase in local nitrate concentration and a commensurate increase in phytoplankton growth rates. The persistence of the isopycnal deflections to a distance of at least 50 km downstream (cf. Fig. 2.10a) implies a temporal persistence on the order of about 7 days, for steady inflow at 8 cm s^{-1} . The response times of phytoplankton are typically on the order of 1 to 2 days, so it is reasonable to expect that they could respond to such an influx of nutrients. Response times of zooplankton and organisms higher up in

the food web tend to be longer; hence, their ability to take advantage of any enhanced phytoplankton production may be compromised.

The enhancement of turbulent mixing rates near the tops of the banks and in their wakes, as represented by increases in the local vertical eddy diffusivity, agrees with several recent studies of turbulence enhancement associated with small-scale topographic features on the sea floor (Toole et al., 1997; Lueck and Mudge, 1997; Moum and Nash, 2000; Lavelle et al., 2004). The potential contribution of many such localized intensifications of turbulence can be important for the overall turbulent mixing in the ocean (Lueck and Mudge, 1997). For instance, Moum and Nash (2000) estimated that the local mixing measured over a single 10-km scale bank on the Oregon shelf was equivalent to that occurring over the entire rest of the shelf out to the 100-m isobath. A similar effect might be at work off the coasts of Texas and Louisiana, where the predominantly smooth, muddy shelf is dotted with several dozen hard banks (in addition to the Flower Garden Banks) that rise to within 50-60 m of the surface (Rezak et al., 1985), and that could be sources of locally enhanced turbulence. Parameterization of this topographically induced mixing for use in large-scale models is warranted, but may be difficult because the spatial scales considered here are much too small to be resolved by global ocean and climate models. Temporal intermittency of enhanced mixing caused by abrupt topography may make the parameterization problem even more of a challenge (Nash and Moum, 2001).

On a local scale, the large turbulent diffusivities produced in the model should influence biological processes via enhanced vertical mixing of nutrients, which exerts a bottom-up control on the nutrient-phytoplankton-zooplankton system. Turbulence can also have top-down effects on planktonic food webs, by influencing zooplankton depth distributions, encounter rates, feeding efficiencies and prey choices (Visser and Stips, 2002).

Although the mean flow along the shelf break near the Flower Garden Banks is toward the east, periods of flow reversal are relatively common and can be sustained for several days at a time (DiMarco et al., 1997). The reversed inflow simulation reveals a

flow structure and wake properties generally very similar to those of the reference eastward inflow case. The only notable differences were the sizes of the near-wake regions, which are somewhat larger for the reversed flow case; the off-shore volume transport between the banks, which is smaller for reversed inflow; and the relative reduction in vortex shedding frequency behind the downstream bank, which is more pronounced for reversed inflow. Retention of particles or accumulation of biomass would appear to be more strongly favored for the westward flow case, since the return-flow wake regions are larger. The longer vortex-formation time associated with the downstream bank could further enhance its retention/accumulation capacity.

The superposition of diurnal variability onto the mean inflow resulted in more pronounced cross-shelf meanderings of streamlines, especially during the deceleration phase of the inflow cycle, than observed for steady inflow. The near- and far-field wakes are wider and the overall cross-shelf flow disturbances greater when forcing was unsteady. Cross-shelf dispersal of particles should be similarly enhanced relative to the steady-inflow case. The cycle of wake formation and destruction associated with deceleration and acceleration of the inflow further compounds the already unsteady nature of flow in the wake. Timing becomes even more critical. For larvae being released from one of the banks, for instance, the state of the near-wake at the time of release may determine whether they are initially retained near their points of origin or very quickly swept away.

Stratification has an important effect on flow patterns. For the stronger (summer) stratification case, a two-layer flow develops, with virtually no surface manifestation of the presence of the topographic banks. Vortices shed from the banks distort near the bank tops and do not penetrate to levels above this. Bograd et al. (1997) used data from satellite-tracked drifters to show that such two-layer flows exist in the ocean. A drifter they released at depth near a group of seamounts in the Pacific ocean remained trapped in a lee-side eddy for several days, while another they released near the surface passed quickly over the seamounts with very little deflection of its path.

Two-layer flow does not exist in the presence of weaker (winter) stratification.

Instead, vortices shed from the banks extend up to the surface and show none of the distortion observed for the summer stratification case. These dramatically different results have important consequences for larval dynamics. At the Flower Garden Banks, the reef-building corals that comprise the foundation of the ecosystem reproduce in one of two ways: mass-spawning corals release positively buoyant propagules into the water column just a few times each year, usually in late summer (Hagman et al., 1998); brooding corals release neutrally buoyant larvae into the surrounding water on a relatively regular basis year-round (Fadlallah, 1983). Larvae of mass-spawning corals, released at the time of near-maximum water column stratification in late summer, apparently have little chance of being retained near their points of origin. Their initial positive buoyancy brings them to the surface, where the effects of the topography below them are not felt because of the two-layer flow, and where their trajectories will be most strongly determined by wind and tidal forcing. Neutrally buoyant brooded larvae have a much better chance of being retained near their natal reefs, since they do not rise to the surface and may thus be temporarily trapped in return-flow wake regions.

Although I compared different strengths of stratification only for steady-inflow forcing, it has been shown that the influence of stratification on the flow field near abrupt topography can be much more pronounced when forcing is periodic rather than steady (Mohn and Beckman, 2002).

The use of more realistic bathymetry resulted in the suppression of the regular vortex shedding that was observed for all of the Gaussian geometry simulations. For the upstream (west) bank, shedding occurs sporadically at depths shallower than about 50 m, where the bank cross-section is very narrow and nearly aligned with the inflow. Deeper than 50 m, flow was disrupted by the neighboring feature on the upstream side of the bank and coherent vortex formation did not occur. The downstream (east) bank presents a flatter, less streamlined cross-section to the incoming flow, which results in a large region of return flow in the wake and only occasional vortex generation and shedding. The cross-sectional areas of the banks are important determinants of the resultant flow character, and of the size and shape of the wakes, which agrees with the model of Coutis

and Middleton (2002), who studied flow past an island using various coastline configurations. They found significant differences in the particle-retention capabilities of different wakes, which depended on the shape of the island under study. I would certainly expect wake-related differences as well, with stronger particle-retention properties for the larger east-bank wake than for the much smaller west-bank wake.

The flow downstream of both banks in the realistic simulations had a significant cross-shelf component, as streamlines there tend to follow bathymetric contours, sweeping flow up onto the shelf. This onshelf flow may have important consequences for colonization of offshore oil and gas platforms by larvae released from the Flower Garden Banks, as well as for overall cross-shelf dispersal of particles.

2.8 Conclusions

For flow over multiple topographic features on a continental shelf, variations in inflow velocity (Ro), strength of stratification (Bu) and topographic detail play key roles in determining the characteristics of the flow-topography interactions. Changes in Ro impact vortex shedding frequencies, wake sizes, wake return flows, cross-shelf transport, isopycnal displacements, relative vorticity generation and turbulent mixing rates. The main consequence of increased water-column stratification is the creation of two-layer flow in which the effects of the submerged topography are manifested only in the deeper layer and not near the surface. Realistic topography creates much more complexity in the observed flow patterns, with suppression of regular vortex shedding and more vigorous cross-shelf activity throughout the model domain.

The results of this chapter set the foundation for further studies on flow-topography interactions and their impacts on biological processes at the Flower Garden Banks. Many of the speculations and predictions made in the above discussion will be tested using a Lagrangian particle-tracking routine coupled to the flow model (for larval transport, chapter III) and an embedded nutrient-plankton ecosystem model (for plankton dynamics, chapter IV).

CHAPTER III

PARTICLE TRANSPORT AND IMPLICATIONS FOR LARVAL DYNAMICS

3.1 Overview

For the many marine organisms that reproduce by releasing larvae into the water column, dispersal processes experienced by those larvae can play a key role in recruitment dynamics and hence population structure and ecosystem function. The impracticality of measuring larval transport in the field has prompted the development and use of numerical models to study larval processes. Here, a Lagrangian particle-tracking algorithm embedded in a three-dimensional hydrodynamic model was used to compute the trajectories of passive particles in topographically influenced oceanic flows. The modeled ecosystem is based on the Flower Garden Banks, two small and geographically isolated but thriving coral reefs in the northwest Gulf of Mexico. Variations in inflow velocity, strength of stratification and degree of topographic detail influence modeled patterns in particle retention, dispersal and interbank transport. Faster inflows, although they are associated with larger wake regions immediately downstream of the banks and stronger return flows within the wakes, nevertheless result in reduced retention of particles originating from the bank tops. The timing and magnitude of interbank particle transport and of downstream dispersal are also controlled by the speed of the inflow. A strongly stratified water column results in a two-layer flow environment where flow in the surface layers is effectively cut off from the influence of the submerged banks and particles released in the surface layers are minimally perturbed. Weaker stratification leads to a notable surface signature of the subsurface flow disturbance and to enhanced dispersal of surface-layer-released particles. Incorporation of more realistic bathymetry changes the fundamental nature of the flow field, which alters the pattern in downstream particle dispersal and has implications for transport of larvae to nearby oil and gas platforms in the Gulf of Mexico.

3.2 Introduction

One of the most fundamental yet least understood aspects of coral reef ecosystem dynamics, and indeed of marine ecosystem function in general, is larval dispersal and transport. Many reef-associated organisms, including the corals themselves, reproduce sexually by releasing gametes or early larvae into the water column, where fertilization and/or further development take place. The growing larvae are at the mercy of the prevailing currents while they develop sufficiently to settle in or recruit to a chosen environment. Establishment of new coral colonies and recruitment of other reef-associated organisms thus depends at least partly upon the availability of settlement-ready larvae in the water column near appropriate sites. Efforts to predict this availability depend upon knowledge of both the physical environment and larval ecology.

The very existence of a pelagic larval phase in so many reef organisms and the presence of coral reefs in geographically isolated regions of the world's oceans suggest that long-distance transport of larvae is an important mechanism for the establishment of new communities and the maintenance of existing ones. Recent evidence has shown, however, that many coral reef ecosystems may, in fact, depend heavily on local sources of larvae to sustain their populations (Todd, 1998; Jones et al., 1999; Swearer et al., 1999; Cowen et al., 2000). Understanding the relative importance of local vs. remote sources of larvae and uncovering the specific physical and biological mechanisms underlying both possibilities has direct implications for population dynamics studies, fisheries management and marine reserve design (Cowen et al., 2000; Warner et al., 2000). Yet these mechanisms are inherently difficult to determine experimentally (Levin, 1990). The use of numerical models is an alternative and potentially very powerful way to explore these questions.

Most previous studies of hydrodynamics and larval transport in coral reef ecosystems have focused on Australia's Great Barrier Reef (GBR). Williams et al. (1984) were among the first to integrate knowledge of the large-scale flow patterns over the central region of the GBR with information on larval pelagic duration. They inferred that most

larvae released in the region were likely to be swept into the shelf current and transported far downstream before settling.

Direct measurements of larval settlement at a relatively isolated reef in the GBR showed that, notwithstanding long-distance transport, recruitment of corals from local sources was occurring in significant numbers (Sammarco and Andrews, 1988). In addition, observed spatial patterns in settlement density around the reef showed some correspondence with modeled water residence times, with settlement occurring mostly in regions having the lowest flushing rates. A similar study by Wolanski et al. (1989) combined measurements of the flow field around Bowden reef in the GBR with observations of coral egg aggregations on the sea surface and of drifter tracks to show that both local retention and long-distance transport of larvae were possible, and that the ultimate fate of larvae depended strongly on the prevailing currents at the time of spawning.

Combined hydrodynamic and particle tracking numerical models designed to study larval transport and dispersal on the GBR (e.g. Dight et al., 1990; Black, 1993) have proven useful in terms of understanding the initiation and spread of crown-of-thorns starfish outbreaks, though the two dimensional nature of most of these studies was recognized as one of their primary limitations (Oliver et al., 1992). Preliminary three-dimensional modeling in this area (Black et al., 1991) uncovered order-of-magnitude differences in particle retention depending on the particles' vertical positions in the water column.

While most of the reef crests of the GBR are very near the sea surface, those of the Flower Garden Banks, the study area of interest here, are submerged beneath ~20 m of seawater. This makes the topography of the Banks in many ways analogous to that of open ocean seamounts, though the spatial scale is significantly smaller.

The Flower Garden Banks region, a National Marine Sanctuary, was chosen as a model system in this study because the complex topography is known to exert significant influence on the flow field surrounding it and this flow disruption is thought to have important consequences for particles that are released from the banks. I explore the

retention of particles near their points of release, potential exchange between the two banks, and longer-distance transport to alternative settlement sites such as the many oil and gas platforms that dot the surrounding continental shelf and slope area. The goal is to uncover some of the physical mechanisms that might influence larval dispersal in this region and to characterize the patterns in transport and dispersal that result. The spatial and temporal scale of this study fits in between (and can complement) transport studies based on larger-scale (e.g. Gulf-wide) circulation patterns that may be inferred from satellite altimetry or coarser resolution ocean models (e.g. Cowen et al., 2000; Polovina et al., 1999; Lugo-Fernandez et al., 2001) and the very small-scale studies that focus on the details of the actual larval settlement process, including surface composition and roughness, chemical cues, boundary-layer fluid dynamics and larval behavior (e.g. Crimaldi et al., 2002; Browne and Zimmer, 2001; Butman et al., 1988).

Exploration of flow patterns and larval transport at the Flower Garden Banks has thus far been limited to a study by Lugo-Fernandez et al. (2001). In it, the authors used observed and simulated drifter tracks to identify several modes of large-scale transport that are likely to affect dispersal of larvae from the Banks. The present study is designed to examine in much closer detail the mechanisms of flow disruption in the close vicinity of the banks and how that disruption influences the transport of passive particles. I use a high spatial resolution hydrodynamic model coupled to a Lagrangian particle tracking algorithm to simulate detailed particle trajectories and dispersal patterns, which are important to determining the ultimate fates of particles on time scales relevant to the pelagic larval duration of coral (and other marine) larvae.

3.3 The Flower Garden Banks

The Flower Garden Banks are located on the continental shelf of the northwestern Gulf of Mexico, approximately 200 km south of the Texas-Louisiana border, near the shelf break (Fig. 3.1). They rise from depths of 100–150 m to approximately 20 m, where temperature and light penetration are sufficient to sustain thriving coral reef ecosystems. The average surface-layer current velocity is 8 cm s^{-1} , directed eastward, but variability in both speed and direction is large (DiMarco et al., 1997). Near-surface

flow at the banks is predominantly wind-driven, as it is over most of the continental shelf (Cochrane and Kelly, 1986; Cho et al., 1998). Tidal ellipses are oriented with their major axes across bathymetric contours (i.e. in the cross-shelf direction) and tidal currents range from $\sim 3\text{-}6\text{ cm s}^{-1}$ (DiMarco and Reid, 1998). Their positions near the shelf break also subjects the banks to the influences of deep-water processes, most importantly the large, anticyclonic eddies that separate from the Loop Current in the eastern Gulf of Mexico. These eddies travel westward through the Gulf, eventually impacting the slope where they are partly responsible for the eastward flow near the shelf-break and can cause significant cross-shore transport (Brooks, 1984; Oey, 1995; Sahl et al., 1997).

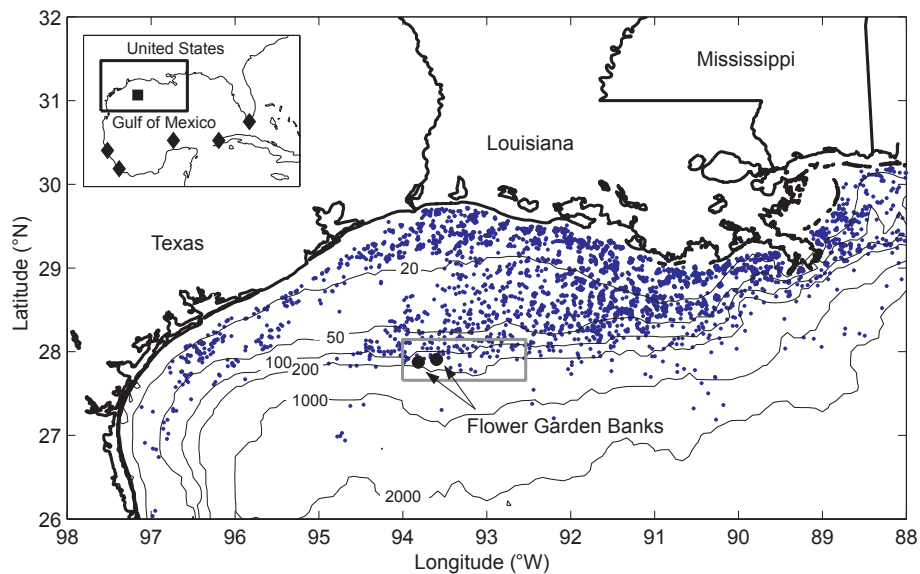


Fig. 3.1. Map of Flower Garden Banks. Gray box shows region modeled. Blue dots are locations of offshore oil and gas platforms. Filled square in inset box shows location of Flower Garden Banks. Diamonds in inset box show locations of nearest coral reefs. Depth contours in meters.

The banks are separated by about 20 km and together they are more than 600 km from their nearest neighboring coral reefs around Veracruz, Mexico, on the Yucatan Peninsula and in the Florida Keys. They were presumably first colonized by larvae from these remote sources, but it is not known whether and to what extent they continue to be

dependent on remote sources of larvae. The banks are thought to act as sources of larvae to themselves, to one another and to the many surrounding offshore oil and gas platforms on the continental shelf and slope (Fig. 3.1).

The two methods of sexual reproduction in reef-building corals are broadcast spawning and brooding. Most broadcast-spawning species release gametes or gamete bundles into the water column, where fertilization and early embryonic and larval development occur (Fadlallah, 1983). The gamete bundles and early-stage larvae of spawners are usually positively buoyant upon release and for some time thereafter (Kojis and Quinn, 1982; Bull, 1986; Wyers et al., 1991). After fertilization occurs, larvae must go through a stage (the pre-competent stage) that involves growth and development but during which settlement is impossible. Once they have developed sufficiently to be able to settle, they are in the competent stage but remain in the plankton until they find a suitable benthic habitat. Most spawned larvae have pre-competent periods of one to two weeks (Harrison et al., 1984; Babcock and Heyward, 1986). The duration of the competent period is typically on the order of several weeks, although maximum competency periods of up to three months have been measured in the lab (Harrison et al., 1984; Wilson and Harrison, 1998).

Brooding species incubate larvae internally to a more advanced stage of development before releasing them into the water column. Most brooded larvae are neutrally buoyant and competent to settle immediately or within hours of release, though many are able to survive without settling for several days to a week (Lewis, 1974; Goreau et al., 1981). Maximum measured competency periods for brooded larvae are on the order of one month (Fadlallah, 1983).

Once larvae have been released, they become part of the plankton and are primarily at the mercy of prevailing currents for transport and dispersal (Scheltema, 1986). They can change only their vertical positions in the water column separately from the velocity field around them, either indirectly through developmental changes in buoyancy and sinking rates (Bull, 1986), or directly through active swimming (Chia et al., 1984).

At the Flower Garden Banks, about 90% of the corals are broadcast spawners. Seven of the approximately twenty species that are present at the Banks are known to participate in annual mass spawning events, which occur in late summer and can be predicted from a knowledge of lunar phase and sea surface temperature (Gittings et al., 1992; Hagman et al., 1998). Brooding species tend to reproduce several times throughout the year (Szmant, 1986) but reproductive behavior in brooders at the Flower Garden Banks has not been observed. Settlement of brooded larvae has been documented at the Banks (Baggett, 1985), while that of broadcast-spawned larvae has not.

3.4 Model Description and Configuration

I used the Regional Ocean Modeling System (ROMS), described in detail by Haidvogel et al. (2000) and Marchesiello et al. (2003), to model the flow field in the region of interest. ROMS is a free-surface hydrostatic model that solves the primitive equations of motion using finite-difference approximations on orthogonal coordinates in the horizontal and a stretched, terrain-following coordinate in the vertical.

3.4.1 Model domain and grid

The geographic region of interest extended from ~ 92.5 to 94° W longitude and from ~ 27.7 to 28.1° N latitude, forming a domain ~ 140 km in the alongshelf (zonal) direction and ~ 50 km in the cross-shelf (meridional) direction. The horizontal grid consisted of 205 cells in the alongshelf direction and 125 cells in the cross-shelf direction. In both the alongshelf and cross-shelf directions, horizontal grid resolution varied smoothly and gradually from 200 m over a region centered on the banks to 2000 m near each boundary of the domain. The maximum relative change in grid cell length between any two adjacent cells was less than 5%. There were forty vertical levels, with resulting vertical grid resolutions of ~ 0.5 m above the banks, where the minimum depth was ~ 20 m, and ~ 3 to 11 m in regions of maximum depth. The Coriolis parameter was set to a constant value of $6.8 \times 10^{-5} \text{ s}^{-1}$, which corresponds to 27.9° N latitude; beta-plane effects were neglected.

I tested both highly idealized and somewhat more realistic bathymetries in the model. The idealized topography consisted of two Gaussian peaks, representing the East and West Flower Garden Banks, on a smooth shelf-slope region (Fig. 3.2a). The more realistic bathymetry was created by combining two data sets: that of Gardner et al. (1998), with a horizontal resolution less than 10 m, for the banks themselves, and that of Herring (Dynalysis of Princeton, unpublished data), with a ~ 1 -km resolution, for the surrounding shelf and slope regions (Fig. 3.2b). Depth values at grid points were

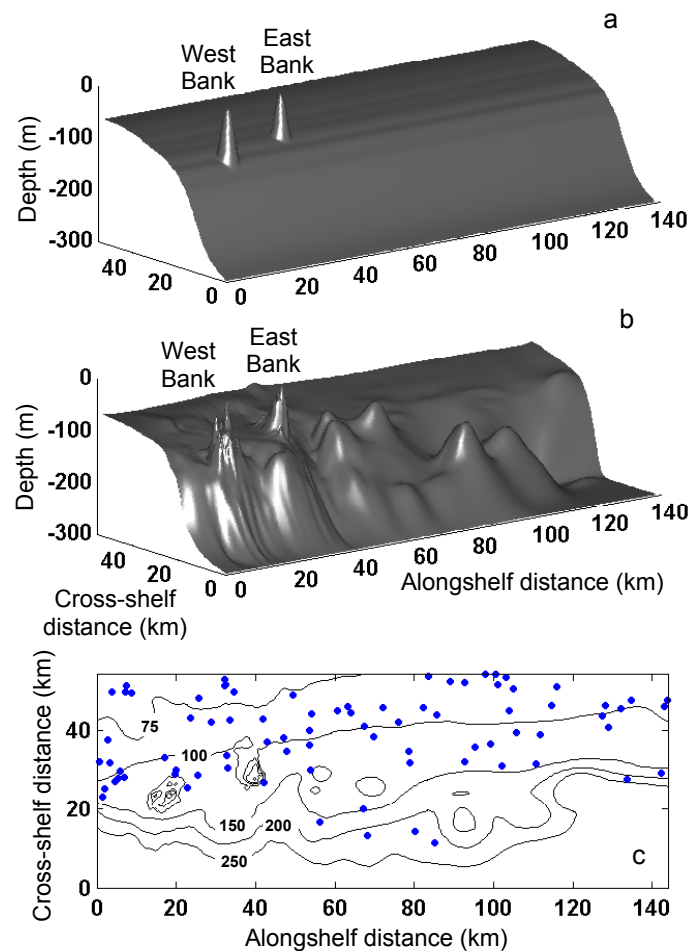


Fig. 3.2. Model bathymetries and platform locations. (a) Ideal case with Gaussian peaks. (b) More realistic case. (c) Contour map of more realistic topography. Blue dots show locations of oil and gas platforms. Depth contours in meters.

calculated by bilinear interpolation of the combined data sets. The topographically complex slope region was greatly simplified by imposing a maximum depth of 300 m offshore. The resulting bathymetry was then smoothed using a selective Shapiro filter such that the maximum relative variation in topography computed on the discrete grid was less than 0.15, a constraint that is thought to minimize potential pressure-gradient errors (Beckman and Haidvogel, 1993).

The density-Jacobian scheme of Shchepetkin and McWilliams (2003) was used to compute the pressure gradient terms. Diagnostic simulations were conducted without forcing and with closed-wall boundary conditions; the resulting spurious velocities generated by pressure gradient errors were negligibly small.

3.4.2 Initialization, forcing and boundary conditions

Initial water column stratification was set by choosing a typical potential temperature vertical profile from data gathered near the Flower Garden Banks during the LATEX program (Jochens et al., 1998). One of two profiles was used to initialize the entire domain. Most of the simulations used a temperature profile derived from a summer 1992 cruise when surface temperature was 29°C and there was a strong thermocline centered at 35 m. A temperature profile more typical of winter conditions, based on data from a February 1994 cruise, was used for comparison in one simulation. The winter profile had a surface temperature of about 21°C and a relatively weak thermocline at 100 m.

Salinity varies moderately with depth near the Flower Garden Banks on a seasonal basis. Most of the variability is in the upper 10-20 m. Annual surface salinity near the Flower Garden Banks averages 35.5 (30.4-37.4) psu, while near-bottom salinity averages 36.3 (35.6-36.8) psu (Jochens et al., 1998). For simplicity, its value was fixed at a uniform 36 psu in the model. Seawater density was computed in the model using the UNESCO equation of state.

Each simulation started with the water at rest throughout the domain; currents were induced by specifying a uniform barotropic velocity at the upcurrent boundary. The velocity was increased from zero to the target value over a period of three days using a

hyperbolic tangent multiplier. Variations in the imposed forcing form an integral part of the overall strategy employed and are discussed in section 3.5.

The onshore and offshore boundaries of the domain were closed, while the upcurrent and downcurrent boundaries were open and subject to radiation of mass and momentum. I implemented the oblique radiation and adaptive nudging technique described by Marchesiello et al. (2001) at the open boundaries. Where information fluxes were directed into the domain, I nudged boundary temperatures to their specified initial values and barotropic velocities to the imposed forcing value, both on a time scale of four hours (strong nudging). Where fluxes were directed out of the domain, I allowed barotropic velocity and temperature to relax to the desired background values on a time scale of 14 days (weak nudging). A sponge layer provided damping over 5 grid points (about 10 km) on the downcurrent end of the domain; Laplacian horizontal mixing coefficients for momentum and tracers increased quadratically in this region from zero in the interior to $100 \text{ m}^2 \text{ s}^{-1}$ at the boundary.

3.4.3 Particle tracking

Each simulation was integrated without particles for 14 days so that the flow fields were well-developed by the time the particle tracking routine began (i.e. the total kinetic energy in the domain had reached an approximately constant value). A total of ten thousand particles were released during each simulation. Particles were released in batches of 2000 (1000 at each bank) at six-hour intervals over the span of a single day. Initial particle positions were randomly distributed at depths shallower than 40 m over the tops of the banks (i.e. at the lowest vertical model level). Particles were tracked for 7 to 28 days after being released, depending on inflow speed; their positions were saved to memory every four hours. Tracking stopped if a particle left the model domain. Particle trajectories were computed using the fourth-order predictor-corrector time-stepping scheme that is included as part of ROMS.

3.4.4 Oil and gas platforms

The locations of nearby oil and gas platforms (Fig. 3.2c) were obtained from a downloadable database maintained by the Minerals Management Service

(www.mms.gov). Although these platforms are known to influence the flow field surrounding them, their effects are generally small and highly localized (Forristall, 1996). They were not included in the hydrodynamic model.

3.5. Strategy

The reference simulation consisted of an 8 cm s^{-1} eastward flow over the idealized topography grid with summertime stratification. Additional simulations were conducted using steady eastward velocities of 4 and 16 cm s^{-1} ; reversing the flow direction; using the winter stratification; and using the more realistic bathymetry. Two final simulations incorporated diurnal sinusoidal velocity forcing on the ideal and realistic topographies. Table 3.1 summarizes the conditions for each of the simulations conducted.

Table 3.1. Parameters of the particle-transport simulations. Details of geometries and stratifications are as described in the text. Inflow speed is positive eastward, negative westward. ω is equal to the forcing frequency, $2\pi/D \text{ d}^{-1}$ where D is 1 day and t is measured in days. Simulation B is the reference simulation.

Simulation	Geometry	Inflow speed (cm s^{-1})	Stratification
A	Ideal	4	Summer
B	Ideal	8	Summer
C	Ideal	16	Summer
D	Ideal	-8	Summer
E	Ideal	$8 + 4\sin(\omega t)$	Summer
F	Ideal	8	Winter
G	Realistic	8	Summer
H	Realistic	$8 + 4\sin(\omega t)$	Summer

3.6. Results

3.6.1 General features of the flow

Flow over and around the Gaussian peaks is characterized by vigorous vortex shedding and by strong return flows immediately downstream of each peak. Streamlines are deflected around the peaks and continue to undulate through the downstream region of vortex shedding (Fig. 3.3a). Normalized velocity anomaly vectors show that the shed vortices have characteristic sizes that initially scale with the cross-sectional areas of the peaks and that they tend to coalesce downstream of both banks to form larger vortical

structures in the flow (Fig. 3.3a). The normalized velocity anomaly is computed by subtracting the forcing velocity (U) from the alongshelf velocity component (u), and then normalizing both the alongshelf and cross-shelf velocity (v) components by the forcing velocity (i.e. $u^* = (u - U)/U$ and $v^* = v/U$). The frequency of vortex shedding increases with inflow velocity, ranging from $\sim 0.25 \text{ d}^{-1}$ for 4 cm s^{-1} inflow to $\sim 0.8 \text{ d}^{-1}$ for 16 cm s^{-1} inflow.

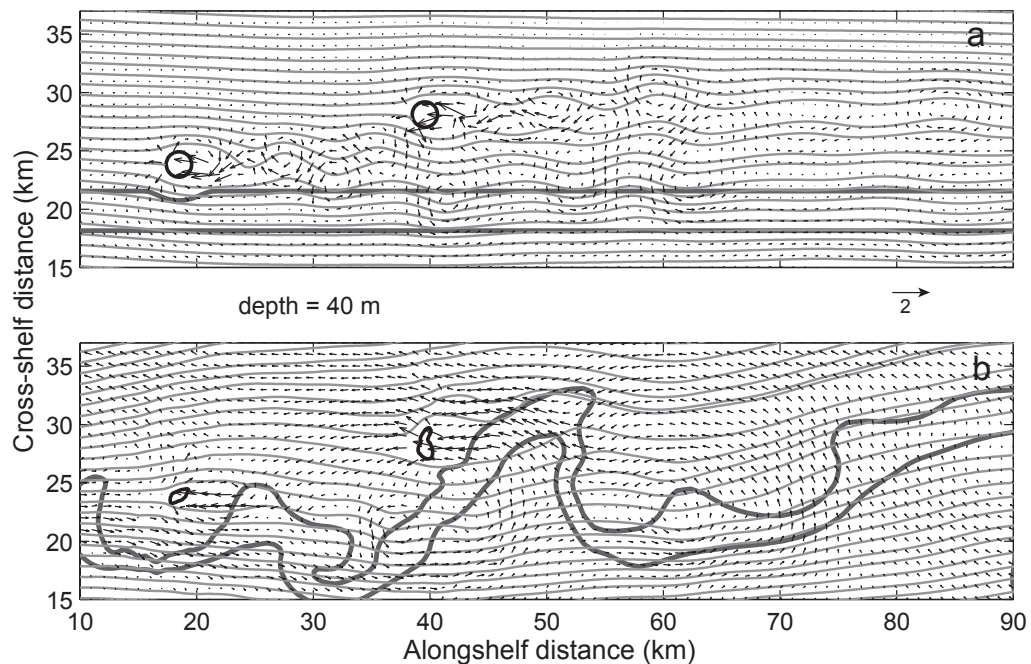


Fig. 3.3. Comparison of flow patterns. Snapshots of streamlines and normalized velocity anomaly vectors at 40-m depth. (a) Reference simulation B, Gaussian bathymetry. (b) Simulation G, more realistic bathymetry. Closed black contours are at 40 m. Thick gray lines are the 125 and 150 m isobaths. Normalized velocity anomaly is computed by subtracting the alongshelf forcing velocity from the model velocity and dividing by the forcing velocity (see text). Only part of the model domain is shown.

Regular vortex shedding is suppressed for the more realistic bathymetry case, although the return-flow wake regions persist. Streamline deflection is minimal for flow around the west (upstream) bank, where the bank cross-section is more streamlined than

for the case of Gaussian peaks, but is more pronounced for flow around the east (downstream) bank, since the bank cross-section there presents more of a bluff body shape to the oncoming flow (Fig. 3.3b). Streamlines between the two banks are directed more strongly off-shelf for the realistic bathymetry case; downstream of both banks the streamlines tend to follow the bathymetric contours of the narrowing shelf-slope.

The wake regions immediately behind each of the banks where flow is directed back toward the banks are generally narrow bands that extend 2-3 km downstream (Fig. 3.4). For the ideal bathymetry cases, the average volume of the return-flow region increases with inflow velocity. For the west bank, the return-flow wake volume is approximately equal for the ideal and more realistic bathymetries (Fig. 3.4, left panels), whereas for the east bank, the wake region is somewhat larger for the realistic bathymetry case (Fig. 3.4, right panels). The background alongshelf velocity also tends to be slower for flow past the more realistic east bank as compared to the Gaussian east bank.

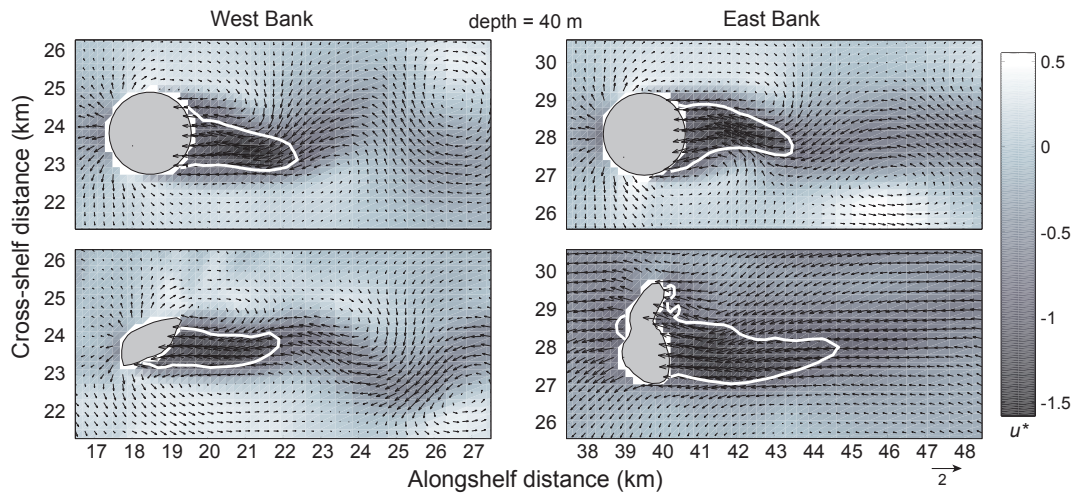


Fig. 3.4. Comparison of wake structures. Normalized instantaneous velocity anomaly vectors at 40 m on day 16. Shading denotes the magnitude of the alongshelf component of normalized velocity anomaly. White contours are where $u^* = 0$. Upper panels are reference simulation B (Gaussian bathymetry), lower panels are simulation G (more realistic bathymetry).

When the inflow forcing is reversed (simulation D), the sizes of the return-flow wake regions tend to be larger than for the reference case. This is due to early separation of the flow around the Gaussian peaks, a result of topographically induced changes in the relative vorticity of the flow (see Chapter II). Deflection of flow in the gap between the two peaks is also less pronounced for the reversed flow case, which will be shown to have consequences for interbank transport of particles.

Unsteady forcing (simulations E and H) leads to dynamic cycles of wake formation, growth and obliteration, accompanied by broader cross-shelf excursions of the flow field than for the steady forcing cases. The primary impact of a less stratified water column (simulation F) is to allow the flow disturbances created by the presence of the banks to be manifested in the surface layers, above the tops of the banks, instead of being confined to the deeper layers, as is the case for the summer stratification simulations. Cross-shelf excursions of the flow field are also more pronounced for the weaker stratification simulation.

3.6.2 Particle retention

The presence of the banks results in enhanced retention of particles near their release points in all cases (Fig. 3.5). For the varying inflow velocity cases (simulations A-C), the time to loss of 50% of the particles is 2-3 times longer when the banks are present than when they are not (Fig. 3.5a). Retention is greatest for the slowest inflow case. At two days, which corresponds approximately to the minimum pre-competency period for spawning corals, ~40% of the particles remain within 2 km of their release points for the 4 cm s^{-1} case; ~10% remain for the 8 cm s^{-1} case; and ~3% remain when the inflow is 16 cm s^{-1} . After one week, which is a more typical spawner pre-competency period, ~7% of particles remain within 2 km for the 4 cm s^{-1} case, whereas only ~0.05 to 0.15% remain for the faster inflow cases. Even these very small percentages, however, can mean significant numbers of particles retained when the numbers initially released are in the tens to hundreds of thousands, or more.

For the unsteady flow case (simulation E), the timing of particle release impacts particle retention, with greater retention of particles that are released when the flow is

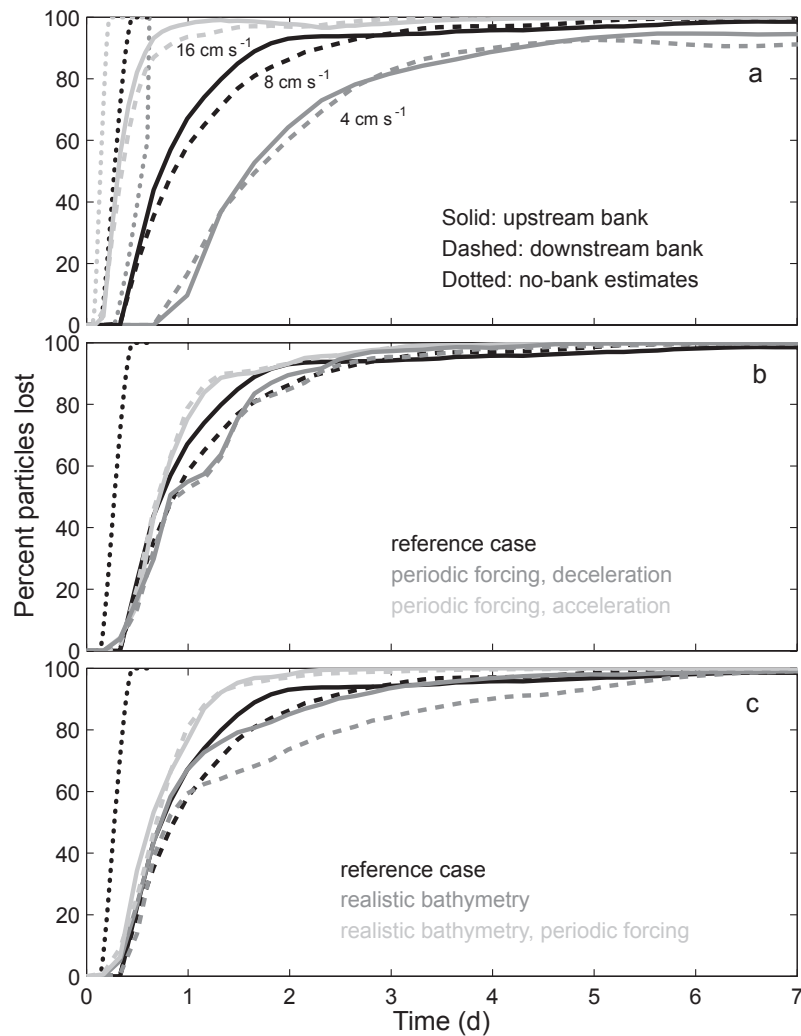


Fig. 3.5. Loss of particles over time. A particle is assumed lost when its distance from the center of the bank from which it was released exceeds 2 km. No-bank estimates are based on advection of particle patches at the mean inflow speed. (a) Simulations A, B and C. (b) Simulations B and E, where a distinction is made between particles released during acceleration of the flow and those released during deceleration. (c) Simulations B, G and H.

decelerating and less retention when particles are released during the acceleration phase (Fig. 3.5b). The difference in retention is only evident between days one and two, but approaches about 30% (55% lost versus 85% lost at 1.2 days). Greater retention coincides with times of large return-flow wake volumes, while less retention occurs when the wakes are washed out of existence by the accelerating flow.

Particle retention is enhanced when the more realistic bathymetry is used in place of the Gaussian peaks along with steady inflow forcing (Fig. 3.5c). The difference in the retentive properties of the upstream and downstream banks is also amplified, with the downstream bank able to trap particles more effectively. However, when unsteady forcing is applied on the more realistic bathymetry, particle retention suffers. The loss rates plotted in Fig. 3.5c include particles released during all phases of the inflow cycle; the net effect of periodic forcing is to reduce retention of particles near their points of release.

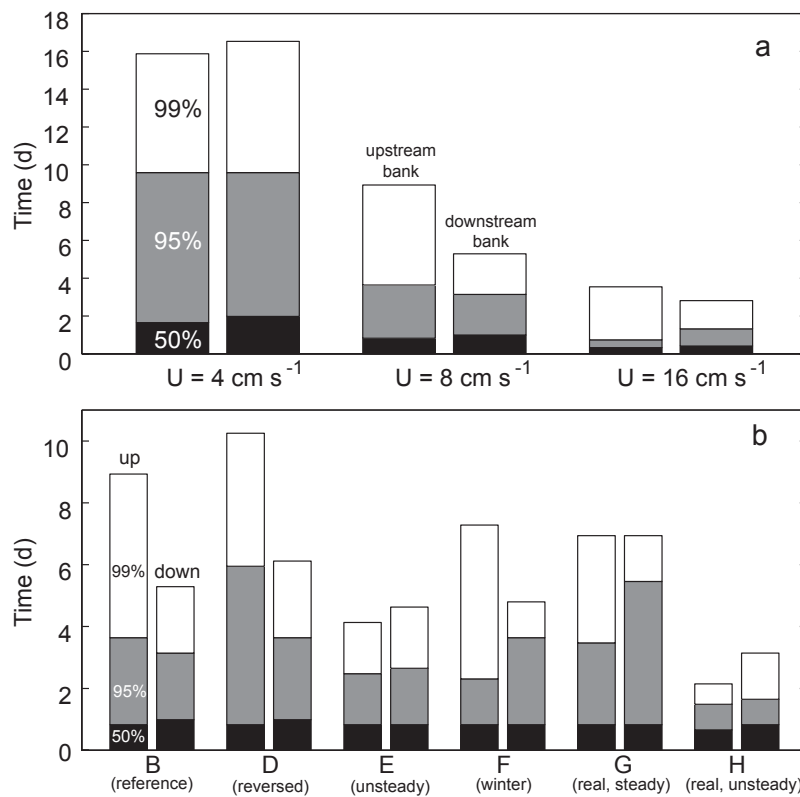


Fig. 3.6. Patterns in particle loss. Bars are color-coded to show times to loss of 50%, 95% and 99% of particles. A particle is considered lost when its distance from the center of the bank from which it was released exceeds 2 km. The left bar of each pair presents results for the upstream bank while the right bar presents results for the downstream bank. (a) Simulations A, B and C. (b) Simulations B and D–H. Note that for simulation D (reversed flow), the upstream and downstream directions are reversed.

The most significant and systematic trend in retention of particles near the banks is attributable to variations in the magnitude of the inflow velocity, with longer retention times corresponding to slower inflows (Fig. 3.6a). Comparison of the simulations for which the mean inflow speed is 8 cm s^{-1} (simulations B and D–H) reveals that in all cases the time to loss of 50% of the particles is about the same, at just under one day (Fig. 3.6b). Differences in retention times are only apparent for the remaining 50% of particles. When the flow is reversed, retention of these remaining particles is greater for both the upstream and downstream banks. When weaker stratification is used, retention tends to be somewhat less for both banks. In both of these cases, the pattern apparent in the reference case of less retention at the downstream bank as compared to the upstream bank persists.

For the more realistic bathymetry, steady inflow simulation, the time to loss of 99% of the particles is approximately 7 days for each of the banks; the effect of the larger cross-sectional area of the downstream (east) bank and resulting larger return-flow wake volume can only be seen in the time to loss of 95% of the particles, which is ~ 5.5 days for the downstream banks and ~ 3.5 days for the upstream bank (Fig. 3.6b). Unsteady forcing results in less particle retention for both the ideal Gaussian and more realistic topographies.

3.6.3 Particle dispersal

Dispersal of particles released from the bank tops is predominantly in the alongshelf direction, an expected consequence of the unidirectional alongshelf inflow forcing. As some particles are initially retained in the near-wake regions behind the banks, others are transported downstream with the mean flow, and the originally cross-sectionally circular particle patches (for the Gaussian cases), elongate into narrow bands (Fig. 3.7, upper panels). Cross-shelf dispersion of particles increases with distance downstream as a result of the horizontal spreading and partial coalescence of vortices shed from the banks. This is best seen in snapshots of particle positions on day 12 and day 16 in the upper panels of Fig. 3.7. Dispersal in the vertical direction is minimal, as the strong stratification of the water column confines the particles to a vertical band 20–25 m thick.

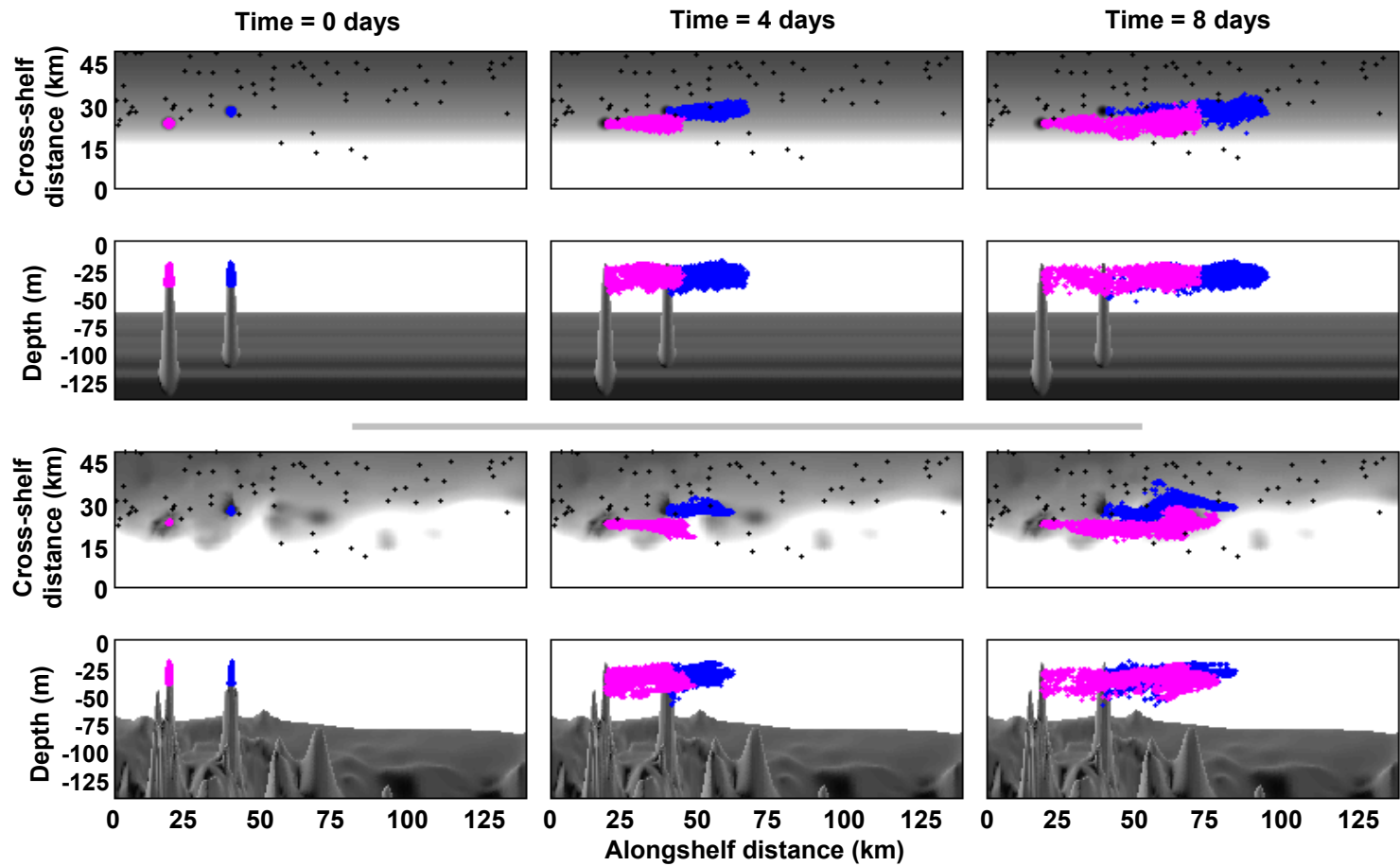


Fig. 3.7. Patterns in particle dispersal. Locations of all 5000 particles released from each bank are plotted at four-day time intervals. Black dots indicate locations of oil and gas platforms. For each time and simulation there is an overhead view and a profile view. Upper panels show the reference case (simulation B), lower panels show the more realistic bathymetry case (simulation G).

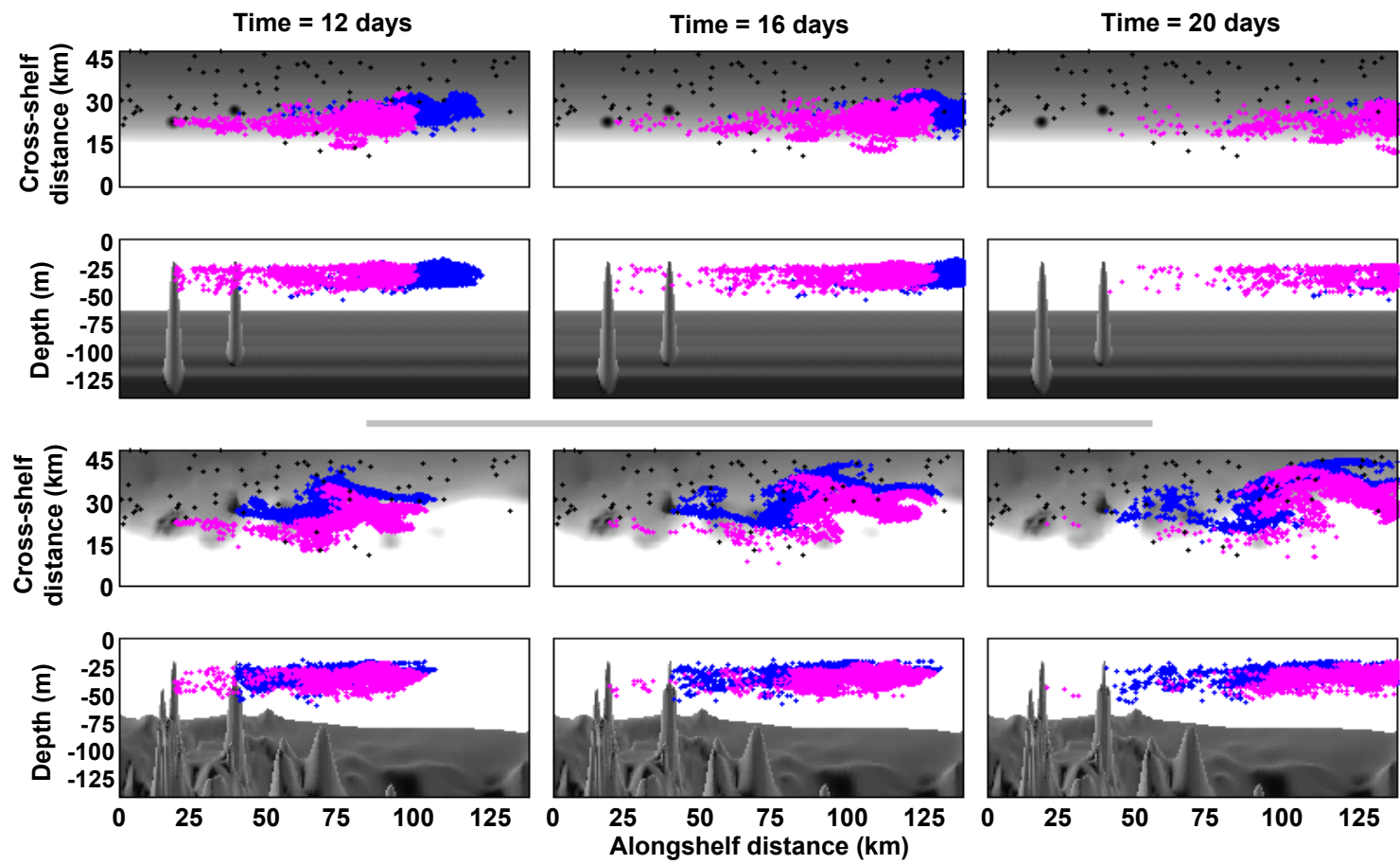


Fig. 3.7. Continued.

Comparison of the domain-wide dispersal patterns for the reference case (Fig. 3.7, upper panels) with the more realistic bathymetry, steady inflow case (Fig. 3.7, lower panels), reveals that cross-shelf dispersion of the particle patches in the realistic case is strongly influenced by the topography of the shelf-slope downstream of both of the banks. The narrowing of the shelf results in the particle patches being steered up onto the shelf as the flow conforms to isobaths. The mean flow on the shelf is slowed in the realistic case, which results in relatively longer residence times of the particle patches there, especially for particles released from the downstream bank (compare positions of blue particles in the upper vs. lower panels at day 16 and day 20).

To quantify the effect of variations in the speed of the steady inflow on particle dispersal, I computed variances in particle positions through time in both the alongshelf and cross-shelf directions. The rate of change of the variance (σ^2) can be interpreted as an effective mixing coefficient for the particle patch (i.e. $K_{eff} = d\sigma^2/2dt$). As expected, the alongshelf variance in particle positions increases most rapidly for the fastest inflow simulation. However, the reduced particle retention in this case results in a maximum patch variance of $\sim 150\text{--}175 \text{ km}^2$ within the model domain whereas the slowest inflow simulation results in a maximum patch variance of $\sim 200\text{--}250 \text{ km}^2$ (Fig. 3.8, upper panels). Effective mixing coefficients initially increase as the patches are stretched in the alongshelf direction, then decrease once most of the particles have escaped from the near-wake regions and the patches are transported downstream as a group. Maximum values of the alongshelf effective mixing coefficients are $\sim 100 \text{ m}^2 \text{ s}^{-1}$ for $U = 4 \text{ cm s}^{-1}$, $\sim 150 \text{ m}^2 \text{ s}^{-1}$ for $U = 8 \text{ cm s}^{-1}$, $\sim 275 \text{ m}^2 \text{ s}^{-1}$ for $U = 16 \text{ cm s}^{-1}$. In all cases, the effective mixing coefficient eventually settles to a value between 10 and $100 \text{ m}^2 \text{ s}^{-1}$.

Variances of particle positions in the cross-shelf direction also increase most rapidly for the fastest inflow case, but here the maximum value of the variance is also largest when inflow is fastest (Fig. 3.8, lower panels). Maximum patch variances are on the order of 10 km^2 , an order of magnitude smaller than alongshelf values. Effective mixing coefficients in the cross-shelf direction are negative just after particles are released, which is not physically meaningful but is a result of particles released from the on-shelf

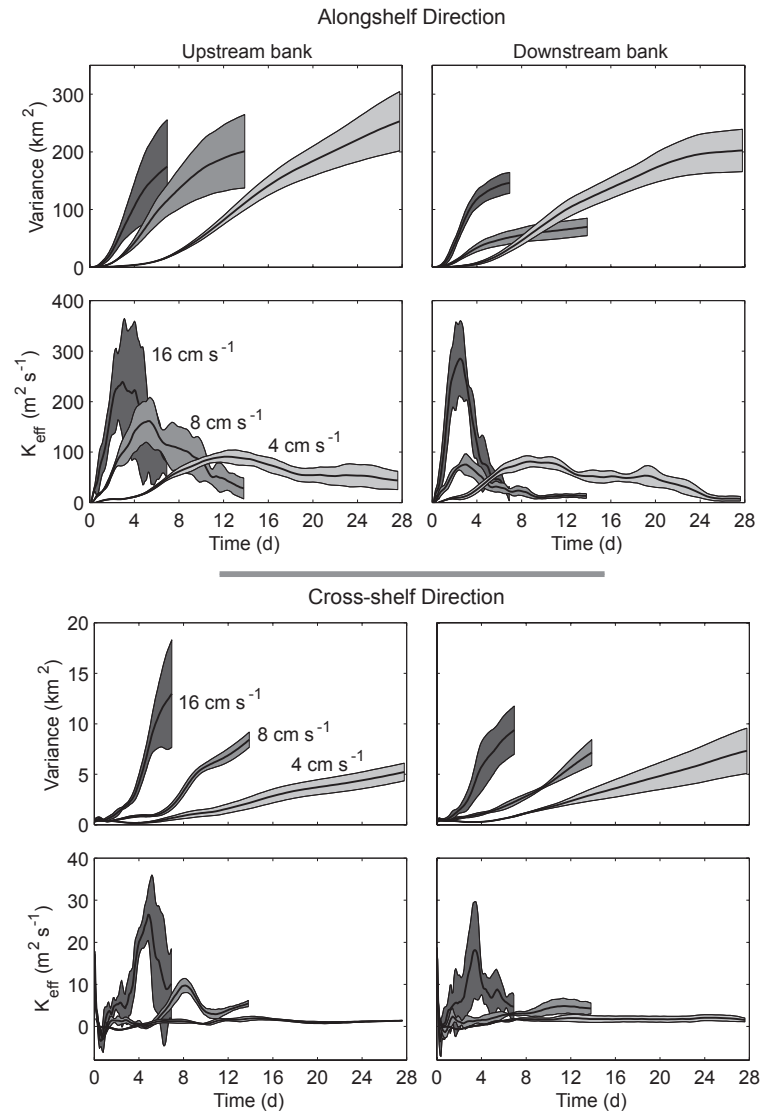


Fig. 3.8. Variances in particle positions and effective mixing coefficients. Simulations A–C (idealized geometry). Mixing coefficients calculated using $K_{eff} = \Delta\sigma^2/2\Delta t$, where σ^2 is the variance. Shaded regions denote ± 1 standard deviation about the mean of five releases of 1000 particles each.

and off-shelf flanks of the banks being swept into the central wake regions. Values of effective cross-shelf mixing coefficient are also an order of magnitude smaller than their alongshelf counterparts, at $\sim 1\text{--}10\text{ m}^2\text{ s}^{-1}$. Taken together, the patterns in alongshelf and cross-shelf particle patch variances and effective mixing coefficients depicted in Fig. 3.8

point to slower inflow speeds resulting in longer and narrower bands of dispersed particles while faster inflows lead to somewhat shorter and wider bands. The characteristic time associated with the particle dispersal process scales inversely with inflow speed.

The fundamental difference in flow structure between the reference simulation (B), with strong summer stratification, and the weaker winter stratification simulation (F) is that strong stratification isolates the flow in the upper water column from the disturbance caused by the presence of the banks in lower layers. The influence of this one-layer vs. two-layer flow on dispersal of particles was tested by releasing additional batches of neutral particles in simulations B and F, initially distributed in columns over the depth range 5–15 m above the tops of the two banks. The enhancement of particle dispersal for the winter stratification case is dramatic, with patch sizes after 14 days on the order of ten times larger than those of the summer stratification case (Fig. 3.9).

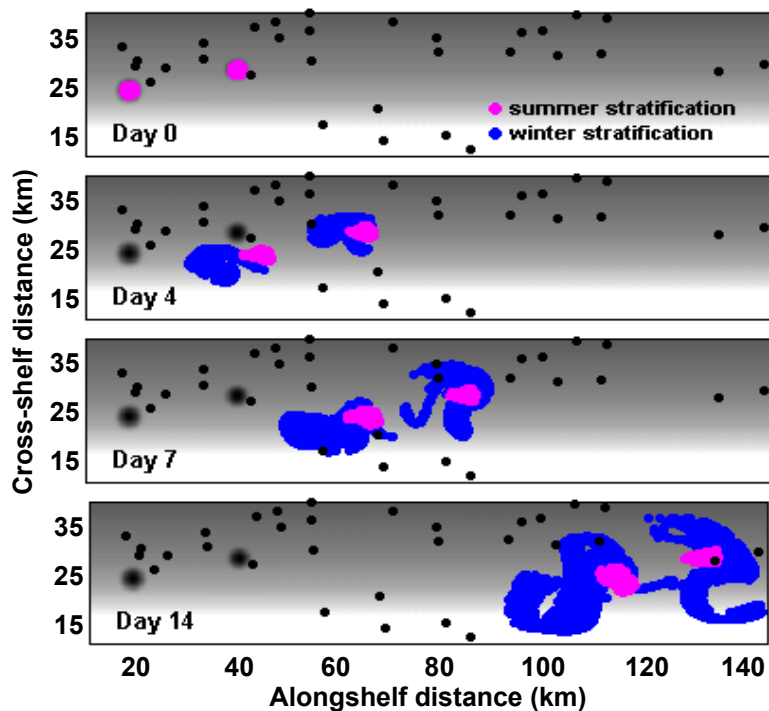


Fig. 3.9. Dispersal of near-surface released particles. Simulations B (pink) and F (blue). 5000 particles were released atop each bank. Black dots show platform locations.

The broader cross-shelf distribution of particles results in a much greater potential for interaction between particles and the downstream oil and gas platforms. The rotational component of the flow field in the surface layer is revealed by the loops and filaments that develop in the patch shapes for the winter stratification case (Fig. 3.9).

3.6.4 Interbank transport

The potential for interbank exchange of larvae was estimated by computing the number of particles released from the upstream bank that pass within an arbitrary distance of the downstream bank (here, 4 km). Both the magnitude and the timing of interbank transport depend on the strength of the inflow velocity (Fig. 3.10). The peak in interbank particle transport occurs at ~ 2.7 days for $U = 16 \text{ cm s}^{-1}$, ~ 4.5 days for $U = 8 \text{ cm s}^{-1}$, and ~ 10 days for $U = 4 \text{ cm s}^{-1}$. All of these intervals are longer than in the absence of bank-induced flow disruption, with the greatest offset corresponding to slowest inflow (Fig. 3.10, no-bank estimates). The magnitude of interbank transport is always less than for the corresponding no-bank case because of alongshelf and cross-shelf dispersion of the particle patches, which were assumed to be zero for the no-bank

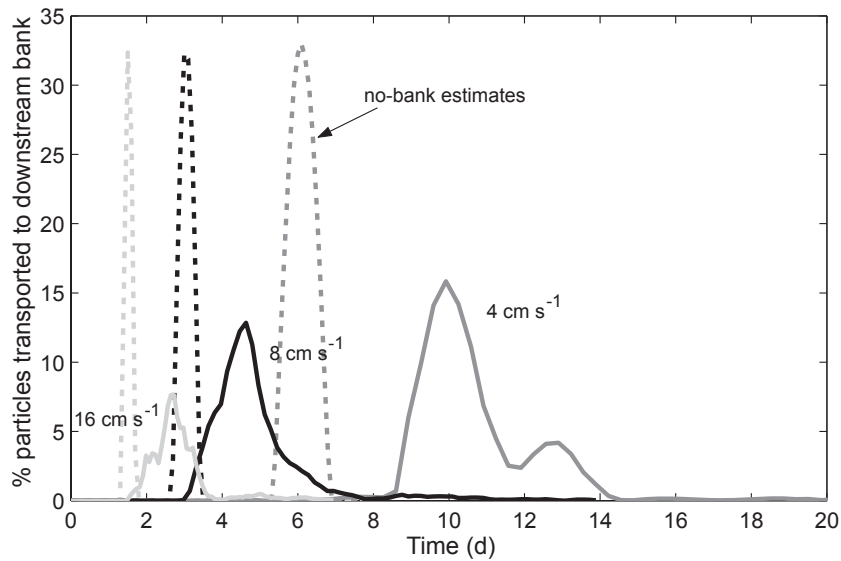


Fig. 3.10. Interbank particle transport for simulations A, B and C. Percentage of particles released from the upstream bank that pass within 4 km of the downstream bank as a function of time. No-bank estimates are based on advection of particle patches at the mean inflow speed.

estimates. Although the slowest inflow case leads to the largest peak in interbank transport in terms of particle numbers, the distance of closest approach is actually smallest for the fastest inflow case (1.3 km for $U = 16 \text{ cm s}^{-1}$ vs. 1.7 km for $U = 4 \text{ cm s}^{-1}$). For the no-bank estimates, the closest approach distance is 3.2 km. Faster inflow speeds correspond to shorter time windows over which interbank transport may occur and fewer particles involved in transport, but the particles that are involved tend to come closer to the downstream bank than they do for slower inflow.

When the inflow is reversed, potential interbank particle transport is enhanced. The maximum number of particles originating from the upstream bank that are within 4 km of the downstream bank increases from $\sim 13\%$ to $\sim 18\%$ and the time window over which transport occurs increases from ~ 5 days to ~ 10 days (Fig. 3.11). The longer time window is at least partly attributable to stronger retention of particles by the upstream bank for the reversed flow case (Fig. 3.6b), which acts to extend the time over which the upstream bank can act as a source of particles for the downstream bank. Deflection of flow in the gap between the two banks is weaker for the reversed flow case, which can account for the larger peak in maximum number of particles near the downstream bank,

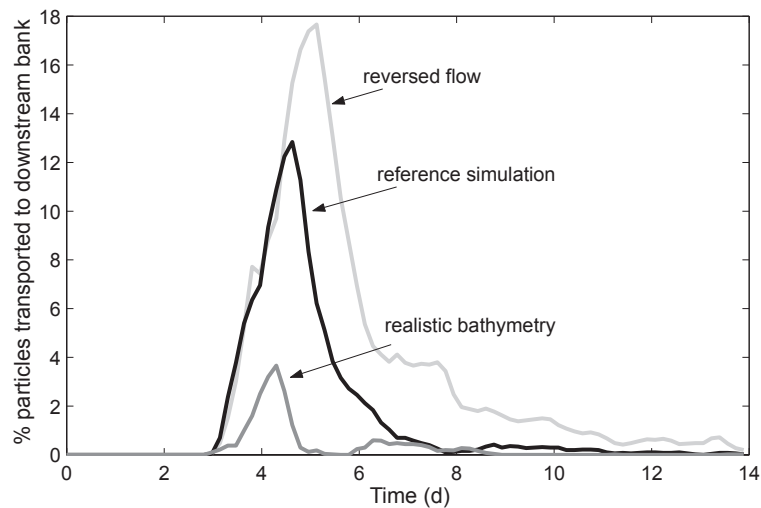


Fig. 3.11. Interbank particle transport for simulations B, D and G. Percentage of particles released from the upstream bank that pass within 4 km of the downstream bank as a function of time.

as well as the distance of closest approach being smaller for reversed flow (1.0 km vs. 1.5 km for the reference case).

The use of more realistic bathymetry greatly reduces the potential for interbank particle transport. A maximum of $\sim 4\%$ of particles released from the upstream bank are within 4 km of the downstream bank and the time window for potential transport is just ~ 2 days (Fig. 3.11). The closest approach distance for the realistic bathymetry case is 2.8 km, almost double that of the reference case. The more oblong cross-section of the realistic upstream bank as compared to the Gaussian circle (Fig. 3.4, left panels) and the lack of regular vortex shedding behind the realistic bank results in a narrower band of particles extending downstream in the region between the two banks for the realistic case (compare particle distributions on day 4 in Fig. 3.7). Stronger off-shelf flow between the banks in the realistic case leads to cross-shelf dispersion of the particle cloud that is skewed toward the off-shelf direction, which reduces the potential for particle transport to the downstream bank.

3.6.5 Platform contacts

The magnitude and timing of the interactions between particles released from the banks and nearby oil and gas platforms were computed by counting particle-platform contacts, assuming that a contact occurs when the separation distance is 1 km or less. For simulations A–C, where only the inflow speed was varied, the greatest number of contacts occur during the first few days, with faster inflow speed resulting in more contacts (Fig. 3.12). Contacts during this period are dominated by interactions with two specific platforms (one at each bank), each located less than ~ 4 km downstream of its associated bank and close to the midline of the bank wake. Peak interaction occurs on day 1 for the 8 cm s^{-1} and 16 cm s^{-1} cases and involves 14% and 31%, respectively, of the 10,000 total particles released. For the 4 cm s^{-1} case, the peak in contacts involves almost 9% of the particles and occurs on day 2. The percentage of particles interacting with platforms remains at ~ 5 to 12% up to 7 days after release for $U = 16 \text{ cm s}^{-1}$, but falls to ~ 1 to 6% during this period for the slower inflow cases. After the first week, the percentage of particles contacting platforms is less than $\sim 6\%$ each day. Not shown in

Fig. 3.12 is the 4 cm s^{-1} data from day 21 to day 28; fewer than 1% of particles are in contact with platforms on each of these days.

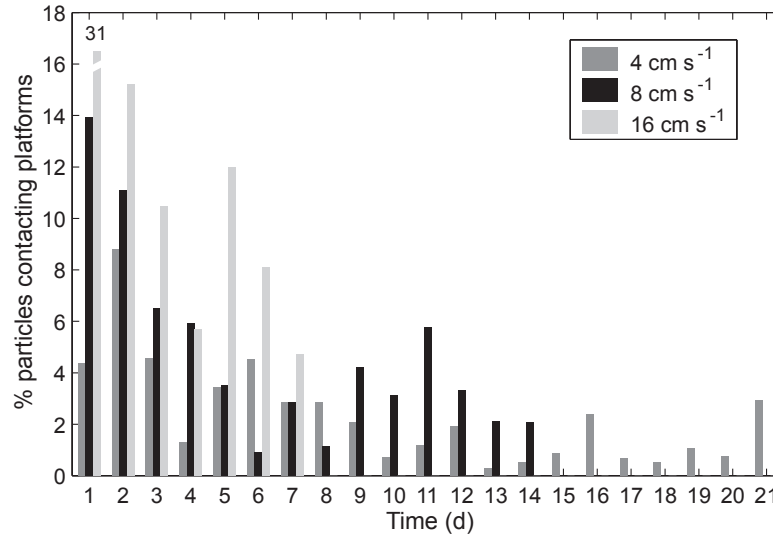


Fig. 3.12. Particle-platform contacts, simulations A, B and C. A contact occurs when a particle is within 1 km of a platform. Particles released from the two banks are combined so that each bar is based on 10,000 particles. Multiple contacts between the same particle-platform pair are not included.

The data in Fig. 3.12 provide a minimum estimate of potential particle-platform interactions for two reasons. First, multiple contacts between the same particle and platform are not counted. Multiple contacts are most important for the two closest platforms mentioned previously, since they are located near the bank wakes where recirculation of water and retention of particles occurs. Second, in order to make a fair comparison of the *total* number of particle-platform contacts for the different inflow speeds, I scaled the time over which particles are tracked inversely with speed. Hence, the $U = 16 \text{ cm s}^{-1}$ data extend to 7 days, the $U = 8 \text{ cm s}^{-1}$ data to 14 days, and the $U = 4 \text{ cm s}^{-1}$ data to 28 days. These times correspond approximately to the times at which the first particles leave the model domain. Additional particle-platform contacts would occur in all cases, as most of particles remain within the domain when particle tracking stops.

Particle dispersal patterns as a function of topographic detail (Fig. 3.7) have a significant impact on particle-platform interactions. Use of the more realistic bathymetry results in fewer particle-platform contacts initially (Fig. 3.13, days 1–3). However, the tendency for particles to be swept up onto the shelf in the realistic case leads to much more interaction with platforms, starting on day 12 and continuing through day 21. The average percentage of particles in contact with platforms each day during this time span is 3% for the Gaussian bathymetry simulation and 6% for the realistic bathymetry simulation.

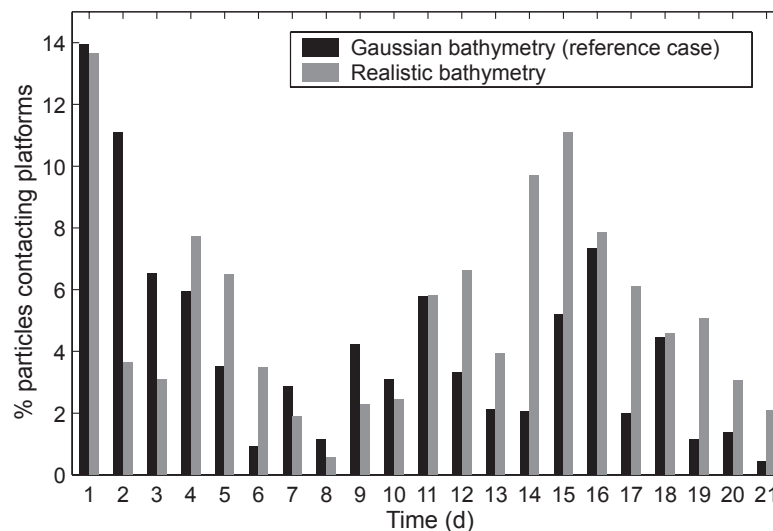


Fig. 3.13. Particle-platform contacts, simulations B and G. A contact occurs when a particle is within 1 km of a platform. Particles released from the two banks are combined so that each bar is based on 10,000 particles. Multiple contacts between the same particle-platform pair are not included.

Twelve platforms, all located in a relatively narrow (<20 km) cross-shelf band directly downstream of the banks, are contacted by particles in the reference Gaussian bathymetry simulation (Fig. 3.14a). Over the course of a 21-day simulation, a total of 10,527 contacts occur, not including multiple particle-platform contacts. Platforms located nearest the cross-shelf midline of the domain are contacted most often, while those found either on-shelf or off-shelf of the midline experience fewer particle contacts.

When the more realistic topography is used, particles come into contact with many more platforms (33 total), covering a broader (~35 km) cross-shelf swath of the model domain (Fig. 3.14b). While the number of platforms affected is nearly triple that of the reference case, the total number of particle-platform contacts over 21 days is only ~35% larger, at 14,152. The tendency of particles to be swept onto the narrowing shelf in the realistic bathymetry simulation is clearly reflected in the distribution of the platforms that are contacted by those particles.

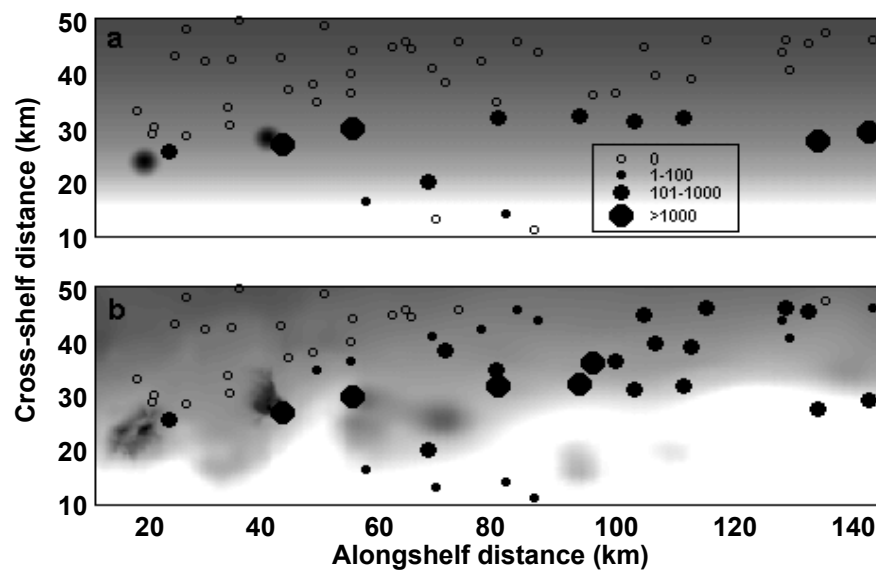


Fig. 3.14. Particle-platform contacts as a function of platform location. A contact occurs when a particle is within 1 km of a platform. Multiple contacts between the same particle-platform pair are not included. (a) Simulation B (Gaussian bathymetry reference). (b) Simulation G (more realistic bathymetry).

For the eastward inflow simulations (includes all except simulation D), a larger fraction of the particles released from the downstream (east) bank contact platforms than do those released from the upstream (west) bank (Table 3.2). This is partly a result of large numbers of contacts with the platform that is located just ~2.5 km downstream and almost directly in the wake of the downstream bank. It is also due to the preponderance of platforms located on the shelf as opposed to on the slope. Since the downstream bank

Table 3.2. Particle-platform contact data. Total # of particle-platform contacts includes multiple contacts between the same particle-platform pair and contacts of the same particle with multiple platforms. WB–West Bank; EB–East Bank.

Simulation	Source of particles	# platforms contacted	# particles contacting at least one platform	Total # of particle-platform contacts
A (4 cm s ⁻¹)	WB	7	972 (19%)	2856
	EB	7	3299 (66%)	24590
	both	9	4271 (43%)	27446
B (8 cm s ⁻¹)	WB	7	994 (20%)	1318
	EB	10	3219 (64%)	12153
	both	11	4213 (42%)	13471
C (16 cm s ⁻¹)	WB	9	2236 (45%)	2252
	EB	10	3583 (72%)	9216
	both	12	5819 (58%)	11468
D (reversed)	WB	7	4320 (86%)	7428
	EB	20	4907 (98%)	21743
	both	21	9227 (92%)	29171
E (unsteady)	WB	13	2142 (43%)	3688
	EB	12	3406 (68%)	9682
	both	15	5548 (55%)	13370
F (winter)	WB	10	2142 (43%)	3189
	EB	11	4105 (82%)	21890
	both	15	6247 (62%)	25079
G (real, steady)	WB	10	1187 (24%)	1988
	EB	15	4018 (80%)	24910
	both	20	5205 (52%)	26898
H (real, unsteady)	WB	13	2427 (49%)	4167
	EB	17	3945 (79%)	14902
	both	23	6372 (64%)	19069

is offset from the upstream bank in the on-shelf direction, particles released from it are more likely to encounter platforms.

The number of platforms contacted by particles increases slightly with increasing inflow speed; the fraction of particles involved in those contacts is about the same for the 4 cm s^{-1} and 8 cm s^{-1} inflows, but increases by $\sim 40\%$ for the 16 cm s^{-1} case (Table 1, simulations A–C). The difference between the number of particles contacting at least one platform and the total number of particle-platform contacts, as shown in Table 1, provides a measure of the frequency of multiple particle-platform contacts. This includes contacts between a single particle and multiple platforms as well as multiple contacts between the same particle-platform pair. Multiple contacts occur less frequently as inflow speed increases. The relative difference between number of particles involved in contacts and total number of contacts is six-fold for $U = 4 \text{ cm s}^{-1}$, three-fold for $U = 8 \text{ cm s}^{-1}$, and two-fold for $U = 16 \text{ cm s}^{-1}$.

For the reversed flow simulation (D), twice as many platforms are contacted as compared to the reference simulation and a much larger percentage of particles released (92%) contact at least one platform. This enhancement in particle-platform interaction is primarily due to the larger number of platforms located directly downstream of the Flower Garden Banks to the west than to the east (cf. Fig. 3.15 and Fig. 3.9). In addition, the Coriolis effect in this case acts to deflect flow (and particles) on-shelf, where more platforms are located, instead of off-shelf, as is the case for eastward flow.

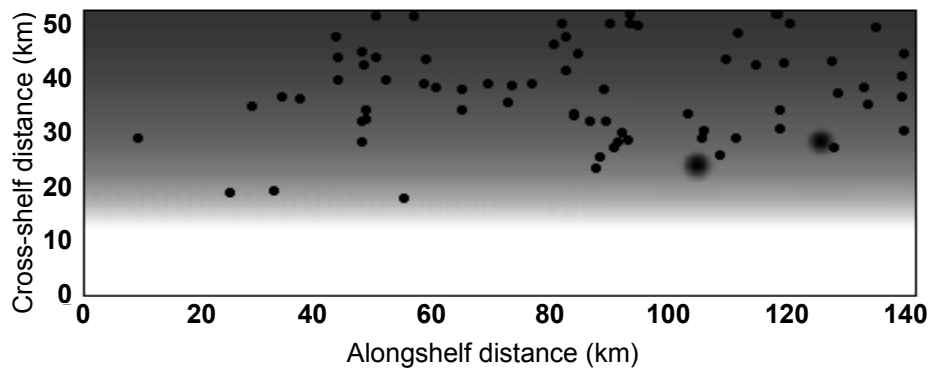


Fig. 3.15. Platform locations for reversed inflow simulation.

Unsteady forcing (simulation E) is associated with larger cross-shelf flow disturbances, which acts to bring particles in contact with a greater number of platforms (15 vs. 11 for steady inflow). The number of particles contacting platforms increases by ~30%, but total particle-platform contacts remain about the same as for reference simulation B. This implies that multiple contacts occur relatively less frequently for unsteady forcing.

When weaker stratification is specified (simulation F), the broader wake regions extending downstream of the bank enhance cross-shelf dispersion of particles. Both the number of platforms contacted and the number of particles involved increase by ~50%. The overall interaction potential, measured in terms of the total number of contacts, is double that of the reference case.

The more realistic bathymetry simulations (G and H) result in the largest numbers of platforms being contacted by particles, a result of the on-shelf deflection of the flow. Note that the values listed for number of platforms contacted in Table 3.2 for simulation G and reference simulation B are smaller than those shown in Fig. 3.14 because the Table 3.2 data are for 14-day rather than 21-day simulations. Multiple contacts are relatively more frequent for the steady inflow, realistic bathymetry case as compared to the reference. The addition of unsteady forcing has a similar effect as noted in the Gaussian case, with greater numbers of platforms and particles interacting but relatively fewer multiple contacts occurring.

3.7 Discussion

The tendency of particles to stay near their release points atop the modeled banks is a result of topographically generated flow fields, in particular the return-flow wake regions that exist just downstream of each bank. To the extent that the model represents a simplified version of the Flower Garden Banks coral reef ecosystem, particle retention can be viewed as a proxy for the self-seeding potential of the corals that live on the banks and reproduce by releasing larvae into the water column. The time scales of particle retention are relatively short for all simulations, with 50% of particles lost within 2 days and 95% lost within one week (except for the slowest inflow, where 95% loss

corresponds to ~10 days). This implies that maintenance of the coral populations at the banks via self-seeding of larvae is more likely for species whose larval pre-competency periods are shorter than one week. Brooding corals should be favored over spawners, as they generally have much shorter pre-competency periods (hours to days vs. one to two weeks). However, a recent study has documented minimum pre-competency periods of 2.5–2.75 days for two spawning coral species (Miller and Mundy, 2003). If also true for spawners found at the Flower Garden banks, this would make them much more competitive with brooders on the short time scales associated with near-bank particle retention.

The trends in particle retention predicted by the model simulations are most applicable to brooding corals because of the short time scales involved and also because spawned coral larvae tend to be positively buoyant when initially released (Wolanski et al., 1989; Hagman et al., 1998). Positive buoyancy would prevent these larvae from being entrained in the wake regions and larval loss rates would be much higher. For the case of summer stratification, where surface-layer flow is effectively decoupled from flow below the level of the bank tops, surface-released particle loss rates are similar to the no-bank estimates shown in Fig. 3.5. For winter stratification, where the flow disturbances extend to the surface, loss rates are somewhat lower (note the initial lag in downstream advection of winter-stratification particles in Fig. 3.9), but still greatly exceed the loss rates for neutrally buoyant particles. Black et al. (1991) noted that such depth-dependent variation in particle retention around coral reefs points to the importance of incorporating full three-dimensional physics into hydrodynamic models designed to study larval transport processes.

The greatest variation in particle retention times is attributable to inflow speed, with faster inflows resulting in less retention. Similar negative relationships between inflow speed and particle/larval retention have been observed and modeled by Wolanski et al. (1989), Black (1993) and Kloppmann et al. (2001). My model results indicate that faster inflows are associated with more frequent vortex shedding and stronger cross-shelf flows in the wake regions, both of which inhibit particle retention. Particles entrained in the

vortices are swept away more quickly, and particles transported cross-shelf away from the midline of the wake region are subjected to stronger downstream advection by the free-stream flow. These mechanisms overwhelm the larger wake volumes and stronger return-flow velocities produced by faster inflows.

Differences in particle retention between the upstream and downstream banks result from the upstream bank influencing the flow structure around the downstream bank. In all of the Gaussian bathymetry simulations except for the slowest inflow and unsteady inflow cases, the wake volumes and vortex shedding frequencies at the downstream bank are reduced, as is overall particle retention. The differences in retention, though in some cases subtle, demonstrate that the East and West Flower Garden Banks are not hydrodynamically isolated from one another and that studies of flow and larval transport in the area should incorporate interbank influences.

The most significant difference in particle retention for the realistic bathymetry compared to the reference case is the enhanced retention at the downstream (east) bank. This enhancement is consistent with results of Coutis and Middleton (2002), who found more effective particle retention in island wakes when island cross-sections presented bluff-body rather than more streamlined profiles to the oncoming flow.

The Flower Garden Banks are thought to act as sources of coral larvae to the numerous other natural banks and thousands of offshore oil and gas platforms that are located on the continental shelf and slope of the northern Gulf of Mexico. None of the other natural topographic banks support reef-building coral populations of comparable abundance to those of the Flower Garden Banks, mostly as a result of them having deeper crest depths, which deprives the corals of light, or locations closer to shore, which exposes the corals to unacceptably cold wintertime temperatures. Estimates of the dispersal potential of larvae released from the Flower Garden Banks help us understand the biological connectivity of shelf banks and platforms.

Dispersal of particles in the model is predominantly in the alongshelf direction, as dictated by the unidirectional alongshelf inflow. The time required for the first particles to reach the downstream boundary of the domain varies from ~1 week for $U = 16 \text{ cm s}^{-1}$

to ~ 1 month for $U = 4 \text{ cm s}^{-1}$. For a given mean alongshelf speed, larvae with long pre-competent periods will be transported further from the banks before they are able to settle than will those with shorter pre-competent periods. Thus, the dispersal potential of particles as predicted by the model must be augmented with knowledge of the pre-competent and competent periods of larvae to obtain better estimates of actual settlement patterns. Since the maximum competency period of brooded coral larvae is thought to be ~ 1 month, and that of spawned larvae is thought to be at least 3 months, dispersal of competent larvae beyond the boundaries of the model domain is likely for both larval types.

Cross-shelf dispersion of the particle patches increases as a result of the increased cross-shelf wake velocities associated with faster inflows. The total horizontal area of influence of the particle patches is thus larger for faster inflows, but their residence times within the model domain are shorter. The computed effective mixing coefficients in the alongshelf direction reach their peak values early in the simulations and then approach stable values on the order of $10\text{--}100 \text{ m}^2 \text{ s}^{-1}$. This is consistent with Black (1993), who estimated horizontal dispersal rates of $55 \text{ m}^2 \text{ s}^{-1}$ for particles released on a coral reef subject to an 8 cm s^{-1} alongshelf flow. Black's model also included tidal flow of comparable magnitude directed perpendicular to the alongshelf flow, resulting in an effective mixing coefficient that was the same in both the cross-shelf and alongshelf directions. Estimated cross-shelf effective mixing coefficients in my model were an order of magnitude smaller than alongshelf estimates. I would expect the addition of cross-shelf tidal forcing to the model to similarly increase cross-shelf particle dispersal rates, but since tidal velocities at the Flower Garden Banks are typically slower than the alongshelf current and since their strength diminishes with depth, the magnitude of the increase should not be dramatic.

The differences in bank shapes and sizes between the more realistic bathymetry and the Gaussian approximations leads to differences in particle retention capability; the added complexity of the shelf-slope geometry downstream of the banks in the more realistic case similarly impacts longer distance particle dispersal patterns. Particle

patches are displaced, as a whole, in the onshore direction and up onto the shelf for the more realistic bathymetry simulations. The cross-shelf dispersion of the particle clouds that is superimposed on this on-shelf displacement is significantly larger than that of the reference case. While use of the greatly simplified bathymetry may provide reasonable estimates of alongshelf particle dispersal rates, cross-shelf dispersal is underestimated, and the locations of the particle clouds with respect to other topographic banks and man-made structures downstream differs dramatically.

Dispersal patterns of particles released in the upper layers of the water column, above the crest depth of the modeled banks, depend strongly on the specified strength of water-column density stratification. The dispersal predicted for both strong and weak stratification is certainly underestimated by the model, since both wind forcing and tidal forcing are expected to play major roles in the surface layers and are neglected here. Still, the differences in dispersal between the two cases is significant and can be expected to persist.

My use of simple unidirectional inflows and neglect of surface wind forcing, tidal forcing, and any influences of loop current eddies impinging on the slope, results in particle dispersal dominated by eastward advection of the particle patches (except for the reversed flow simulation) with relatively little cross-shelf dispersion. This dispersal pattern coincides with two of the primary dispersal modes observed by Lugo-Fernández et al. (2001) for satellite-tracked surface drifters released near the Flower Garden Banks. The first mode consisted of a continuous eastward displacement of drifters, to a distance of ~200 km downstream of the banks; the second involved an initial eastward displacement (well beyond the bounds of my model domain) followed by a turn to the northwest and eventual westward transport along the inner continental shelf. A third mode of drifter transport observed in this study consisted of offshore displacement via entrainment in eddies. This points to the importance of eventually incorporating the influence of loop current eddies into models of flow and particle transport near the Flower Garden Banks.

Maintenance and expansion of the coral populations at the Flower Garden Banks via local (i.e. bank-specific) sources of larvae seems likely, as the flow structures generated by the local topography have been shown to retain particles on biologically relevant time scales. The relatively short distance between the two banks (~20 km) and their orientations with respect to the mean current direction also make it likely that larvae released at one bank can be transported to the other and potentially settle there. My estimates of the potential for such interbank larval exchange based on passive particle trajectories show that faster alongshelf current speeds lead to reduced interbank transport. It was noted in Chapter II that the magnitude of off-shelf volume transport in the region between the two banks increased with faster inflows. This off-shelf deflection of the flow inhibits interbank particle transport, as particles are carried further offshore of the downstream bank. Even though the total number of particles involved in interbank transport is smaller for faster inflow, the greater cross-shelf dispersion associated with faster speeds leads to a reduction in the distance of closest approach.

The time at which maximum interbank particle transport occurred for each of the inflow speeds I tested ranged from ~3 to 10 days. For spawned larvae, many of which are competent to settle only after 5–7 days, faster alongshelf speeds may bring them close to the downstream bank before their pre-competent period has ended. Brooded larvae, with their generally much shorter pre-competent periods, are expected to be competent to settle upon reaching the downstream bank for all flow speeds tested.

Lugo-Fernández et al. (2001) documented surface drifters released near the West Flower Garden Bank passing over the East Bank in 1–3 days, which corresponds to a mean eastward current velocity of ~8–23 cm s⁻¹. None of the drifters released at the East Bank were transported directly to the West Bank in their study, indicating that westward flow was not present during the times of drifter release in August for three different years. Nonetheless, since westward flows have been measured at buoys near the banks, often persisting for one week at a time and occasionally lasting 2–3 weeks (DiMarco et al., 1997), I included a westward flow case among the simulations. Particle transport from the upstream to the downstream bank in this case is more effective than for the

reference eastward inflow case, both in terms of total numbers of particles transported and the time window over which transport occurs. This is due to weaker flow deflection in the gap between the banks and stronger retention of particles near the upstream bank, which acts to extend the time period over which transport to the downstream bank occurs. The peak in interbank particle transport occurs five days after release. Thus, although the alongshelf current near the Flower Garden Banks is usually directed to the east, the flow reversals that do occur generally persist long enough for particles (and potentially larvae) to be transported from the East Bank to the West Bank.

Interbank transport of particles is less effective when the more realistic bathymetry is specified along with steady eastward inflow. The shape and orientation of the upstream bank and the stronger off-shelf flow between the banks contribute to reduced particle transport. Westward flow over the more realistic bathymetry, though not simulated here, may greatly enhance the potential for interbank particle transport. The mechanisms causing enhanced transport for the Gaussian bathymetry simulation are expected to remain, and the larger area over which particles are initially distributed on the East Bank is expected to lead to a larger patch size, bringing more particles close to the West Bank.

Recruitment of coral larvae to offshore oil and gas platforms in the northern Gulf of Mexico serves to increase the number of coral colonies inhabiting the area and to broaden their distributions over the continental shelf (Bright et al., 1991; Sammarco et al., 2004). Platforms may act as stepping stones of coral colonization between the Flower Garden Banks and surrounding banks that harbor smaller coral populations. They may also help promote long-distance larval exchange between the Flower Garden Banks and remote reefs in Florida, the Caribbean and Mexico. My results indicate that particles released at the Flower Garden Banks have high likelihoods of coming into contact with offshore platforms. This implies that the supply of Flower Garden Banks larvae to platforms is good, which is an essential first condition for actual settlement and survival to adulthood.

The timing of particle-platform contacts with respect to larval pre-competent and competent periods further constrains the potential for larval recruitment to platforms. For

instance, the maximum number of contacts in my simulations occurs during the first 1–3 days after release. Many spawned larvae would still be pre-competent during this period, and thus would not be able to take advantage of being near a presumably suitable substrate. We might expect to find larger numbers of brooding coral species on platforms located closest to the banks, as they are usually competent to settle within hours of release. However, recent surveys of coral populations on a set of 13 platforms located within 50 km of the Flower Garden Banks showed no significant trends in terms of reproductive strategy vs. distance from the banks (Sammarco et al., 2004). Brooders and spawners were found in nearly equal abundances on the platforms studied, which included three platforms that were located west of the banks.

The most important factor influencing spatial and temporal patterns in particle-platform contacts in my simulations is the use of more detailed shelf topography. The on-shelf deflection of the flow combined with the large number of platforms on the shelf makes for a large increase in particle-platform interactions as compared to the reference simulation with Gaussian banks and a smooth, uniform shelf-slope. The potential for larval recruitment to offshore platforms is thus greatly improved in the realistic bathymetry case. My results can be interpreted in terms of potential larval supply to offshore platforms, but quantitative predictions of platform settlement and survival rates would need to incorporate knowledge or estimates of local environmental conditions, substrate suitability, and pre- and post-settlement mortality rates.

3.8 Conclusions

The results of my coupled hydrodynamic/particle-tracking model support the idea that the corals of the East and West Flower Garden Banks act as sources of larvae to themselves, to one another, and to nearby oil and gas platforms in the northern Gulf of Mexico. Retention of particles near their release locations points to the potential for self-seeding of coral populations, and is a result of temporary trapping within the return-flow wake regions that form just downstream of each bank. The time scale of effective particle retention is most sensitive to changes in the free-stream current speed. Interbank transport of particles provides a measure of the likelihood of larval exchange between

the two banks. The relative magnitude of interbank particle transport is inversely related to the strength of the cross-shelf flow in the region between the banks. Dispersal of particles downstream of the banks brings many of them into contact with offshore oil and gas platforms, implying that the supply of larvae from the Flower Garden Banks to these platforms is large for a variety of inflow and stratification conditions. Particle-platform interactions increase substantially when more realistic bathymetry is specified in the model. Topographically generated flow fields exert a strong influence on passive particle transport and cannot be ignored in studies of larval dynamics near the Flower Garden Banks.

CHAPTER IV

PLANKTON DYNAMICS

4.1 Overview

Abrupt changes in bathymetry steer ocean currents. The altered local flows can influence planktonic food web structure and dynamics. Topographically generated turbulence can enhance mixing of nutrients into the euphotic zone; water trapped in recirculation regions can cause localized accumulation of planktonic biomass. In this chapter, I use a fully three-dimensional coupled physical-biological model to explore the effects of submerged topography on flow and plankton dynamics in a system modeled on the Flower Garden Banks in the northern Gulf of Mexico.

In the earlier chapters, I showed how simplified representations of the Flower Garden Banks altered the flow around them in ways that could have biological consequences. The Banks, represented in the model by two Gaussian peaks, are located near the shelf break and rise from 150–200 m to within 20 m of the sea surface. The simulated Gaussian peaks generate vortices that are transported downstream under the influence of a steady, uniform alongshelf inflow. Mixing in the wake regions just downstream of the peaks leads to upwelling of a passive tracer with an initially nutrient-like vertical distribution. Thus, the topographically-influenced flow field is capable of bringing nutrients from deeper water into shallower areas of the euphotic zone.

In this chapter, a simple nutrient-phytoplankton-zooplankton ecosystem model is coupled to the physical model and predicts increases in plankton biomass in the wake regions. Phytoplankton biomass in the wake is up to three times greater than background levels; zooplankton biomass is enhanced by up to a factor of two. The region of elevated plankton biomass extends more than 100 km downstream of the peaks after 21 days. If such increases in planktonic biomass occur at the Flower Garden Banks, they may serve as a locally enriched food source to the higher trophic level organisms that live on and around the Banks in an otherwise oligotrophic environment.

4.2 Introduction

Enhanced plankton biomass concentrations observed over shallow seamounts and in the wakes of islands in the ocean have been attributed to a number of physical mechanisms. For seamounts, the focus has been on the doming of isopycnals that is associated with the formation of Taylor caps, which are closed circulation cells formed directly atop seamounts. The upwelling of nutrient-rich water that presumably occurs along with the isopycnal doming may spur phytoplankton growth. Dower et al. (1992) measured chlorophyll concentrations as much as five times higher than background values above Cobb Seamount in the North Pacific and suggested they resulted from Taylor cap formation. Current meter data from this study indicated the existence of a circular flow pattern around the top of the seamount. A subsequent study of nutrient concentration, phytoplankton biomass and primary production at Cobb did not find nutrient upwelling or enhanced biomass, but did reveal an increase in primary productivity (Comeau et al., 1995). The alternative mechanism proposed was enhanced water-column stability over the seamount leading to an improved subsurface light regime for the phytoplankton. Comeau et al. (1995) concluded that the high chlorophyll concentrations observed by Dower et al. (1992) were most likely a transient phenomenon.

For surface-penetrating islands and reefs, enhanced biological activity in the wake regions has traditionally been attributed to runoff of nutrients from land or lagoon drainage. Recent work has shown, however, that flow-topography interactions can themselves account for observed increases in nutrient levels. Rissik et al. (1997) and Coutis and Middleton (1999) documented nutricline uplift and an accompanying 40% increase in nutrient concentration in the wake of an isolated reef with negligible land runoff and a small, shallow lagoon. Both phytoplankton and zooplankton abundances were elevated in the wake as well. A detailed study of an island wake by Hasegawa et al. (2004) showed a seven-fold increase in nitrate concentration and a one- to two-order-of-magnitude increase in turbulent dissipation compared to upstream observations.

The inspiration for the present study comes from an interest in how flow-topography interactions might impact nutrient and plankton dynamics at the Flower Garden Banks, a pair of small and relatively isolated coral reef ecosystems in the northwestern Gulf of Mexico. The reefs are similar to seamounts in that they are submerged beneath 20 m of seawater, but typical flow conditions are not conducive to the formation of Taylor caps (see chapter II). My hydrodynamic model of the Banks did, however, predict regions of temporary water trapping in the lee of each bank and isopycnal displacements in the wakes (chapter II). The mechanisms of local upwelling and recirculation thought to be important for seamounts may function in modified form at the Flower Garden Banks.

Simulated flow past the Banks is similar to flow past a surface-penetrating island, such as that studied by Hasegawa et al. (2004), in that turbulent wakes are generated and, hence, turbulent mixing rates in these wakes are elevated. Increased vertical mixing may serve to bring nutrient-rich water up into the euphotic zone where it can stimulate phytoplankton growth.

The goal of this study is to use a coupled hydrodynamic-ecosystem model, configured to represent the Flower Garden Banks, to test the ability of topographically generated flow disturbances to change plankton dynamics via nutrient injection into the euphotic zone.

4.3 The Flower Garden Banks

The Flower Garden Banks are located in the oligotrophic waters of the outer continental shelf in the northwestern Gulf of Mexico, approximately 200 km south of the Texas-Louisiana border. They rise from depths of 100–150 m to approximately 20 m, where temperature and light penetration are sufficient to sustain thriving coral reef ecosystems.

Surface waters near the Banks are depleted in nitrate, with concentrations lower than $0.1 \mu\text{M}$ extending from the surface to ~ 50 m in the summer and to ~ 80 m in the winter (Jochens et al., 1998). Mean mixed-layer phytoplankton standing stock is also very low, at ~ 0.1 to $0.5 \text{ mg Chla m}^{-3}$, and integrated water column primary productivity is estimated at ~ 0.2 to $0.4 \text{ g C m}^{-2} \text{ d}^{-1}$ (Chen et al., 2000). No studies of zooplankton

biomass or secondary production have been published for the Flower Garden Banks region.

4.4 The Hydrodynamic Model

I used the Regional Ocean Modeling System (ROMS), described in detail by Haidvogel et al. (2000) and Marchesiello et al. (2003), to model the flow field in the region of interest. ROMS is a free-surface hydrostatic model that solves the primitive equations of motion using finite-difference approximations on orthogonal coordinates in the horizontal and a stretched, terrain-following coordinate in the vertical.

The model was configured as for the reference simulation described in chapters II and III. Briefly, the topography of the Flower Garden Banks and their surroundings was approximated by Gaussian peaks rising from a smooth, uniform shelf-slope (Fig. 4.1). The horizontal resolution of the grid varied from 2000 m at the boundaries to 200 m over a region centered on the peaks. Vertical resolution was 0.5 m over the tops of the peaks and 3–11 m at maximum depth. The f -plane assumption was made; i.e. there was no latitudinal variation in the Coriolis parameter.

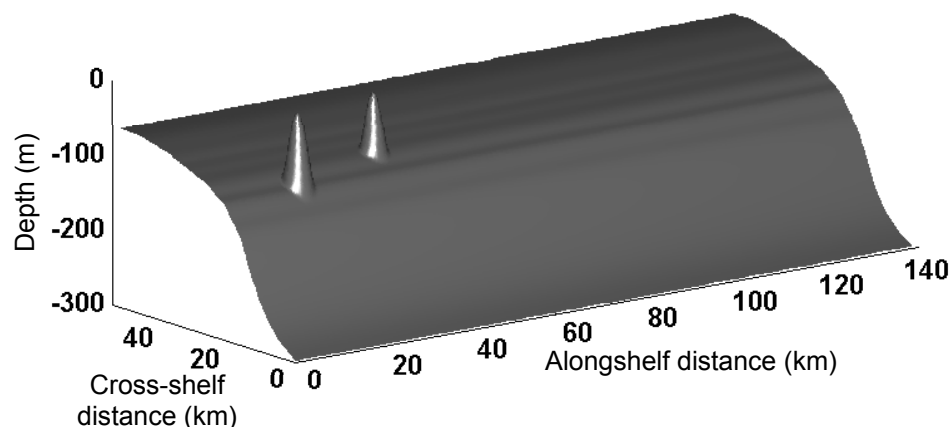


Fig. 4.1 Model bathymetry.

Initial water column stratification was set by choosing a typical summertime potential temperature vertical profile from data gathered near the Flower Garden Banks during the LATEX program (Jochens et al., 1998). Salinity was assumed constant. A

preliminary simulation was conducted that included a passive tracer with a nitrate-like initial vertical distribution, characterized by depletion in the surface layer down to about 50 m and increasing with further depth (Fig. 4.2). This initial tracer distribution was also based on LATEX data for nitrate concentrations near the Flower Garden Banks in summer.

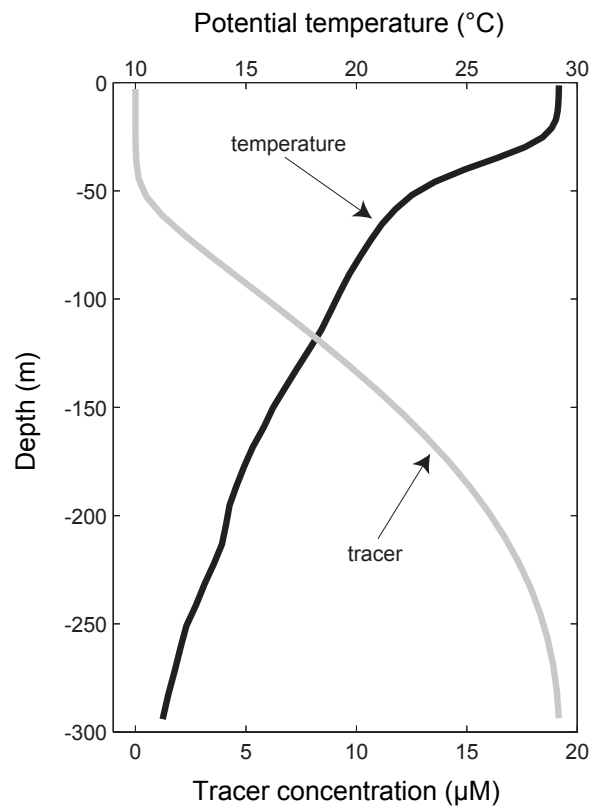


Fig. 4.2 Initial vertical profiles of temperature and nutrient-like tracer.

The simulation started with the water at rest throughout the domain; flow was imposed as a uniform eastward barotropic velocity at the upcurrent boundary. The velocity was increased gradually from zero to 8 cm s^{-1} over a period of three days and then held constant for the subsequent 18 days. The onshore and offshore boundaries of the domain were closed, while the upcurrent and downcurrent boundaries were open and subject to radiation-type transfer of mass and momentum.

4.5. Flow Disruption and Nutrient Upwelling

4.5.1 *General features of the flow*

Flow over and around the Gaussian peaks is characterized by vigorous vortex shedding and by strong return flows immediately downstream of each peak. Disturbance of the flow is strongest in the near-wake regions, where vortex formation leads to an increase in relative vorticity of more than five times the background rotation rate (Figs. 2.10c, 2.11). Maximum turbulent mixing rates in the wakes are 2–20 times the background value (Fig. 2.13). There are dynamic recirculation regions extending several km downstream of each modeled bank where the magnitude of the reversed alongshelf flow can reach ~70% of the forcing speed (Figs. 2.9c, 3.4).

4.5.2 *Upwelling of a passive tracer*

I studied the effects of flow disruption on nutrient concentration using the preliminary simulation, which included a passive tracer with a nitrate-like vertical distribution. Horizontal sections at 50 m, focused on the region near the upstream bank, show tracer concentrations increasing in the wake region through time (Fig. 4.3). Results are similar for the downstream bank.

Upwelling of the passive tracer is strongest immediately downstream of the modeled bank, where concentrations reach $0.65 \mu\text{M}$, a 60% increase over the background value of $0.4 \mu\text{M}$. In the nominal tracer vertical profile, $0.65 \mu\text{M}$ corresponds to a depth of about 54 m, so the tracer isopleths are uplifted 4 m in the immediate lee of the bank. A plume develops in the wake of the bank, with tracer concentrations remaining above $0.5 \mu\text{M}$ out to 2.5–3 km downstream. The plume narrows as it extends further downstream and the tracer concentration within it drops to 10–15% above background.

The flow disruption caused by the modeled banks is apparently capable of inducing upwelling of a nutrient-like passive tracer in the bank wakes. The next step is to address whether this local enhancement of nutrient concentration is sufficient to affect phytoplankton growth.

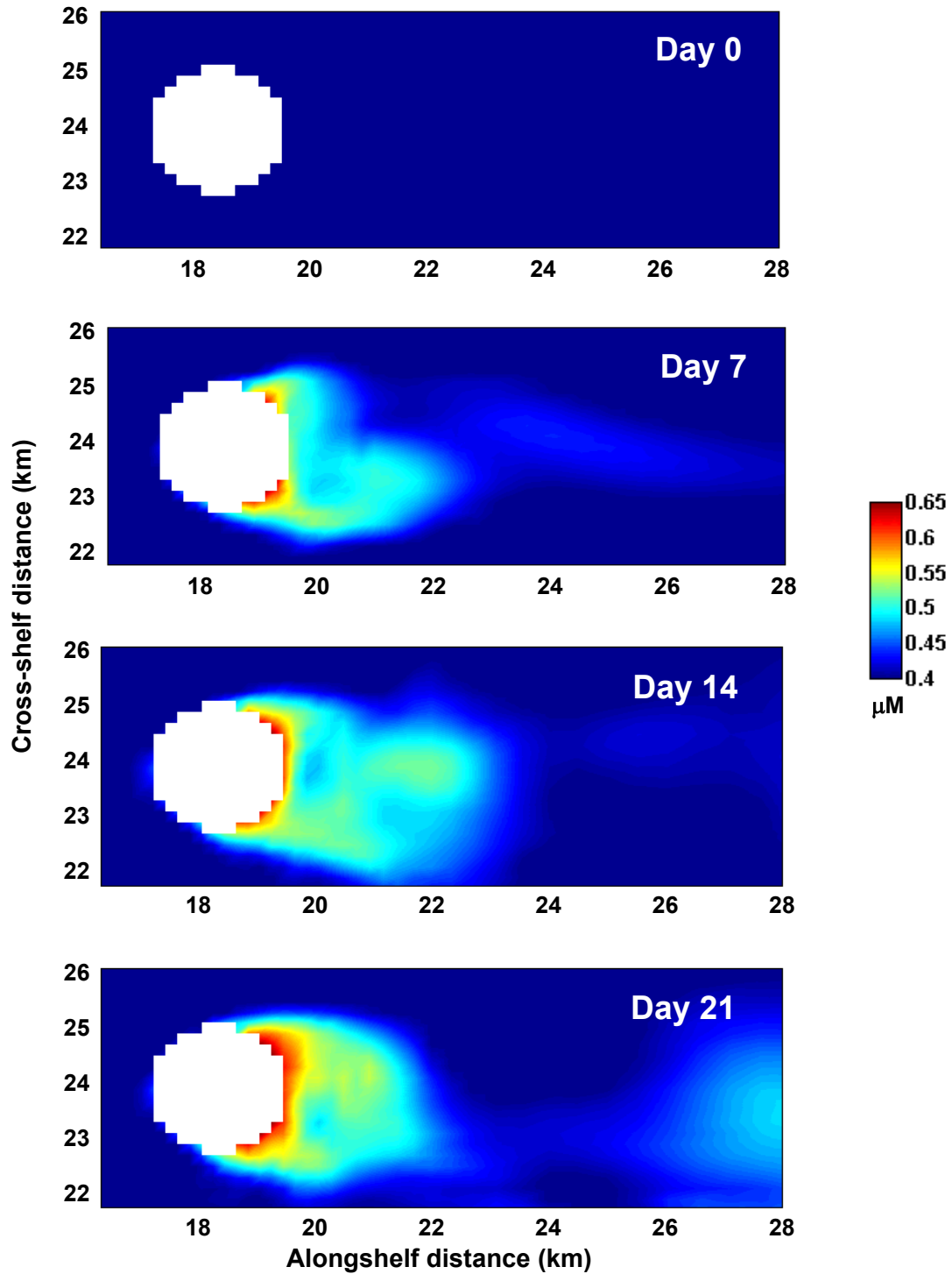


Fig. 4.3 Upwelling of a nutrient. Horizontal sections at 50 m in the vicinity of the upstream bank.

4.6. The Ecosystem Model

The ecosystem model describes interactions among four biological compartments: nitrate, ammonium, phytoplankton and zooplankton (Fig 4.4). Nitrogen is the model currency. Although bacteria and detritus are important components of all planktonic ecosystems, my aim here is not to construct the most complete, realistic food web possible. Instead, my primary interest is in simply testing the hypothesis that the nutrient enrichment shown by the preliminary simulation can impact phyto- and zooplankton dynamics. My approach is to first obtain a quasi-steady-state solution of the model system in one spatial dimension (depth); the results are then used as initial conditions in the three-dimensional time-dependent coupled model.

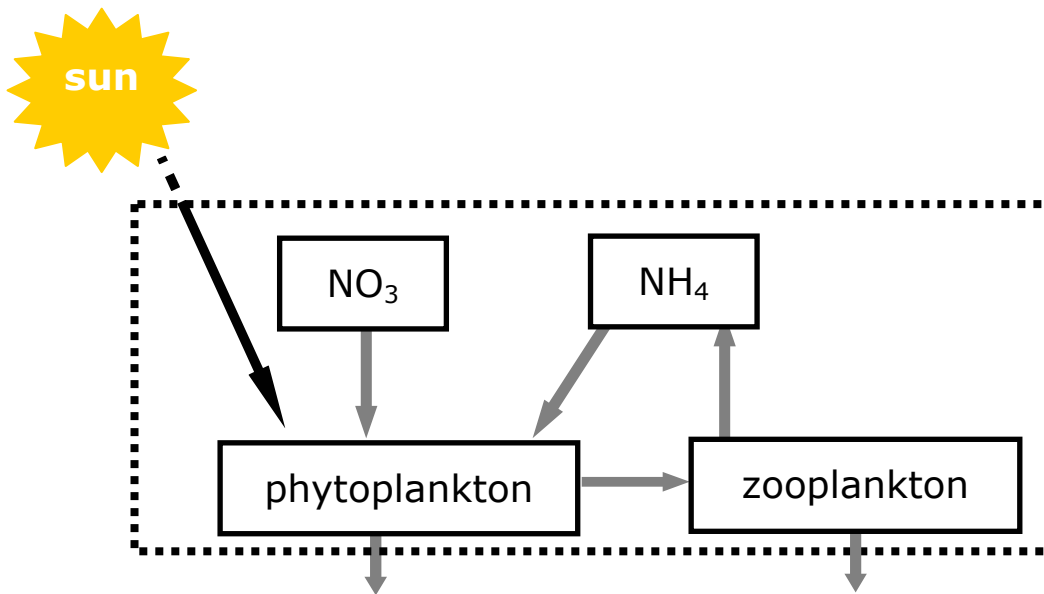


Fig. 4.4 Diagram of the ecosystem model.

4.6.1 Model equations and parameter values

The set of differential equations governing the one-dimensional ecosystem model is very similar to that used by Fasham et al. (1990), but with vertical mixing terms included

for each state variable:

$$\begin{aligned}\frac{\partial P}{\partial t} &= JQP - gZ \frac{P}{K_p + P} - m_p P + K_z \frac{\partial^2 P}{\partial z^2} \\ \frac{\partial Z}{\partial t} &= \gamma gZ \frac{P}{K_p + P} - m_z Z - e_z Z + K_z \frac{\partial^2 Z}{\partial z^2} \\ \frac{\partial NO_3}{\partial t} &= -JQ_{NO_3} P + K_z \frac{\partial^2 NO_3}{\partial z^2} \\ \frac{\partial NH_4}{\partial t} &= -JQ_{NH_4} P + e_z Z + K_z \frac{\partial^2 NH_4}{\partial z^2}\end{aligned}$$

where

$$\begin{aligned}J &= \frac{\mu_m \alpha I}{(\mu_m^2 + \alpha^2 I^2)^{1/2}} \\ I &= I_o e^{-(k_w + k_p P)z} \\ Q &= Q_{NO_3} + Q_{NH_4} = \frac{NO_3 e^{-\psi NH_4}}{K_{NO} + NO_3} + \frac{NH_4}{K_{NH} + NH_4}\end{aligned}$$

Descriptions of the state variables and parameters used in the equations are provided in Table 4.1.

Phytoplankton concentration increases via joint light- and nutrient-limited growth and decreases via grazing by zooplankton and natural mortality. The formulation for the light-limited growth factor, J , is the modified Monod relationship proposed by Smith (1936). Attenuation of light with depth follows the standard Beer's Law decaying exponential relationship, with separate attenuation coefficients corresponding to absorption by seawater and by phytoplankton biomass. The nutrient-limited growth factor, Q , is the sum of two saturating Monod functions, one each for nitrate and ammonium. Inhibition of nitrate uptake in the presence of ammonium is included in the nitrate term in the exponential formulation proposed by Wroblewski (1977). The multiplication of J and Q in the phytoplankton growth term follows Fasham et al. (1990).

Table 4.1 Symbols used in the ecosystem model. Parameter values are given for this study and three other similar studies.

Symbol	Description	Units	Values			
			This study	Fasham et al. (1990)	Lima et al. (2002)	Newberger et al. (2003)
e_z	zooplankton excretion rate	d^{-1}	0.1	0.1	-	0.145 ^b
g	zooplankton maximum grazing rate	d^{-1}	0.75	1.0	1.0	0.52, 1.5
I	PAR irradiance	W m^{-2}	-	-	-	-
I_o	mean surface PAR irradiance	W m^{-2}	200	-	104 ^a	158
K_{NH}	NH_4 half-saturation constant	$\mu\text{M-N}$	0.5	0.5	-	1.0
K_{NO}	NO_3 half-saturation constant	$\mu\text{M-N}$	1.0	0.5	0.6	1.0
K_p	P half-saturation constant	$\mu\text{M-N}$	1.0	1.0	1.0	-
K_z	Vertical mixing coefficient	$\text{m}^2 \text{d}^{-1}$	1	-	0.1	-
k_ϕ	light attenuation by P	$\mu\text{M-N}^{-1} \text{m}^{-1}$	0.01	0.03	-	0.0095
k_w	light attenuation by seawater	m^{-1}	0.04	0.04	0.035	0.067
m_p	phytoplankton mortality rate	d^{-1}	0.1	0.045, 0.09	0.01	0.1
m_z	zooplankton mortality rate	d^{-1}	0.05	0.05	0.1	b
NH_4	ammonium concentration	$\mu\text{M-N}$	-	-	-	-
NO_3	nitrate concentration	$\mu\text{M-N}$	-	-	-	-
P	phytoplankton concentration	$\mu\text{M-N}$	-	-	-	-
t	time	d	-	-	-	-
Z	zooplankton concentration	$\mu\text{M-N}$	-	-	-	-
z	depth	m	-	-	-	-
α	initial slope of P_B vs. I curve	$(\text{W m}^{-2})^{-1} \text{d}^{-1}$	0.025	0.025	0.025	0.025
γ	zooplankton assimilation efficiency	-	0.7	0.75	0.8	0.7
μ_m	P maximum growth rate	d^{-1}	2.0	2.9	2.0	1.5
ψ	NH_4 inhibition parameter	$\mu\text{M-N}^{-1}$	1.5	1.5	-	1.46

^a Lima et al. used an annual average for latitude 30°. I doubled this to get a value more representative of summer conditions.

^b Newberger et al. combined zooplankton excretion and mortality into a single linear loss term with the rate constant given here.

Fasham et al. (1990) described grazing on phytoplankton by zooplankton using a Monod relationship, while mortality of phytoplankton and zooplankton were taken as simple linear functions, as was zooplankton excretion. I do the same in my model.

Nitrate concentration decreases as a result of phytoplankton uptake; ammonium levels increase via zooplankton excretion and decrease via phytoplankton uptake. The second-derivative terms in the equations represent vertical mixing and are used only in the one-dimensional model solution.

I obtained quasi-steady-state solutions to the equations above using a simple forward-differencing scheme in Matlab. No-flux boundary conditions were imposed at the surface and bottom for all variables. Although total nitrogen is not conserved in the model, concentration changes after 300 days of model simulation time are small. Computing the change in total nitrogen integrated over the water column at 300 days results in a net loss rate of $-3.52 \text{ mmol m}^{-2} \text{ d}^{-1}$, or about $-0.08\% \text{ d}^{-1}$. This net loss is dominated by loss of NO_3 deep in the water column ($-3.50 \text{ mmol m}^{-2} \text{ d}^{-1}/-0.08\% \text{ d}^{-1}$). Losses also occur in the phytoplankton and zooplankton compartments ($-0.013 \text{ mmol m}^{-2} \text{ d}^{-1}/-0.06\% \text{ d}^{-1}$ and $-0.019 \text{ mmol m}^{-2} \text{ d}^{-1}/-0.08\% \text{ d}^{-1}$, respectively), while total ammonium increases ($0.014 \text{ mmol m}^{-2} \text{ d}^{-1}/0.21\% \text{ d}^{-1}$). At 50-m depth, nitrogen is lost from each of the four compartments at rates ranging from -0.07 to $-0.2\% \text{ d}^{-1}$.

One-dimensional profiles, generated over a 300-m water column after 300 days of model simulation, were compared to nutrient and phytoplankton biomass data that were collected near the Flower Garden Banks during the LATEX program (Jochens et al., 1998). Parameters were chosen to be in the range of those used for three similar ecosystem models (Fasham et al., 1990; Lima et al., 2002; Newberger et al., 2003); minor tuning of the parameters within these ranges optimized the model-data fit. The vertical mixing coefficient was chosen to be consistent with the background value used in the three-dimensional model.

The solutions for nitrate concentration and phytoplankton concentration represent the data well (Fig. 4.5). The model produces a nutricline that is less sharp than the data indicate, but it occurs at about the right depth. The subsurface maximum in

phytoplankton biomass is captured in the model profile. The scatter in the ammonium data makes it difficult to judge the quality of the model solution, although it appears to underestimate ammonium concentration. The model predicts a subsurface maximum in zooplankton biomass that is less pronounced than for phytoplankton; no zooplankton data were available for comparison.

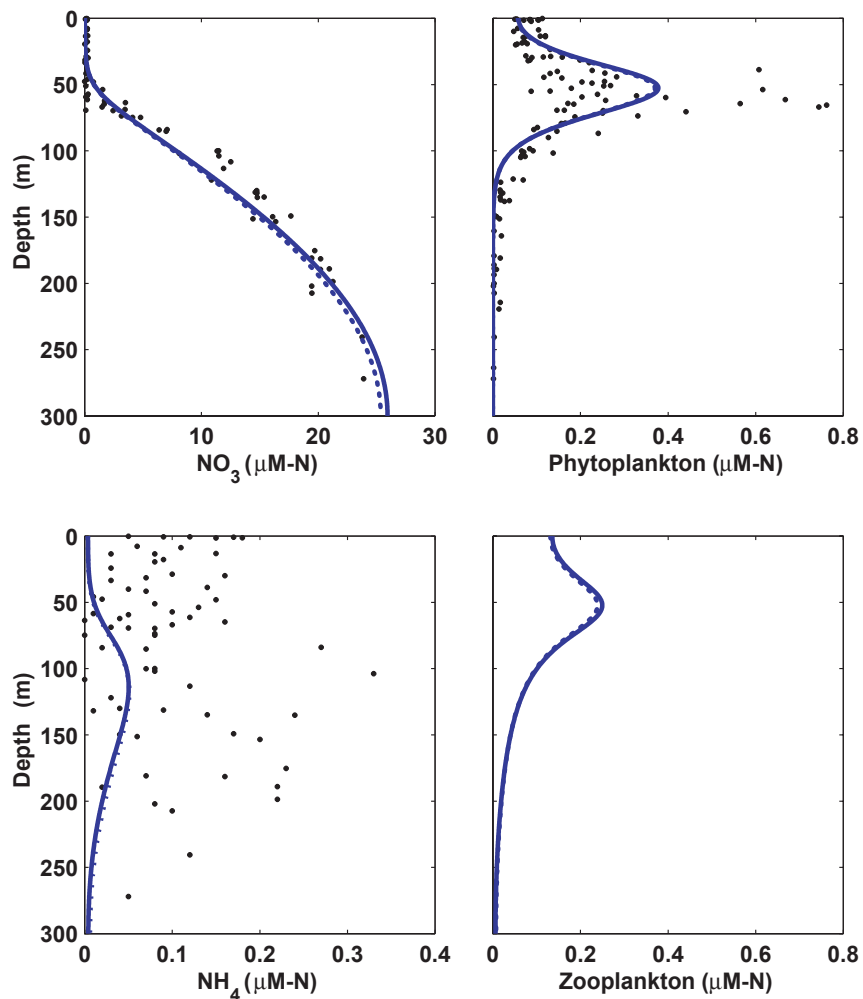


Fig. 4.5 Results of the one-dimensional model. Black dots are data from several stations near the Flower Garden Banks visited during cruise H09 of the LATEX program. Solid blue lines are model solutions after 300 days. Dotted blue lines are model solutions after 330 days and show the quasi-steady nature of the model solution.

4.6.2 *Coupled hydrodynamic-ecosystem model*

I used the results of the 1-D model to initialize the biological variables in the 3-D hydrodynamic-ecosystem model. The physical and biological components of the model are fully coupled in that advection and diffusion of the biological tracers are dictated by the solution of the physical flow field at each grid point and at each time step.

Upwelling of nitrate occurs in the wake of each of the modeled banks, as it did for the passive tracer simulation. This upwelling is accompanied, in the full ecosystem

simulation, by increases in phytoplankton and zooplankton biomass (Fig. 4.6).

Phytoplankton concentration near the banks reaches $1.2 \mu\text{M-N}$, a three-fold increase over the background $0.4 \mu\text{M-N}$; maximum zooplankton concentration is about double the background value (0.5 vs. $0.25 \mu\text{M-N}$). Changes in the ammonium concentration are negligible over the course of the simulation and are not shown. The nitrate plumes dissipate more rapidly with distance from the banks than do the plankton plumes, which extend to more than 100 km downstream of the banks after 21 days.

4.7 Discussion

My model results support the hypothesis that flow disruption at the Flower Garden Banks leads to upwelled nutrients in the bank wakes. The increased nutrient concentration is sufficient to induce a response in the planktonic food web. Hence, the Banks may promote the formation of hotspots of elevated primary and secondary production in an otherwise oligotrophic environment. Such increased production can contribute to overall shelf productivity and may serve as a food source to the higher trophic level organisms that live on and around the Flower Garden Banks.

The rate constants and parameter values used in the ecosystem model are “typical” values compiled from various literature sources. Although they are consistent with what is known about nutrient-plankton dynamics in oligotrophic systems, the quantitative details of the biological response produced in the model are unlikely to be representative of any particular ecosystem. Still, the potential for topographically generated flows to impact biological processes is clear in the model results. Incorporation of ecosystem-specific experimentally determined model parameters would greatly improve the

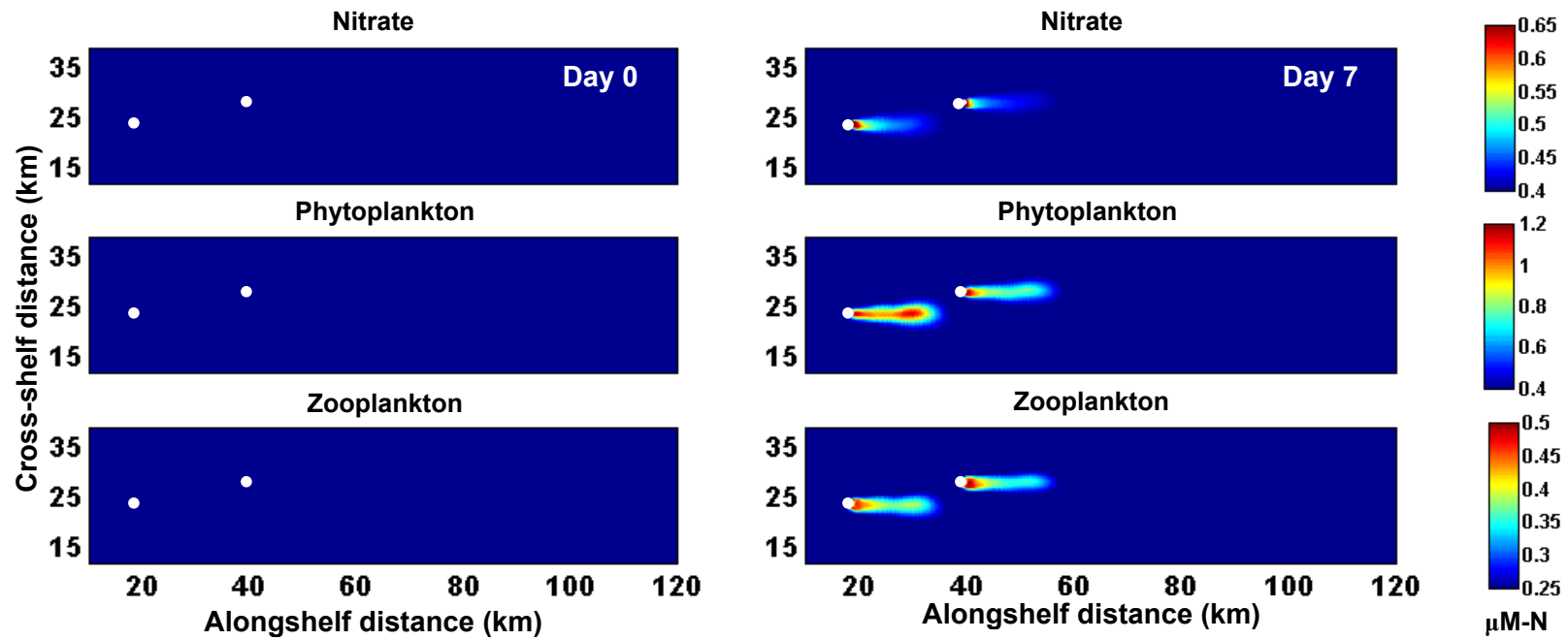


Fig. 4.6. Results of the three-dimensional coupled model. Sections at 50 m.

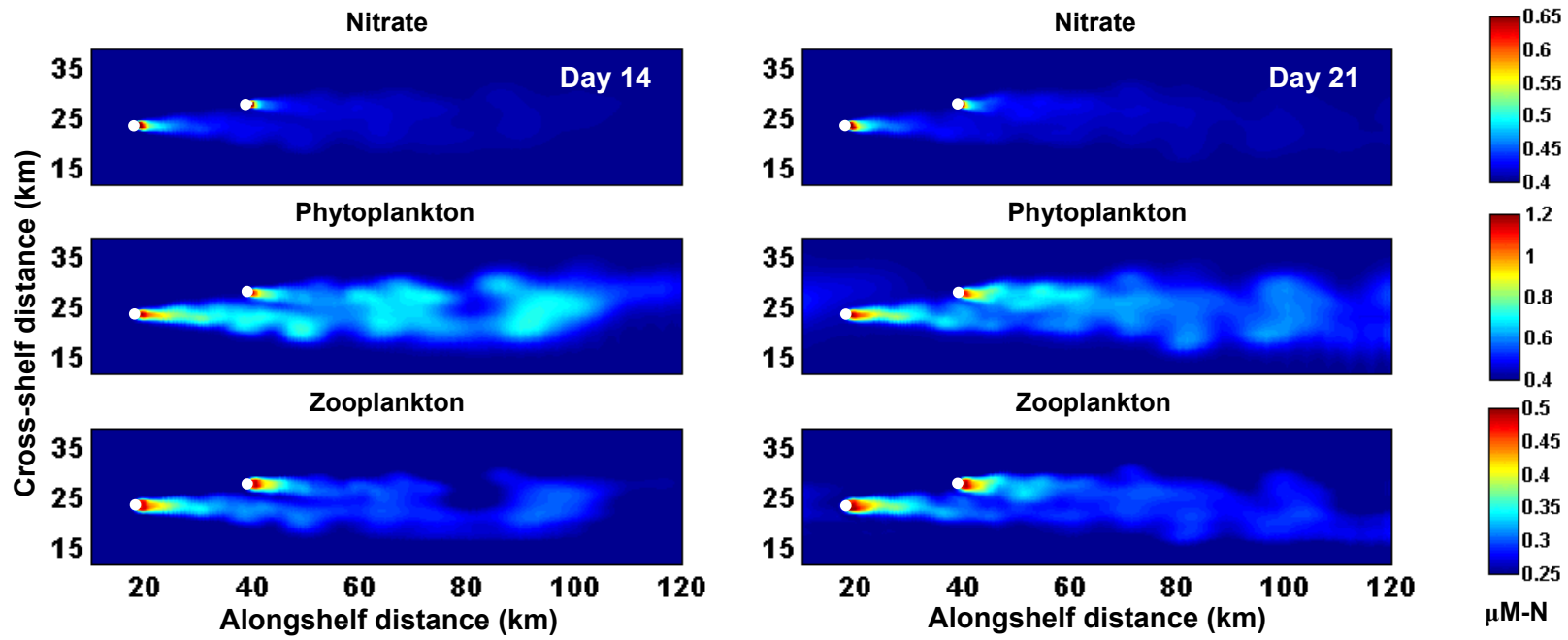


Fig. 4.6. Continued.

realism of the model, as would the inclusion of additional biological compartments such as bacteria and detritus.

The plankton plumes generated in my model are consistent with the field observations of Coutis & Middleton (1999), who found enhanced planktonic biomass in the lee of an isolated island subjected to a weak, essentially unidirectional inflow. Use of a more sophisticated forcing scheme in the model (oscillating inflow, for instance) might lead not to a plume but to a “cloud” of high planktonic biomass surrounding the banks. This would be more in line with the broader patterns of increased plankton abundance observed by Dower et al. (1992) and Mullineaux & Mills (1997), where the measured flow fields were not unidirectional in nature.

It is important to note that the enhanced nutrient and plankton concentrations produced in the model are subsurface effects (as are the flow disturbances). This makes it difficult to test the results of the model using satellite data like ocean color, since satellite sensors can only penetrate to one optical depth—about 25 m at the Flower Garden Banks. A careful field study may be the only way to adequately test the model predictions.

The Flower Garden Banks are just two of dozens of similar shallow topographic banks on the Louisiana-Texas shelf (Rezak et al., 1985). If the phenomena of upwelled nutrients and increased planktonic biomass produced in my model function similarly at these other shelf banks, then hotspots of biological activity may be a relatively common occurrence on the continental shelf of the northern Gulf of Mexico, as well as on other shelves where shallow banks are found.

4.8 Conclusions

Although the coupled hydrodynamic-ecosystem model I used in this study is based on greatly simplified geometry, physical forcing and biological interactions, it is a useful first step in exploring how topographically influenced flows can affect biological processes in the ocean. It demonstrates that turbulent wakes behind submerged shallow banks act to bring nutrients into the euphotic zone from deeper water and that the increased nutrient concentration can trigger increases in phytoplankton and zooplankton

biomass in distinct wake regions downstream of the banks. Such locally enhanced primary and secondary production may play an important role in the overall ecosystem dynamics of shallow oceanic peaks in general and the Flower Garden Banks in particular.

CHAPTER V

CONCLUSIONS

My model results suggest that interactions between ocean currents and the topography of the Flower Garden Banks result in complex flow patterns that strongly affect local larval transport and plankton dynamics. For resident reef-building corals, whose life cycles include a planktonic larval phase, maintenance and growth of populations through the establishment of new colonies depends on, among many other factors, the supply of settlement-ready larvae to suitable benthic habitats. The physical mechanisms that determine whether a larva is retained near its natal habitat, transported to another suitable natural or man-made habitat, or swept away to an unsuitable habitat can thus play crucial roles in population dynamics and ecosystem structure.

The topographically induced flow disturbances in my model can work to temporarily trap passive particles in the bank wakes, but most particles are swept downstream quickly under the influence of unidirectional alongshelf flow. Under these conditions, dispersal of larvae away from their natal habitats seems much more likely than retention and self-seeding. Larvae that are positively buoyant upon release are even less likely to remain near their bank of origin, since the recirculation that causes trapping in the wakes is a subsurface effect, and will not retain particles at the sea surface.

The relatively short distance between the East and West Flower Garden Banks, and their alignment with respect to the alongshelf direction of the mean flow, creates conditions conducive to interbank exchange of larvae. The prevalent eastward flow favors larval transport from the West Bank to the East Bank. Both banks are probable sources of coral larvae to offshore oil and gas platforms.

The upwelling of nutrients in the lee of the banks and resultant increases in plankton biomass evident in my coupled hydrodynamic-ecosystem model may provide a localized supplemental food source to higher trophic level organisms living on and around the Flower Garden Banks. Hotspots of plankton productivity associated with abrupt

topography may be common on the continental shelf of the northern Gulf of Mexico and in other shelf regions where shallow topographic banks are found.

Although the models I've implemented here are designed to study one particular ecosystem, the fundamental approach taken—of coupling a three-dimensional hydrodynamic model to a particle-tracking algorithm and to a simple plankton model—is broadly applicable. This study is merely representative of the general usefulness and feasibility of taking this type of modeling approach to study the mechanisms of flow-topography interactions and their influences on biological processes in the ocean.

REFERENCES

- Babcock, R.C., Heyward, A.J., 1986. Larval development of certain gamete-spawning scleractinian corals. *Coral Reefs* 5, 111–116.
- Baggett, L.S., 1985. Patterns of coral recruitment at the East Flower Garden Bank. M.S. Thesis, Department of Oceanography, Texas A&M University, College Station, TX, 55 pp.
- Beckman, A., Haidvogel, D.B., 1993. Numerical simulation of flow around a tall isolated seamount, Part I: problem formulation and model accuracy. *J. Phys. Oceanogr.* 23, 1736–1753.
- Beckman, A., Haidvogel, D.B., 1997. A numerical simulation of flow at Fieberling Guyot. *J. Geophys. Res.* 102 (C3), 5595–5613.
- Black, K.P., 1993. The relative importance of local retention and inter-reef dispersal of neutrally buoyant material on coral reefs. *Coral Reefs* 12, 43–53.
- Black, K.P., Moran, P.J., Hammond, L.S., 1991. Numerical models show coral reefs can be self-seeding. *Mar. Ecol. Prog. Ser.* 74, 1–11.
- Bograd, S.J., Rabinovich, A.B., LeBlond, P.H., Shore, J.A., 1997. Observations of seamount-attached eddies in the North Pacific. *J. Geophys. Res.* 102 (C6), 12,441–12,456.
- Bokaian, A., Geoola, F., 1984. Vortex shedding from two interfering circular cylinders. *J. Eng. Mech., ASCE* 110 (4), 623–628.
- Boyer, D.L., Davies, P.A., 1982. Flow past a circular cylinder on a β -plane. *Phil. Trans. R. Soc. Lond., Ser. A* 306, 533–556.
- Boyer, D.L., Davies, P.A., Holland, W.R., Biolley, F., Honji, H., 1987. Stratified rotating flow over and around isolated three-dimensional topography. *Phil. Trans. R. Soc. Lond., Ser. A* 322, 213–241.
- Boyer, D.L., Kmetz, M.L., 1983. Vortex shedding in rotating flows. *Geophys. Astrophys. Fluid Dyn.* 26, 51–83.

- Boyer, D.L., Zhang, X., 1990. Motion of oscillatory currents past isolated topography. *J. Phys. Oceanogr.* 20, 1425–1448.
- Bright, T.J., Gittings, S.R., Zingula, R., 1991. Occurrence of Atlantic reef corals on offshore platforms in the northwestern Gulf of Mexico. *Northeast Gulf Sci.* 12 (1), 55–60.
- Brooks, D.A., 1984. Current and hydrographic variability in the northwestern Gulf of Mexico. *J. Geophys. Res.* 89 (C5), 8022–8031.
- Browne, K.A., Zimmer, R.K., 2001. Controlled field release of a waterborne chemical signal stimulates planktonic larvae to settle. *Biol. Bull.* 200 (1), 87–91.
- Bull, G. 1986. Distribution and abundance of coral plankton. *Coral Reefs* 4, 197–200.
- Butman, C.A., Grassle, J.P., Webb, C.M., 1988. Substrate choices made by marine larvae settling in still water and in a flume flow. *Nature* 333 (6175), 771–773.
- Castro, I., Vosper, S., Paisley, M., Hayden, P., 2001. Vortex shedding behind tapered obstacles in neutral and stratified flow. *Dyn. Atmos. Oceans* 34, 145–163.
- Chapman, D.C., Haidvogel, D.B., 1992. Formation of Taylor caps over a tall isolated seamount in a stratified ocean. *Geophys. Astrophys. Fluid Dyn.* 64, 31–65.
- Chapman, D.C., Haidvogel, D.B., 1993. Generation of internal lee waves trapped over a tall isolated seamount. *Geophys. Astrophys. Fluid Dyn.* 69, 33–54.
- Chen, X., Lohrenz, S.E., Wiesenburg, D.A., 2000. Distribution and controlling mechanisms of primary production on the Louisiana-Texas continental shelf. *J. Mar. Systems* 25, 179–207.
- Chia, F.-S., Buckland-Nicks, J., Young, C.M., 1984. Locomotion of marine invertebrate larvae: a review. *Can. J. Zool.* 62, 1205–1222.
- Cho, K., Reid, R.O., Nowlin Jr., W.D., 1998. Objectively mapped stream function fields on the Texas-Louisiana shelf based on 32 months of moored current meter data. *J. Geophys. Res.* 103 (C5), 10377–10390.
- Cochrane, J.D., Kelly, F.J., 1986. Low-frequency circulation on the Texas-Louisiana continental shelf. *J. Geophys. Res.* 91 (C9), 10645–10659.

- Comeau, L.A., Vézina, A.F., Bourgeois, M., Juniper, S.K., 1995. Relationship between phytoplankton production and the physical structure of the water column near Cobb Seamount, northeast Pacific. *Deep-Sea Res.* 42 (6), 993–1005.
- Coutis, P.F., Middleton, J.H., 1999. Flow-topography interaction in the vicinity of an isolated, deep ocean island. *Deep-Sea Res.* 46, 1633–1652.
- Coutis, P.F., Middleton, J.H., 2002. The physical and biological impact of a small island wake in the deep ocean. *Deep-Sea Res.* 49, 1341–1361.
- Cowen, R.K., Lwisa, K.M.M., Sponaugle, S., Paris, C.B., Olson, D.B., 2000. Connectivity of marine populations: open or closed? *Science* 287, 857–859.
- Crawford, W.R., Dewey, R.K., 1989. Turbulence and mixing: sources of nutrients on the Vancouver Island continental shelf. *Atmosphere-Ocean* 27 (2), 428–442.
- Crimaldi, J.P., Thompson, J.K., Rosman, J.H., Lowe, R.J., Koseff, J.R., 2002. Hydrodynamics of larval settlement: the influence of turbulent stress events at potential recruitment sites. *Limnol. Oceanogr.* 47 (4), 1137–1151.
- Dight, I.J., James, M.K., Bode, L., 1990. Modelling the larval dispersal of *Acanthaster planci*—II. Patterns of reef connectivity. *Coral Reefs* 9, 125–134.
- DiMarco, S.F., Jochens, A.E., Howard, M.K., 1997. LATEX shelf data report: current meter moorings, April 1992 to December 1994. Tech. Rep. 97-01-T, Oceanography Department, Texas A&M University, College Station, TX, 3701pp.
- DiMarco, S.F., Reid, R.O., 1998. Characterization of the principal tidal current constituents on the Texas-Louisiana shelf. *J. Geophys. Res.* 103 (C2), 3093–3109.
- Dower, J., Freeland, H., Juniper, K., 1992. A strong biological response to oceanic flow past Cobb Seamount. *Deep-Sea Res.* 39 (7/8), 1139–1145.
- Fadlallah, Y.H., 1983. Sexual reproduction, development and larval biology in scleractinian corals: a review. *Coral Reefs* 2, 129–150.
- Fasham, M.J.R., Ducklow, H.W., McKelvie, S.M., 1990. A nitrogen-based model of plankton dynamics in the oceanic mixed layer. *J. Mar. Res.* 48, 591–639.
- Forristall, G.Z., 1996. Measurements of current blockage by the Bullwinkle platform. *J. Atmos. Ocean. Tech.* 13, 1247–1266.

- Gardner, J.V., Mayer, L.A., Hughes Clarke, J.E., Kleiner, A., 1998. High-resolution multibeam bathymetry of East and West Flower Gardens and Stetson Banks, Gulf of Mexico. *Gulf of Mexico Sci.* 16 (2), 131–143.
- Gittings, S.R., Boland, G.S., Deslarzes, K.J.P., Combs, C.L., Holland, B.S., Bright, T.J., 1992. Mass spawning and reproductive viability of reef corals at the East Flower Garden Bank, northwest Gulf of Mexico. *Bull. Mar. Sci.* 51 (3), 420–428.
- Goldner, D.R., Chapman, D.C., 1997. Flow and particle motion induced above a tall seamount by steady and tidal background currents. *Deep-Sea Res.* 44 (5), 719–744.
- Goreau, N.I., Goreau, T.J., Hayes, R., 1981. Settling, survivorship and spatial aggregation in planulae and juveniles of the coral *Porites porites* (Pallas). *Bull. Mar. Sci.* 31, 424–435.
- Hagman, D.K., Gittings, S.R., Deslarzes, K.J.P., 1998. Timing, species participation and environmental factors influencing annual mass spawning at the Flower Garden Banks (northwest Gulf of Mexico). *Gulf of Mexico Sci.* 16 (2), 170–179.
- Haidvogel, D.B., Arango, H.G., Hedstrom, K., Beckman, A., Malanotte-Rizzoli, P., Shchepetkin, A.F., 2000. Model evaluation experiments in the North Atlantic Basin: simulations in nonlinear terrain-following coordinates. *Dyn. Atmos. Oceans* 32, 239–281.
- Harrison, P.L., Babcock, R.C., Bull, G.D., Oliver, J.K., Wallace, C.C., Willis, B.L., 1984. Mass spawning in tropical reef corals. *Science* 223, 1186–1189.
- Hasegawa, D., Yamazake, H., Lueck, R.G., Seuront, L., 2004. How islands stir and fertilize the upper ocean. *Geophys. Res. Lett.* 31, L16303, doi: 10.1029/2004GL020143.
- Hogg, N.G., 1973. On the stratified Taylor column. *J. Fluid Mech.* 58 (3), 517–537.
- Huppert, H.E., Bryan, K., 1976. Topographically generated eddies. *Deep-Sea Res.* 23, 655–679.
- Jochens, A., Wiesenberg, D.A., Sahl, L.E., Lyons, C.N., DeFreitas, D.A., 1998. LATEX shelf data report: hydrography, April 1992 through December 1994. Tech. Rep. 96-

- 6-T, Oceanography Department, Texas A&M University, College Station, TX, 1902 pp.
- Jones, G.P., Millicich, M.J., Emslie, M.J., Lunow, C., 1999. Self-recruitment in a coral reef fish population. *Nature* 402, 802–804.
- Kjørboe, T., 1993. Turbulence, phytoplankton cell size and the structure of pelagic food webs. *Adv. Mar. Biol.* 29, 1–72.
- Kloppmann, M., Mohn, C., Bartsch, J., 2001. The distribution of blue whiting eggs and larvae on Porcupine Bank in relation to hydrography and currents. *Fish. Res.* 50, 89–109.
- Kojis, B.L., Quinn, N.J., 1982. Reproductive ecology of two Faviid corals (Coelenterata: Scleractinia). *Mar. Ecol. Prog. Ser.* 8, 251–255.
- Lavelle, J.W., Lozovatsky, I.D., Smith IV, D.C., 2004. Tidally induced turbulent mixing at Irving Seamount—modeling and measurements. *Geophys. Res. Lett.* 31, L10308, doi: 10.1029/2004GL019706.
- Levin, L.A., 1990. A review of methods for labeling and tracking marine invertebrate larvae. *Ophelia* 32 (1-2), 115–144.
- Lewis, J.B., 1974. The settlement behavior of the planulae larvae of the hermatypic coral *Favia fragum* (Esper). *J. Exp. Mar. Biol. Ecol.* 15, 165–172.
- Lima, I.D., Olson, D.B., Doney, S.C., 2002. Biological response to frontal dynamics and mesoscale variability in oligotrophic environments: biological production and community structure. *J. Geophys. Res.* 107 (C8), doi: 10.1029/2000JC000393.
- Lueck, R.G., Mudge, T.D., 1997. Topographically induced mixing around a shallow seamount. *Science* 276, 1831–1833.
- Lugo-Fernández, A., Deslarzes, K.J.P., Price, J.M., Boland, G.S., Morin, M.V., 2001. Inferring probable dispersal of Flower Garden Banks Coral Larvae (Gulf of Mexico) using observed and simulated drifter trajectories. *Cont. Shelf Res.* 21, 47–67.
- Marchesiello, P., McWilliams, J.C., Shchepetkin, A., 2001. Open boundary conditions for long-term integrations of regional oceanic models. *Ocean Modelling* 3, 1–20.

- Marchesiello, P., McWilliams, J.C., Shchepetkin, A., 2003. Equilibrium structure and dynamics of the California current system. *J. Phys. Oceanogr.* 33, 753–783.
- Mellor, G.L., Yamada, T., 1982. Development of a turbulence closure model for geophysical fluid problems. *Rev. Geophys. Space Phys.* 20 (4), 851–875.
- Miller, K., Mundy, C., 2003. Rapid settlement in broadcast spawning corals: implications for larval dispersal. *Coral Reefs* 22, 99–106.
- Mohn, C., Beckmann, A., 2002. Numerical studies on flow amplification at an isolated shelfbreak bank, with application to Porcupine Bank. *Cont. Shelf Res.* 22, 1325–1338.
- Moum, J.N., Nash, J.D., 2000. Topographically induced drag and mixing at a small bank on the continental shelf. *J. Phys. Oceanogr.* 30, 2049–2054.
- Mullineaux, L.S., Mills, S.W., 1997. A test of the larval retention hypothesis in seamount-generated flows. *Deep-Sea Res.* 44 (5), 745–770.
- Nash, J.D., Moum, J.N., 2001. Internal hydraulic flows on the continental shelf: high drag states over a small bank. *J. Geophys. Res.* 106 (C3), 4593–4611.
- Newberger, P.A., Allen, J.S., Spitz, Y.H., 2003. Analysis and comparison of three ecosystem models. *J. Geophys. Res.* 108 (C3), 3061, doi: 10.1029/2001JC001182.
- Oey, L.-Y., 1995. Eddy- and wind-forced shelf circulation. *J. Geophys. Res.* 100 (C5), 8621–8637.
- Oliver, J.K., King, B.A., Willis, B.L., Babcock, R.C., Wolanski, E., 1992. Dispersal of coral larvae from a lagoonal reef—II. Comparisons between model predictions and observed concentrations. *Cont. Shelf Res.* 12 (7-8), 873–889.
- Owens, W.B., Hogg, N.G., 1980. Oceanic observations of stratified Taylor columns near a bump. *Deep-Sea Res.* 27A, 1029–1045.
- Polovina, J.J., Kleiber, P., Kobayashi, D.R., 1999. Application of TOPEX-POSEIDON satellite altimetry to simulate transport dynamics of larvae of spiny lobster, *Panulirus marginatus*, in the Northwestern Hawaiian Islands, 1993–1996. *Fish. Bull.* 97, 132–143.

- Rezak, R., Bright, T.J., McGrail, D.W., 1985. Reefs and Banks of the northwestern Gulf of Mexico. Wiley-Interscience., New York, 259 pp.
- Rissik, D., Suthers, I.M., Taggart, C.T., 1997. Enhanced zooplankton abundance in the lee of an isolated reef in the south Coral Sea: the role of flow disturbance. *J. Plankton Res.* 19 (9), 1347–1368.
- Royer, T.C., 1978. Ocean eddies generated by seamounts in the North Pacific. *Science* 199, 1063–1064.
- Sahl, L.E., Wiesenburg, D.A., Merrell, W.J., 1997. Interactions of mesoscale features with Texas shelf and slope waters. *Cont. Shelf Res.* 17 (2), 117–136.
- Sammarco, P.W., Andrews, J.C., 1988. Localized dispersal and recruitment in Great Barrier Reef corals: the Helix experiment. *Science* 239, 1422–1424.
- Sammarco, P.W., Atchison, A.D., Boland, G.S., 2004. Expansion of coral communities within the Northern Gulf of Mexico via offshore oil and gas platforms. *Mar. Ecol. Prog. Ser.* 280, 129–143.
- Schär, C., Durran, D.R., 1997. Vortex formation and vortex shedding in continuously stratified flows past isolated topography. *J. Atmos. Sci.* 54, 534–554.
- Scheltema, R.S., 1986. On dispersal and planktonic larvae of benthic invertebrates: an eclectic overview and summary of problems. *Bull. Mar. Sci.* 39 (2), 290–322.
- Shchepetkin, A.F., McWilliams, J.C., 2003. A method for computing horizontal pressure-gradient force in an oceanic model with a nonaligned vertical coordinate. *J. Geophys. Res.* 108 (C3), 3090, doi: 10.1029/2001JC001047.
- Shchepetkin, A.F., McWilliams, J.C., 2005. The regional oceanic modeling system (ROMS): a split-explicit, free-surface, topography-following-coordinate oceanic model. *Ocean Modelling* 9, 347–404.
- Smith, E.L., 1936. Photosynthesis in relation to light and carbon dioxide. *Proc. Nat. Acad. Sci. U.S.A.* 22, 504–511.
- Smith, L.T., 1992. Numerical simulations of stratified rotating flow over finite amplitude topography. *J. Phys. Oceanogr.* 22, 686–696.

- Swearer, S.E., Caselle, J.E., Lea, D.W., Warner, R.R., 1999. Larval retention and recruitment in an island population of a coral-reef fish. *Nature* 402, 799–802.
- Szmant, A.M., 1986. Reproductive ecology of Caribbean reef corals. *Coral Reefs* 5, 43–54.
- Todd, C.D., 1998. Larval supply and recruitment of benthic invertebrates: do larvae always disperse as much as we believe? *Hydrobiologia* 375/376, 1–21.
- Toole, J.M., Schmitt, R.W., Polzin, K.L., Kunze, E., 1997. Near-boundary mixing above the flanks of a midlatitude seamount. *J. Geophys. Res.* 102 (C1), 947–959.
- Visser, A.W., Stips, A., 2002. Turbulence and zooplankton production: insights from PROVESS. *J. Sea Res.* 47, 317–329.
- Warner, R.R., Swearer, S.E., Caselle, J.E., 2000. Larval accumulation and retention: implications for the design of marine reserves and essential fish habitat. *Bull. Mar. Sci.* 66 (3), 821–830.
- Williams, D.McB., Wolanski, E., Andrews, J.C., 1984. Transport mechanisms and the potential movement of planktonic larvae in the central region of the Great Barrier Reef. *Coral Reefs* 3, 229–236.
- Wilson, J.R., Harrison, P.L., 1988. Settlement-competency periods of larvae of three species of scleractinian corals. *Mar. Biol.* 131, 339–345.
- Wolanski, E., Burrage, D., King, B., 1989. Trapping and dispersion of coral eggs around Bowden Reef, Great Barrier Reef, following mass coral spawning. *Cont. Shelf Res.* 9 (5), 479–496.
- Wroblewski, J.S., 1977. A model of phytoplankton plume formation during variable Oregon upwelling. *J. Mar. Res.* 35, 357–394.
- Wyers, S.C., Barnes, H.S., Smith, S.R., 1991. Spawning of hermatypic corals in Bermuda: a pilot study. *Hydrobiologia* 216/217, 109–116.
- Zhang, X., Boyer, D.L., 1991. Current deflections in the vicinity of multiple seamounts. *J. Phys. Oceanogr.* 21, 1122–1138.

VITA

Simone Francis was born in Daly City, California on February 4, 1969, the youngest of three girls. Her parents are David Francis, of Grass Valley, California, and the late Susan Francis. Simone earned a B.E. in mechanical engineering at the City College of New York in 1995, an M.S. in mechanical engineering at the California Institute of Technology in 1996, and a Ph.D. in oceanography at Texas A&M University in 2005. She is a certified scientific diver and holds a private pilot's license.

Permanent address: 257 E. 19th St. Brooklyn, NY 11226